

**X-ray Scattering Studies of Gold Nanoparticle Synthesis at the
Liquid-Liquid Interface**

BY

UMME SHAINAZ URMEE
B.Sc., Bangladesh University of Engineering and Technology, 2008

THESIS

Submitted in partial fulfillment of the requirements
for the degree of Doctor of Philosophy in Chemical Engineering
in the Graduate College of the
University of Illinois at Chicago, 2018

Chicago, Illinois

Defense Committee:

Mark Schlossman, Advisor, Department of Physics
Lewis Wedgewood, Chair
Ying Liu
Vivek Sharma
Ludwig Nitsche

Copyright by

Umme Shainaz Urmee

2017

To my husband, my parents and my sisters.

ACKNOWLEDGMENTS

First, I would like to devote my earnest thanks to my thesis advisor, Professor Mark Schlossman for his constant guidance and support throughout my time as his student. He has introduced me to the highly exciting synchrotron X-ray scattering techniques. He is an excellent scientist and a very good teacher. He has always extracted time from his busy schedules to teach and guide us during the experiments at different synchrotron sources. I consider myself extremely lucky to get an opportunity to work under his supervision. I also want to thank my colleague Dr. Sabina Tatur for her invaluable contribution to my thesis project. I would like to thank Dr. Mrinal Bera for his suggestions on analyzing data.

I acknowledge contributions of Dr. Binhua Lin and Mati Meron at the ChemMatCARS sector of the Advanced Photon Source at Argonne National Laboratory. They were extremely helpful during our X-ray scattering data collection.

Finally, I must thank Dr. Humayun, my husband for his continued support and encouragement. I would also like to thank my parents, my sisters and my friends, without their support this thesis would not be possible.

TABLE OF CONTENTS

<u>CHAPTER</u>		<u>PAGE</u>
1	BACKGROUND	1
1.1	Synthesis of AuNPs	4
1.2	AuNPs formation at L/L interface	6
1.3	Characterization techniques	9
1.3.1	X-ray scattering techniques	11
2	THEORY: X-RAY SCATTERING TECHNIQUES	13
2.1	Introduction	13
2.2	Interaction of X-rays with matter	14
2.2.1	Scattering by an electron	14
2.2.2	Scattering in reciprocal space	16
2.2.3	Scattering by an atom	18
2.3	propagation of X-rays at interfaces	20
2.3.1	The refractive index, n	20
2.3.2	Snell's law, Fresnel coeeficients and penetration depth	20
2.3.3	X-ray penetration depth, Λ	23
2.4	Fresnel reflection and transmission in layered samples	24
2.4.1	Thin film	24
2.4.2	Multilayers	26
2.4.3	Effect of surface roughness on the Fresnel reflectivity	26
2.5	Off-specular scattering	27
2.5.1	Scattering in the kinematical Born approximation	28
2.5.2	Distorted wave Born approximation	33
2.5.3	Form factor of nanoparticle within DWBA	34
2.6	Form factor and Interference function	36
2.7	Effect of Polydispersity	37
2.8	Limiting form of $I(Q)$	37
3	EXPERIMENTS	39
3.1	Gold nanoparticle synthesis	39
3.2	Electrochemical Sample Cell	40
3.3	Sample Preparation	43
3.3.1	LiCl Purification	43
3.4	Preparation of BTPPATPFB	45
3.5	Preparation of TOAAuCl_4 solution in DCE	46
3.6	Distillation of organic solvent	48
3.7	Purification of reducing agent	49

TABLE OF CONTENTS (Continued)

<u>CHAPTER</u>		<u>PAGE</u>
	3.8 Sample cell preparation	49
	3.9 Ag/AgCl electrode preparation	53
	3.10 Electrochemical measurements	54
	3.11 TEM measurements	54
	3.12 X-ray scattering measurements	56
	3.13 Interfacial tension measurement	58
4	GISAXS AT WATER/DCE INTERFACE	60
	4.1 Gold Nanoparticle Synthesis	60
	4.2 Determination of Potential of Zero Charge	63
	4.3 GISAXS Measurement	64
	4.3.1 Two Dimensional GISAXS Patterns	67
	4.3.2 1D Linecuts	68
	4.3.3 Exposure time	70
	4.3.4 Primary Data Processing	70
	4.3.5 Evolution of GISAXS Patterns with Time	72
	4.4 Background Subtraction	74
	4.5 Data Interpretation	78
	4.5.0.1 Shape of the Particle	78
	4.5.1 Data Modeling	82
5	CONCLUSION	106
	APPENDIX	108
	CITED LITERATURE	115

LIST OF TABLES

<u>TABLE</u>		<u>PAGE</u>
I	Electrochemical deposition by changing applied potential and duration time.	63
II	Best fitted parameters of Raleigh form factor fitting with log normal distribution in R.	102

LIST OF FIGURES

FIGURE		PAGE
1	Schematic illustrations of AuNPs formation (a) in homogeneous solution, (b) on solid electrode, (c) at L/L interface	8
2	X-ray scattering geometry	17
3	The incident wave vector \vec{k}_{in} is scattered by an atom in the direction of scattered wave vector \vec{k}_{out} at the origin and at position \vec{r}	19
4	Incident X-rays are reflected and refracted at the interface $z = 0$	21
5	Reflection and transmission in a layer of thickness Δ	24
6	Scattering from a rough surface	28
7	X-ray scattering events within DWBA	35
8	schematic figure of electrochemical sample cell	41
9	3 jaw chuck	42
10	Tilting stage	43
11	Glass tube to purify LiCl	44
12	Recrystallization from acetone	46
13	Setup for preparation of TOAAuCl ₄	47
14	Setup for column chromatography	48
15	Reference electrode preparation	53
16	Parameters for CV measurements	55
17	X-ray scattering measurements	56
18	Schematic figure of liquid-surface spectrometer installed on the Chem-MatCARS at Advanced Photon source, ANL. Copied from Liquid Surfaces and Interfaces: Synchrotron X-ray Methods (p. 31) by P. S. Pershan, M. Schlossman, 2012, Cambridge University Press.	57
19	Interfacial tension measurements	59
20	Voltammograms for the $AuCl_4^-$ ion transfer across the water-DCE interface as a function of scan rate	61
21	Interfacial tension measurements at the interface between 0.1 M LiCl in water and 15 mM BTPPATPFB in DCE.	64
22	Scattering geometry of grazing incidence small angle X-ray scattering.	65
23	Sample Height Scan	67
24	2D GISAXS image	68
25	(a) 2D GISAXS image converted to Q space. (b) I vs Q curve integrated over the narrow white bounded region	69
26	background subtracted GISAXS patterns with time	72
27	I vs Q curves with time	73

LIST OF FIGURES (Continued)

<u>FIGURE</u>		<u>PAGE</u>
28	X-ray transmission through the sample and scattering from bare interface linecuts are compared in both direction. The I vs Q_{xy} curve is integrated over Q_z from 0.016 to 0.018 \AA^{-1} and same Q_{xy} is integrated for I vs Q_z curve.	75
29	background subtracted GISAXS pattern at (a)bare interface (b)at $t = 0$ to 10 minutes	76
30	The constant background at high Q (blue curve) is fitted (red curve) and subtracted (green curve).	77
31	TEM image of gold nanoparticles forming at liquid/liquid interface at 300k magnification. Particles were formed by applying 450 mV at the interface for 1 minute and then collected immediately	79
32	log-log plot of the I vs Q_z with a power law fitting at high Q_{xy} range	80
33	log-log plot of the I vs Q_{xy} with a power law fitting at high Q_{xy} range	81
34	I vs. Q (blue curve) for t=0 to 10 minutes is fitted (red curve). . . .	88
35	Distribution of χ^2 with R.	89
36	I vs. Q (blue curve) for t=11 to 20 minutes is fitted (red curve). Bottom part of the figure shows residuals.	90
37	I vs. Q (blue curve) for t=21 to 30 minutes is fitted (red curve). Bottom part of the figure shows residuals.	91
38	I vs. Q (blue curve) for t=141 to 150 minutes is fitted (red curve). Bottom part of the figure shows residuals.	92
39	I vs. Q (blue curve) for t=151 to 160 minutes is fitted (red curve). Bottom part of the figure shows residuals.	93
40	I vs. Q (blue curve) for t=185 to 194 minutes is fitted (red curve). Bottom part of the figure shows residuals.	94
41	I vs. Q (blue curve) for t=323 to 332 minutes is fitted (red curve). Bottom part of the figure shows residuals.	95
42	I vs. Q (blue curve) for t=337 to 346 minutes is fitted (red curve). Bottom part of the figure shows residuals.	96
43	I vs. Q (blue curve) for t=348 to 357 minutes is fitted (red curve). Bottom part of the figure shows residuals.	97
44	I vs. Q (blue curve) for t=358 to 369 minutes is fitted (red curve). Bottom part of the figure shows residuals.	98
45	I vs. Q (blue curve) for t=423 to 432 minutes is fitted (red curve). Bottom part of the figure shows residuals.	99
46	I vs. Q (blue curve) for t=435 to 444 minutes is fitted (red curve). Bottom part of the figure shows residuals.	100
47	I vs. Q (blue curve) for t=447 to 456 minutes is fitted (red curve). Bottom part of the figure shows residuals.	101
48	Best fitted values of R, σ and $\frac{A}{V^2}$	104

LIST OF ABBREVIATIONS

L/L	Liquid-Liquid
GISAXS	Grazing Incidence Small Angle X-ray scattering
XR	X-ray Reflectivity
TEM	Transmission Electron Microscopy
CV	Cyclic Voltammogram
NPs	Nanoparticles
AuNPs	Gold Nanoparticles
BA	Born Approximation
DWBA	Distorted Wave Born Approximation
TPTA	Tri-(p-tolyl)amine
DCE	1,2-Dichloroethane
<i>TOAAuCl₄</i>	Tetraoctylammoniumtetrachloroaurate
TPTA	Tri-(p-tolyl)amine
BTPPATPFB	Bis(triphenylphosphoranylidene)ammonium tetrakis(pentafluorophenyl)borate tetraoctylammoniumtetrachloroaurate (TOAAuCl(4))

SUMMARY

The electrodeposition of gold at the interface between water and organic solvent 1,2-Dichloroethane has been investigated using reduction of tetrachloroaurate with tri-(p-tolyl)amine as reducing agent. The experiments were carried out in a custom built four-electrode electrochemical cell. The electrochemical cell allowed us to apply a potential across the interface in order to control the transport of reactants across the interface that initiated and sustained the nanoparticle formation. Temporal size/shape evolution of gold nanoparticles was studied with in situ grazing-incidence small angle X-ray scattering (GISAXS). GISAXS provided time-resolved information of the size of the gold nanoparticles at the interface from an average radius of 19 nm to 30 nm. To the extent of our knowledge, this is the first illustration of GISAXS setup for time-resolved studies of nanoparticle formation at the electrified liquid-liquid interfaces.

CHAPTER 1

BACKGROUND

The synthesis and characterization of metal nanoparticles (NPs) is one of the most investigated areas in nanoscience and nanotechnology. In particular, gold nanoparticles (AuNPs), also known as gold colloids, have been studied for their fascinating size related electronic, magnetic and optical properties. Due to quantum size effects AuNPs exhibit properties that are characteristic of neither the bulk metal nor of the molecular compounds. These unique properties have led to the adoption of AuNPs in high technology applications, such as, the use of AuNPs as conductors in printable inks, electronic chips [14]. They are used to connect elements of an electronic chip, like resistors, conductors and thus, are important components in chip design. As another example, AuNPs have applications in photodynamic therapy [29]. When they are excited by light of wavelengths in between 700 to 800 nm, they generate heat. When light is applied to a targeted tumor cell containing AuNPs, the particles quickly heat up and kill the tumor cell. AuNPs are also used in targeted drug delivery [5]. The surface of the particles can be coated with therapeutic agents due to the high ratio of surface area to volume of the AuNPs. AuNPs are used as a substrate in surface enhanced Raman spectroscopy to enable the measurement of vibrational energies of chemical bonds. AuNPs are widely used as catalysts [31]. The surface of the particles can be used for oxidation, in some cases for reduction, as in nitrogen oxide synthesis. In addition to this short list, many other examples of the use of AuNPs could be cited.

AuNPs are generally prepared by solution phase reduction of Au ions. The literature on Au deposition can be traced back to Faraday. Despite this antiquity, interest in solution-based synthesis of AuNPs and their properties have exploded over the past few decades, leading to exponentially increasing number of publications. More recently, synthesis of asymmetric nano-structures, such as nanorods and bi-component core-shell nano-structures have attracted increasing attention because of their unique properties. These complex structures show interesting properties, such as multiple optical absorbance [16], unusual catalytic behavior [35] etc. As mentioned above, the physical and chemical properties of particles are intimately related with the particle size and shapes. Small changes in the preparative conditions often lead to a significant effect on the mean size, size distribution and shapes of the particles. Although reaction conditions can now be tuned to yield NPs of desired size and shape, the understanding of these empirical methods remains incomplete. In order to control the size and shape of the NPs, the detailed understanding of the synthesis process is required. The available quantitative models are not sufficient to tailor physical and chemical properties of NPs by controlling the nucleation and growth steps of the synthesis. Quantitative parameters such as reaction rates and heat and mass transfer coefficients are required for industrial production as the process engineers will require them to scale-up, design and control the process. Therefore, well-designed experiments are necessary to reveal the formation of NPs. The in situ measurements of formation of AuNPs are challenging due to the time and length scales of different steps of growth. Very few reliable measurements of the kinetics of nucleation and growth of NP have been conducted till today. Most of them used ex situ microscopy techniques or in situ optical spectroscopy. While

microscopy techniques can lead to drying artifacts, the indirect spectroscopy measurements are sometime difficult to interpret because of the complexity of a chemical system. Recently, X-ray synchrotron radiation has been found useful to investigate nanomaterials in situ[1, 7].

The interface between two immiscible liquids can be used to investigate atomic and molecular processes of nucleation and growth. A common synthesis route to NPs is based on the spontaneous reaction at the liquid-liquid (L/L) interfaces. NP formation at L/L interfaces can be considered as an intermediate case between purely homogeneous reduction and reduction on a solid electrode.

Nanoparticles are often synthesized at the interface between two immiscible liquids. liquid-liquid (L/L) interface is an ideal system which can be considered as an intermediate between electrodeposition in a homogeneous solution and on a solid electrode. In a homogeneous solution NPs are formed through electron transfer between redox couples which is very difficult in situ. In the case of electrodeposition at a solid electrode-electrolyte interface, any defects on electrode can act as preferential nucleation sites. Moreover, L/L interfaces can be electrochemically polarized which can create a metastable supersaturation at the interface. Thus, the reduction reaction can be confined to a thin layer with a small volume which makes it easier to probe the growth of NPs.

This thesis demonstrates how grazing incidence X-ray scattering (GISAXS) technique can be applied to a liquid-liquid (L/L) electrochemical cell to follow the formation of gold nanoparticles (AuNPs) in-situ. The AuNPs are formed at an electrified interface of two immiscible liquids.

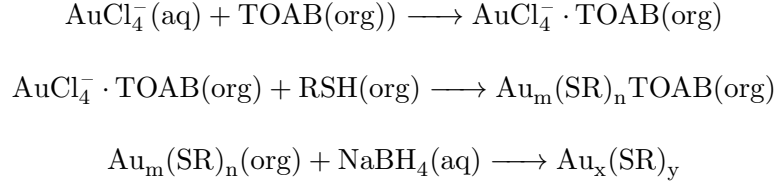
The evolution of the growing AuNPs at the electrified L/L interface with time is probed via in-situ GISAXS using synchrotron radiation.

The remainder of the chapter is arranged as follows: Section 1.1 gives an overview of literature on the study of AuNPs synthesis. Section 1.2 discusses about the advantages of synthesizing AuNPs at a L/L interface for characterizing the growth process and Section 1.3 discusses different techniques to probe synthesis reactions.

1.1 Synthesis of AuNPs

AuNPs are generally obtained by reducing gold(III) derivatives. The reduction reaction has a long pedigree. Two most notable examples are the Turkevitch method and the Brust-Schiffrin Method. The Turkevitch method, introduced in 1951 [32], is one of the simplest and most reliable methods of synthesizing gold nanoparticles. In this method the gold precursor, HAuCl_4 , is reduced by sodium citrate in aqueous solution. The AuNPs (20 nm in diameter) are precipitated from the solution, as the citrate ions act both as the reducing agent and the stabilizing agent.

The BrustSchiffrin Method [6] used L/L systems to synthesize AuNPs, which made a considerable impact in the field of NP synthesis. The biphasic reduction occurs between HAuCl_4 and NaBH_4 in the presence of thiol capping ligands. First, the Au salt is transferred from aqueous to organic phase by the phase-transfer agent tetraoctylammonium bromide (TOAB). In the organic phase Au(III) complex is reduced to Au(I) by alkanethiols (RSH) to form Au(I) thiolate complex. Au(I) is further reduced to Au^0 by the addition of NaBH_4 to the solution. The chemical reactions can be presented as follows:



Although extensive research has been carried out on the growth kinetics of AuNPs synthesis, an unequivocal explanation for the evolution of AuNPs has not been proposed. For example, Kimling et al. [17] proposed a multistep mechanism of AuNPs synthesis by the Turkevitch method. According to their investigation using optical spectroscopy and electron microscopy, the total amount of Au(III) was quickly reduced to Au^0 atoms forming clusters, then the formed clusters assembled into larger polycrystalline particles. The final step was the growth of the clusters by the residual amount of reduced gold in the solution. In contrast to the mechanism proposed by Kimling et al. [17], Pong et al. [24] proposed a new growth kinetics for AuNPs synthesis by the Turkevitch method. Based on TEM and UV-vis-based measurements, the group suggested, an initial fast reduction of $(\text{AuCl}_4)^-$ to form nanoclusters of mean diameter 5 nm. The nanoclusters assembled to form chainlike nanowires, which created a nanowire network. Unstable nanowires increased in diameter and finally collapsed and cleaved into convert into spherical particles. Another report by Ji et al. [15] proposed a mechanism of particle formation by the Turkevitch method which depends on the pH of the solution. According to their findings, the pH of the system has a strong influence on the size/shape distribution and the kinetics of growth to final Au nanocrystals. For the low pH range ($\text{pH} < 6.5$), growth kinetics followed three steps, 1) nucleation, 2) random attachment to polycrystalline nanowires and 3) finally

intraparticle ripening to spherical particles. But for relatively higher pH ($\text{pH} > 6.5$), the study implied two steps: rapid nucleation of atoms and slow diffusion controlled growth.

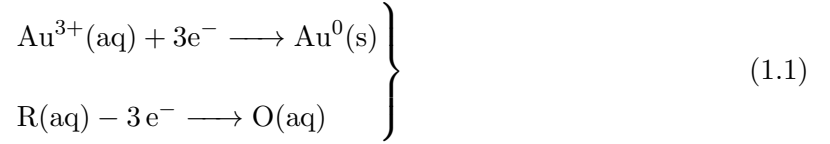
Similarly, a coherent mechanism for the evolution of AuNPs via Brust-Schiffrin method has not found acceptance. Murray et al. [30] analyzed the Brust-Schiffrin method and suggested particles are formed in three steps, 1) nucleation, 2) growth and 3) passivation. The growth of the AuNPs stopped once the surface is completely passivated. Whereas another study of the Brust-Schiffrin method by Peralá et al. [21], predicted nucleation and growth occurred at the same time. Hence, when nucleation, growth and capping of the Au cores reach the final size, new nuclei form in parallel, leading to monodispersed AuNPs.

Hence, present understanding of the AuNPs synthesis does not provide enough molecular level insight into the process and dynamics of particles formation.

1.2 AuNPs formation at L/L interface

The study of the formation of AuNPs formation process becomes much simpler if the reactants are physically separated from each other. This can be achieved by using an immiscible L/L system, where the metal ions and the reducing agents are located in separate phases. The electro-deposition occurs at the L/L interface. The interfacial localization of the particles greatly simplifies the use of several techniques to follow the growth mechanism, such as UV-visible absorption, advanced synchrotron techniques, X-ray absorption etc. A great advantage of the L/L interface is that it can be polarized externally through a potentiostat. The ability to vary the interfacial potential can be used to control the electro-deposition process at the interface.

For example, AuNPs are formed by reducing gold(III) precursor by a reducing agent. The half-reactions can be generalized as:



In the redox reaction in Eq. 1.1, Au^{3+} is reduced to Au^0 by the reducing agent R to form oxidizing product, O. The reaction is assumed to occur in aqueous solution.

The thermodynamics of Eq. 1.1 are given by the Nernst equation. The Nernst equation relates the electrochemical cell potential E at any temperature T with the standard cell potential ΔE^o and activities of the chemical compounds a participating in the redox reaction.

$$E = \Delta E^o + \frac{RT}{3F} \ln \frac{a^{\text{Au}^{3+}} a^{\text{R}}}{a^{\text{Au}^0} a^{\text{O}}} \quad (1.2)$$

In Eq. 1.2, ΔE^o is defined as the difference in reduction potential between the Au^{3+} and R at standard conditions. Solution phase activities, $a_{\text{Au}^{3+}}$, a_{R} , a_{O} can be approximated as concentrations, $[\text{Au}^{3+}]$, $[\text{R}]$, $[\text{O}]$, respectively, and the solid phase activity a_{Au^0} can be taken as unity. Equation 1.2 can be rewritten as,

$$E = \Delta E^o + \frac{RT}{3F} \ln \frac{[\text{Au}^{3+}][\text{R}]}{[\text{O}]} \quad (1.3)$$

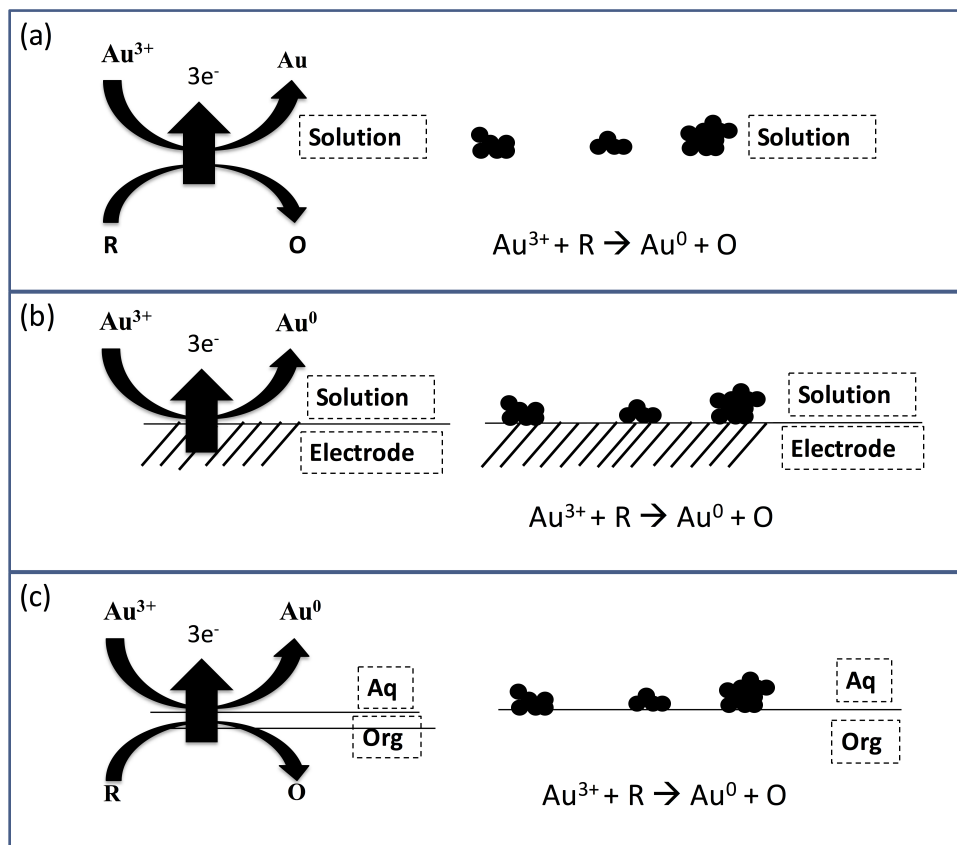
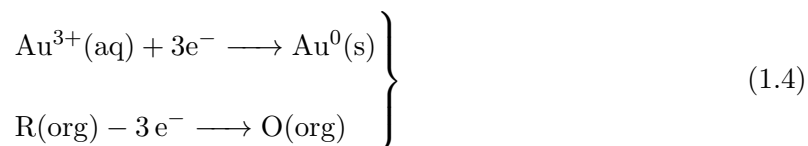


Figure 1: Schematic illustrations of AuNPs formation (a) in homogeneous solution, (b) on solid electrode, (c) at L/L interface .

Hence, according to Eq. 1.3 the driving force for the growth of the AuNPs can be manipulated by varying the concentration of the reactants. It is also well known, that particle size and shape can be tuned by changing concentration of the precursor or the reduction strength of the reducing agent. However, there is no way to manipulate the reaction in situ, if both the

reactants are in the same phase as in Eq. 1.1. The driving force, E also changes with time due to reagent depletion near the electrode, which is regarded as the concentrations of the reactants. This uncontrollable situation changes if the redox reaction occurs at the L/L interface as in Eq. 1.4.



Nernst equation is still valid for Eq. 1.4, but the driving force E , which is the interfacial potential in this case, can be controlled by applying potential across the interface. Figure 1 illustrates the the reduction of Au^{3+} , (a) in a homogeneous solution by a reducing agent, R, b) on a solid electrode, and (c) at the L/L interface where Au^{3+} and R are in separate phases.

The ability to control the potential, hence, the driving force at the L/L interface allows us to tune the particles formation rate. The applied potential can be used to trigger the reduction reaction at the interface at a specific time which is of great advantage to probe the formation process in-situ. L/L interface also has the advantage of localizing the formation reaction at the interface. Therefore, electrodeposition at L/L interfaces is a powerful synthesis route to probe the AuNPs formation reaction.

1.3 Characterization techniques

One of the limitations of the literature on the study of NPs formation is the reliance on ex-situ microscopic methods as characterization tools. Although electron microscopy is often used,

it has very limited relevance to the structure of growing particles in the solution. In general, to perform electron microscopy the particles are removed from the solution and subsequently immobilized on a solid grid, therefore, the technique only probes the final structures of the particles. Also the structures may be subject to drying artifacts. As no information is obtained on the growth of the particles, any apparent relation between the growth conditions and particle structure cannot be established. Recently, a study on the growth of Pt NPs has employed in-situ transmission electron microscopy (TEM) in liquid where the electron beam induced the Pt(II) reactants [19]. Overall, although microscopy techniques provide required structural information, they pose limitations, such as (a) low statistics, (b) convolution with the shape of the tip, (c) difficult to measure on insulated substrate, (d) challenging to use in in-situ growth because of the interruption in the growth process, (e) difficulty to characterize embedded particles, and (f) are often destructive.

Optical absorption spectroscopy is also employed to probe the growth of particles in-situ, but extracting informations from the spectroscopy can be very complex. At any given time there are reactants and particles at different stages of growth present in the chemical system. Complex chemical reactions with overlapping absorption spectra, as well as scattering by the particles when they reaches optical wavelength require spectral deconvolution. Often, even with the deconvolution the interpretation is ambiguous.

Structurally more incisive techniques are required for the characterization of NP growth as a function of particle size, from the very early stages of particle nucleation by the reaction of dissolved molecular species to the growth of the nuclei to the final, ligand-stabilized NPs.

1.3.1 X-ray scattering techniques

X-ray scattering techniques have emerged as a powerful tool in the last two decades. This reciprocal space technique provides information from a large number of NPs in a non destructive way. It allows measurements on surfaces by selecting the incidence angle of the x-ray. These techniques can be used in-situ to investigate growth, annealing or gas exposure. The use of high brilliance synchrotron radiation can provide a strong signal to noise ratio.

Grazing Incidence X-Ray Scattering (GIXS) techniques are highly surface sensitive. They have several advantages over microscopy. For example, GISAXS (grazing incidence small angle X-ray scattering) provides better statistics as it probes several square millimeters and measures the average structure on the sample surface. The technique is nondestructive, provided the sample can endure hard x-ray exposure. By varying the incident angle of the x-ray beam on the sample surface, the technique can probe sample surfaces, buried interfaces, as well as the bulk of samples. It can probe samples from ultra-high vacuum to atmospheric environments. It can follow in situ chemical reactions without any special sample preparation contrary to the microscopy techniques. It provides morphological information from nanometer to micrometer dimensions. Grazing incidence wide angle X-ray scattering (GIWAXS) technique provides atomic arrangement and strain state information on the same sample surface. GISAXS and GIWAXS techniques can be combined to investigate the sample completely. Compositional informations also may be obtained by performing anomalous scattering close to an absorption edge, which enhances the chemical contrast of a given element. But the techniques also have limitations. Synchrotron radiation is required because the scattered signal is proportional to the

amount of material, making it difficult to measure low density material. With the X-ray scattering techniques, all the information is in reciprocal space and usually needs to be converted to real space. Also, as only the scattered intensity can be recorded, any phase information is lost, which sometimes makes it very difficult to fit the data and most often requires some assumptions in the modeling of the data.

Third generation synchrotron beams are intense enough to permit experiments in solution and at L/L interfaces with the time resolution required to follow particles growth from very early stages. There are recent reports on using synchrotron X-ray scattering techniques to probe the growth of AuNPs from homogeneous solution [1, 7]. The high brilliance X-rays from 3rd generation synchrotron sources and the improvement in focusing optics have enabled advanced synchrotron techniques to be used at L/L interfaces. Synchrotron X-ray reflectivity technique has been used to investigate the structure of L/L interfaces [28]. The technique also has been used to probe formation of AuNPs at the L/L interface where the very last stages of growth were explored [27]. Small angle X-ray scattering (SAXS) technique was used to study the response of adsorbed AuNPs to the changes in surface pressure at the L/L interface [18]. In-situ GISAXS was used to probe the self assembly of *CdSe* and *CdS* nanorods (NRs) at the interface of air and liquid [23].

CHAPTER 2

THEORY: X-RAY SCATTERING TECHNIQUES

2.1 Introduction

This chapter presents a theoretical formalism for the experimental studies in later chapters. In this thesis, grazing incidence small angle X-ray scattering (GISAXS) was used to probe the growth of AuNPs at the electrified L/L interface. GISAXS is a characterization technique used to study nanoscale structures at surfaces, interfaces, buried surfaces and thin films. GISAXS probes the same length scales as small angle X-ray scattering (SAXS) and has the surface sensitivity of grazing incidence diffraction (GID). In the GISAXS technique, a beam of X-rays is scattered from a flat surface at a small grazing angle of incidence, typically less than the critical angle of the surface. The small incidence angle enhances the surface sensitivity due to the evanescent wave which occurs for total external reflection and the increased path of X-rays within the surface. The recorded scattering pattern is analyzed to deduce averaged informations, like nanoobjects size, shape, size distribution, inter-nanoobjects distance, etc. from an assembly of nanoobjects on the surface.

In the first Section 2.2 of this chapter the interaction of X-rays with matter is introduced. In Section 2.3 X-ray propagation at interfaces is described after the introduction to refraction index. The concept of the Fresnel coefficients, X-ray penetration depth and the total reflection phenomena is described. In Section 2.4, the reflection and transmission phenomena in a layer

sample are described. The problem of scattering is introduced in Section 2.5. Perturbation treatments known as the Born and Distorted wave approximation are discussed.

While the references are mentioned in this chapter wherever possible, the principles of grazing incidence x-ray scattering are mainly compiled from few excellent textbooks and review articles. The textbook by Als-Nielsen and McMorrow provides an excellent introduction to the field of X-ray scattering [2], Ezquerro, Garcia-Gutierrez, Nogales, and Gomez cover the application of x-ray scattering techniques [8] while Renaud, Gilles, Lazzari, and Leroy review the GISAXS technique [25].

2.2 Interaction of X-rays with matter

2.2.1 Scattering by an electron

When the electric field of an X-ray interacts with an electron, it oscillates and radiates a spherical wave. If an electron of mass m_e oscillates at a frequency ω under the influence of the incident electric field, E_o , the acceleration of the electron, a , seen by an observer at a distance R at an angle Ψ with the direction of propagation in the plane of polarization can be written as,

$$a(t') = \frac{-e}{m_e} E_0 \exp(-i\omega t') \cos \psi \quad (2.1)$$

where, $t' = t - \frac{R}{c}$ is the time of propagation of the scattered wave from source to the observer.

As the intensity of the scattered wave at a point R is proportional to $\frac{1}{R^2}$, the amplitude of the radiated electric field is proportional to $\frac{1}{R}$. The electric field at R is also proportional to

the charge of the electron, $-e$ and acceleration $a(t')$ seen by the observer at R. Hence, electric field of the scattered wave at R at time t is,

$$E_s(R, t) = \frac{-e}{4\pi\epsilon_0 c^2 R} a(t') = -\frac{e^2}{4\pi\epsilon_0 c^2} \frac{E_0}{R m_e} \exp\left(\frac{i\omega R}{c}\right) \cos \Psi \quad (2.2)$$

where, the factor $\frac{1}{4\pi\epsilon_0 c^2}$ produces the correct SI units. Equation 2.2 derived by writing the scattered electric field in terms of the scattered power given by the Larmor formula. The constant factor, $\frac{1}{4\pi\epsilon_0 c^2}$ in Eq. 2.2 is defined as the Thomson scattering length or classical electron radius, r_0 , the value of which is $2.818 \times 10^{-5} \text{ \AA}$. The term $\frac{\exp\left(\frac{i\omega R}{c}\right)}{R} = \frac{\exp(ikR)}{R}$ illustrates a spherical wave. Then Eq. 2.2 becomes,

$$E_s(R, t) = -E_0 \frac{r_0}{R} \exp(ikR) \cos \Psi \quad (2.3)$$

A more generalized form of Eq. 2.3 is,

$$E_s(R, t) = -E_0 \frac{r_0}{R} \exp(ikR) P \quad (2.4)$$

where P is the polarization term which is given by:

$$P = \begin{cases} 1 & \text{Observer is in the perpendicular plane of polarization} \\ \cos \Psi & \text{Observer is in the horizontal plane of polarization} \\ \sqrt{\frac{1}{2}(1 + \cos^2 \Psi)} & \text{Unpolarized source} \end{cases} \quad (2.5)$$

2.2.2 Scattering in reciprocal space

X-ray scattering techniques probe nanoobjects by exploring reciprocal space. Therefore, before considering the scattering from an assembly of electrons, the introduction to reciprocal space is required. If the real space lattice is described by three perpendicular primitive vectors, a_1, a_2, a_3 , then the reciprocal space lattice vectors are defined as,

$$\begin{aligned} b_1 &= \frac{a_2 \times a_3}{a_1 \cdot a_2 \times a_3} \\ b_2 &= \frac{a_3 \times a_1}{a_1 \cdot a_2 \times a_3} \\ b_3 &= \frac{a_1 \times a_2}{a_1 \cdot a_2 \times a_3} \end{aligned}$$

Now, X-ray scattering geometry is considered where the incident X-ray beam of wave vector \vec{k}_{in} makes an angle α_i with the sample surface as shown in [Figure 2](#). The scattered X-ray wave vector \vec{k}_{out} , makes an angle α_f with respect to the sample surface and an in-plane angle $2\theta_f$ with respect to transmitted beam. The wave vector transfer, Q is defined as the difference

between k_{in} and k_{out} . Q is often decomposed into its components Q_x , Q_y and Q_z and are related to α_f and $2\theta_f$ according to:

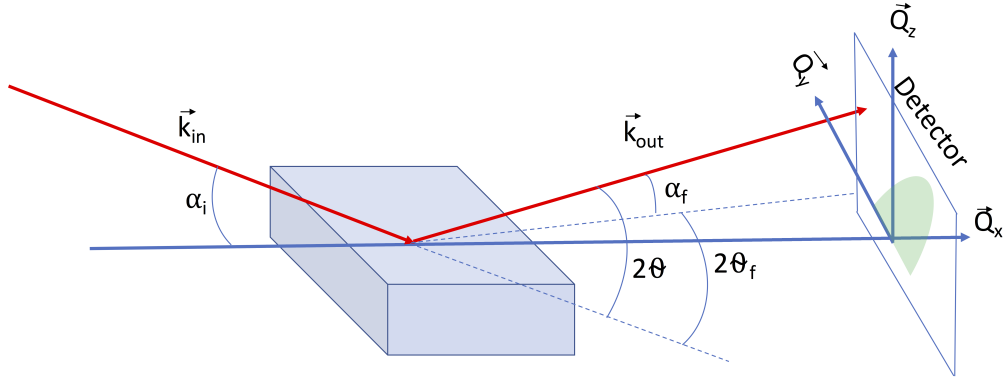


Figure 2: X-ray scattering geometry

$$Q_x = k_0[\cos(2\theta_f) - \cos \alpha_i]$$

$$Q_y = k_0[\sin(2\theta_f) \cos \alpha_i]$$

$$Q_z = k_0[\sin(\alpha_f) + \sin \alpha_i]$$

where, $k_0 = \frac{2\pi}{\lambda}$ given λ is the wavelength of the X-ray.

For specular X-ray reflectivity (XRR) experiments, $\alpha_i = \alpha_f$, Hence, $Q_x = Q_y = 0$ and $Q = Q_z$. XRR only probes structures normal to the sample surface. The in-plane structures are obtained by probing along Q_x and Q_y .

2.2.3 Scattering by an atom

Now, X-ray scattering from an atom of Z electrons is considered. The electron number density of the atom is $\rho(r)$. The scattered electric field is now a superposition of radiation from different volume from the volume distribution. Let's assume, two incident waves (\vec{k}_{in}), one interacting at the origin and other at position \vec{r} as illustrated in [Figure 3](#). The phase difference between the incident waves is $\vec{k}_{in} \cdot \vec{r}$. Similarly, the phase difference between the scattered waves (\vec{k}_{out}) is $\vec{k}_{out} \cdot \vec{r}$. Hence, the total phase difference due to scattering is,

$$\Delta\Phi(\vec{r}) = (\vec{k}_{out} - \vec{k}_{in}) \cdot \vec{r} = \vec{Q} \cdot \vec{r} \quad (2.6)$$

where $\vec{Q} = \vec{k}_{out} - \vec{k}_{in}$ is the wave vector transfer. The total scattering length from the entire atom is,

$$-r_0 f^0(\vec{Q}) = -r_0 \int \rho(\vec{r}) \exp(i\vec{Q} \cdot \vec{r}) d\vec{r} \quad (2.7)$$

where $f^0(\vec{Q})$ is the atomic form factor. This is actually the Fourier transform of the electron density. In the limit of $Q = 0$, all the electrons in the atom scatters in phase, and $f^0 = Z$. In the other limit where $Q \rightarrow \infty$, $f^0 = 0$, different volume scatters out of phase. In reality the model of an atom with uniform electron density is not valid. Atomic electrons are governed by

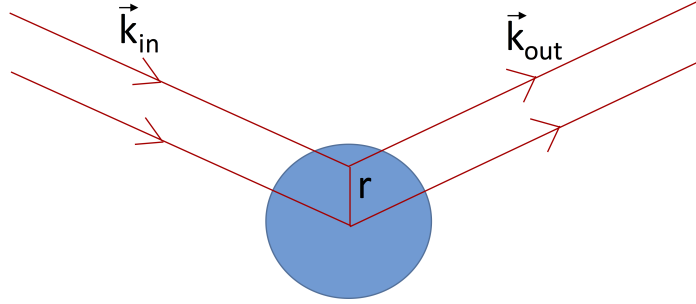


Figure 3: The incident wave vector \vec{k}_{in} is scattered by an atom in the direction of scattered wave vector \vec{k}_{out} at the origin and at position \vec{r}

quantum mechanics and has discrete energy level. Electrons are most tightly bound in the K level, while L, M levels are less tightly bound. If the energy of the X-rays is less than the energy of K level, the response of the electron to the incident will be reduced by the fact that they are bound. This reduction is described by f' . $f' = 0$ when X-ray energy is above the binding energy of the electron and $f' \neq 0$ below the binding energy of the electron. There can be an additional phase lag for the binding of the electrons, which is described by f'' . Combining all this factor, atomic form factor comes to,

$$f(\vec{Q}, E) = f^0(\vec{Q}) + f'(E) + if''(E) \quad (2.8)$$

f' and f'' are known as dispersion corrections. The dispersion corrections are most influential when the x-ray energy matches the atomic absorption edges.

2.3 propagation of X-rays at interfaces

2.3.1 The refractive index, n

The index of refraction, n of a medium is defined as the ratio of phase velocities in the vacuum, c to the medium, v ,

$$n = \frac{c}{v} \quad (2.9)$$

In case of visible light n is greater than one, but for X-rays, n is less than one. The deviation from unity is very small, in the order of $\approx 10^{-5}$. Generally for X-rays, n is described as,

$$n = 1 - \delta - i\beta \quad (2.10)$$

where, δ and β are given by,

$$\delta = \frac{\rho_e \lambda^2}{2\pi} \quad (2.11)$$

$$\beta = \frac{\mu}{2k} \quad (2.12)$$

In Eq. 2.12, μ is the absorption coefficient.

2.3.2 Snell's law, Fresnel coefficients and penetration depth

X-ray is an electromagnetic wave and the time independent form of the associated electric field has the form $\vec{E} = \vec{E}_0 \exp(i\vec{k} \cdot \vec{r})$. [Figure 4](#) shows the propagation of X-rays at an interface.

The incident and reflected wave vectors in the medium with index of refraction n_1 , are \vec{k}_i and \vec{k}_r , and \vec{k}_t is the transmitted wave vector in the medium with index of refraction, n_2 .

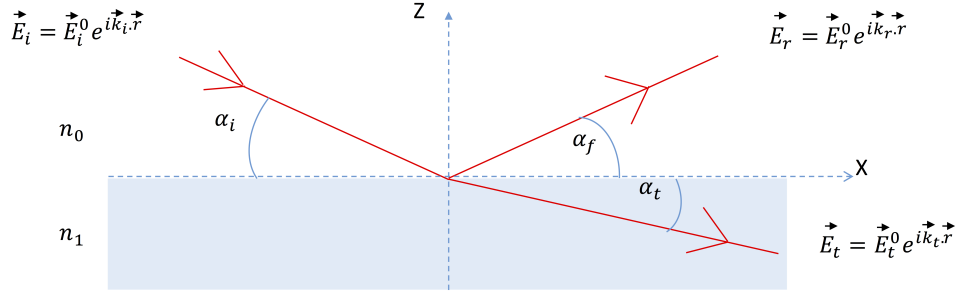


Figure 4: Incident X-rays are reflected and refracted at the interface $z = 0$

The waves and it's derivatives must be continuous at an interface. Imposing this boundary condition at $z = 0$ yields:

$$\left| \vec{E}_i^0 \right| + \left| \vec{E}_r^0 \right| = \left| \vec{E}_t^0 \right| \quad (2.13)$$

$$\vec{k}_i \left| \vec{E}_i^0 \right| + \vec{k}_r \left| \vec{E}_r^0 \right| = \vec{k}_t \left| \vec{E}_t^0 \right| \quad (2.14)$$

In the case of specular reflectivity, $\alpha_i = \alpha_r$. Resolving the parallel and perpendicular components of Eq. 2.14:

$$k_i \left(\left| \vec{E}_i^0 \right| + \left| \vec{E}_r^0 \right| \right) \cos \alpha_i = k_t \left| \vec{E}_t^0 \right| \cos \alpha_t \quad (2.15)$$

$$k_i, r(|E_i^0| - |E_r^0|) \sin \alpha_{i,r} = k_t |E_t^0| \sin \alpha_t \quad (2.16)$$

Now, from the definition of index of refraction:

$$\left| \frac{\vec{k}_i}{n_1} \right| = \left| \frac{\vec{k}_r}{n_1} \right| = \left| \frac{\vec{k}_t}{n_2} \right| \quad (2.17)$$

Combining Eqs. 2.13, 2.17 and 2.15 derives Snell's law:

$$n_0 \cos \alpha_i = n_1 \cos \alpha_t \quad (2.18)$$

The critical angle, α_c for total external reflection is defined as the incident angle for which $\alpha_t = 0$. Expanding the cosines in Eq. 2.18 and assuming $n_0 = n_{vacuum} = 1$ and negligible absorption ($\beta = 0$) in the transmitted medium lead to the derivation of α_c :

$$\alpha_c \approx \sqrt{2(1 - n_1)} \approx \sqrt{2\delta} = \sqrt{\frac{4\pi\rho_e r_e}{k^2}} \quad (2.19)$$

Also, combining Eqs. 2.13 and 2.16 follows:

$$\frac{E_i^0 - E_r^0}{E_i^0 + E_r^0} = \frac{|\vec{k}_t| \sin \alpha_t}{|k_i| \sin \alpha_i} = \frac{n_1 \sin \alpha_t}{n_0 \sin \alpha_i} \quad (2.20)$$

From which the Fresnel amplitude reflectivity, r and transmittivity, t are derived as:

$$r = \frac{E_r^0}{E_i^0} = \frac{n_0 \alpha_i - n_1 \alpha_t}{n_0 \alpha_i + n_1 \alpha_t} \quad (2.21)$$

$$t = \frac{E_t^0}{E_i^0} = 1 + \frac{E_r^0}{E_i^0} = 1 + \frac{n_0\alpha_i - n_1\alpha_t}{n_0\alpha_i + n_1\alpha_t} = \frac{2n_0\alpha_i}{n_0\alpha_i + n_1\alpha_t} \quad (2.22)$$

Equivalently, r and t can also be expressed in term of k_z .

$$r = \frac{E_r^0}{E_i^0} = \frac{k_{z,i} - k_{z,t}}{k_{z,i} + k_{z,t}} \quad (2.23)$$

$$t = \frac{E_t^0}{E_i^0} = \frac{2k_{z,i}}{k_{z,i} + k_{z,t}} \quad (2.24)$$

2.3.3 X-ray penetration depth, Λ

Again, expansion of cosine in Eq. 2.15 yields:

$$\alpha_t = \sqrt{\alpha_i^2 - \alpha_c^2 - 2i\beta} \quad (2.25)$$

α_t can be decomposed into real and imaginary parts.

$$\alpha_t = Re(\alpha_t) + iIm(\alpha_t) \quad (2.26)$$

Transmitted wave E_t can be rewritten as,

$$E_t^0 \exp(ik\alpha_t z) = E_t^0 e^{ikRe(\alpha_t)z} e^{-kIm(\alpha_t)z} \quad (2.27)$$

also, experimentally, it is seen, transmitted wave decays exponentially into the matter with increasing depth. Hence, the intensity decays with $\frac{1}{e^\Lambda}$, where λ is the penetration depth and is given by,

$$\Lambda = \frac{1}{2k\text{Im}(\alpha_t)} \quad (2.28)$$

2.4 Fresnel reflection and transmission in layered samples

2.4.1 Thin film

A thin film of thickness Δ is considered to calculate the Fresnel reflectivity. Unlike a slab of infinite thickness where there is only one possible reflection and transmission process, the reflection and transmission processes take place at multiple interfaces in a thin film. Equation [Figure 5](#) illustrates The possible X-ray beam path in a thin film of thickness Δ . X-rays are reflected at the interface of 0 and 1 with an amplitude r_{10} . The transmitted wave with an amplitude t_{10} is again reflected from the interface of 1 and 2, the amplitude of which is $t_{10}r_{21}$. The total reflectivity therefore is,

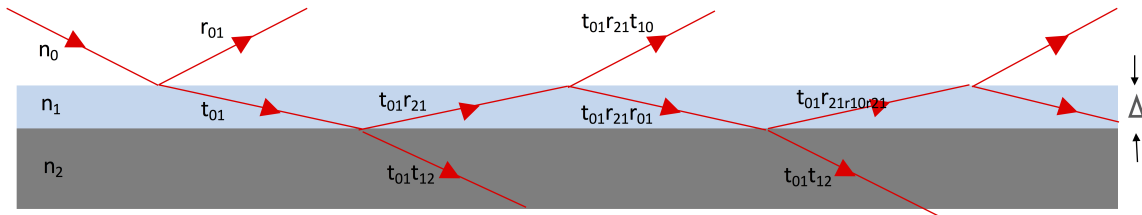


Figure 5: Reflection and transmission in a layer of thickness Δ

$$r_{total} = r_{10} + t_{01}r_{21}t_{10}p^2 + t_{01}r_{21}r_{10}r_{21}t_{10}p^4 + \cdots = r_{10} + t_{10}t_{01}r_{21}p^2 \sum_{m=0}^{\infty} (r_{01}r_{21}p^2)^m \quad (2.29)$$

where the phase factor p^2 is,

$$p^2 = \exp(iQ_1\Delta) \quad (2.30)$$

Here, $Q_1 = 2k_1 \sin \alpha_1$. Equation 2.29 is a geometric series which can be simplified using Eqs. 2.21 and 2.22 to give:

$$r_{total} = r_{10} + \frac{t_{01}r_{21}t_{10}p^2}{1 + r_{10}r_{21}p^2} \quad (2.31)$$

Using the Fresnel's in 2.23 and 2.24, 2.31 can be simplified furthermore to give:

$$r_{total} = \frac{r_{10} + r_{21}p^2}{1 + r_{10}r_{21}p^2} \quad (2.32)$$

The reflectivity given Eq. 2.32 displays oscillations due to the interference of reflected waves from the interfaces at different depths which are known as Kiessig fringes. The thickness of the film can be obtained from the period of the Kiessig fringes by Eq. 2.33 where θ_m is the location of m^{th} fringe.

$$\Delta = \frac{\lambda}{\theta_{m+1} - \theta_m} \quad (2.33)$$

2.4.2 Multilayers

The calculation of reflectivity can be extended from single layer to multilayer. For this, a multilayer of N layers is considered. The j_{th} layer, with a thickness of Δ_j is assumed to have index of refraction n_j . The reflectivity calculation starts with the lowermost N_{th} layer which is supported by an infinite substrate. According to Eq. 2.23, the reflectivity at the interface of N_{th} layer and the substrate is,

$$r_{N,\infty} = \frac{k_z^N - k_z^\infty}{k_z^N + k_z^\infty} \quad (2.34)$$

Applying Eq. 2.32, the reflectivity at the interface of j^{th} and $(j-1)^{th}$ is given by,

$$r_{j-1,j} = \frac{r_{j,j-1} + r_{j+1,j} p_j^2}{1 + r_{j,j-1} r_{j+1,j} p_j^2} \quad (2.35)$$

Equation 2.35 is applied recursively from N_{th} layer to the top layer to calculate the reflectivity at $r_{0,1}$. This method was described by Parratt and is known as Parratt's exact recursive method [20]. The reflected intensity from the sample of N layers is given by,

$$\frac{I_R}{I_0} = |r_{1,0}|^2 \quad (2.36)$$

2.4.3 Effect of surface roughness on the Fresnel reflectivity

A real interface is rarely perfectly flat. There is some degree of randomness in the height of the surface. This is called surface roughness. Surface roughness dampens the reflectivity

as part of the incidents X-rays are scattered out of the specular direction. The reflection and transmission coefficients of a flat surface which is assumed to fluctuate by $z_{j+1}(r_{||})$ from it's vertical position Z_{j+1} , decrease at high Q value by a factor, which is known as Nevot-Croce factor [?] and are given by,

$$r_{j,j+1} = r_{j,j+1(Fresnel)} e^{-2k_{z,j}k_{z,j+1}\langle z_{j+1}^2(r_{||}) \rangle}$$

$$t_{j,j+1} = t_{j,j+1(Fresnel)} e^{(k_{z,j}-k_{z,j+1})\frac{\langle z_{j+1}^2(r_{||}) \rangle}{2}}$$

2.5 Off-specular scattering

Specular reflectivity measures intensity reflectivity, R as a function of $Q(z)$ which only allows to probe out of plane structure. The in-plane component of Q , Q_{xy} measures the in-plane nature of the interface. As previously mentioned, the interface may have fluctuations in it's vertical position, known as surface roughness. There are different approaches to calculate scattered X-rays from a rough surface. In the kinematical Born approximation, the scattering from a sharp but rough interface is calculated by assuming the scattering is weak, so that multiple scattering can be ignored. Distorted wave Born approximation is a more advanced method to calculate scattering from a rough surface which takes into account multiple scattering near critical angle.

2.5.1 Scattering in the kinematical Born approximation

First order Born approximation is applicable to weakly scattered X-rays. In this model, it is assumed the scattered waves are parallel at the detector. This assumption simplifies the mathematical modeling but is not applicable to strong scattering close to the critical angle.

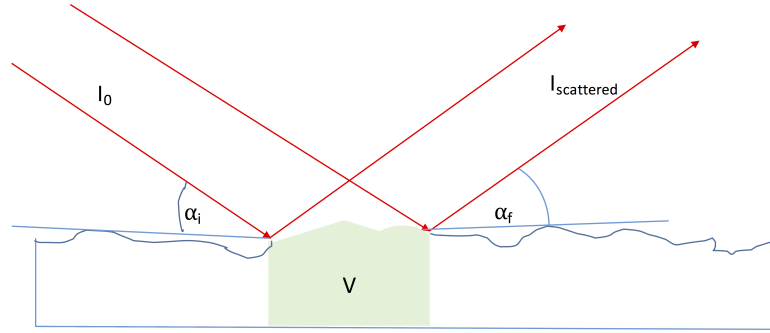


Figure 6: Scattering from a rough surface

An X-ray beam of intensity I_0 is considered which incidents on a rough surface which illuminates a volume V in the sample as illustrated in [Figure 6](#). The total scattered amplitude is calculated by integrating scattering from all the volume elements $d\vec{r}$ in V incorporating the phase factors.

$$r_V = -r_0 \int_V (\rho d\vec{r}) e^{i\vec{Q} \cdot \vec{r}} \quad (2.37)$$

It is assumed, the X-ray footprint is much larger than the thickness of volume V, therefore lateral surfaces in the volume is negligible. also, the X-ray is fully absorbed before reaching the lower surface of V. The relevant surface in this case is solely the topmost surface. By using Gauss's theorem, Eq. 2.37 can be written as,

$$r_S = r_0 \int_V (\rho d\vec{r}) e^{i\vec{Q} \cdot \vec{r}} = -r_0 \rho \left(\frac{1}{iQ_z} \right) \int_S \hat{z} \cdot d\vec{S} e^{i\vec{Q} \cdot \vec{r}} \quad (2.38)$$

The scalar product $\hat{z} \cdot d\vec{S}$ is the projected area on the x-y plane and $\hat{z} \cdot d\vec{S} = dxdy$. So,

$$r_S = -r_0 \rho \left(\frac{1}{iQ_z} \right) \int_S e^{i\vec{Q} \cdot \vec{r}} dxdy \quad (2.39)$$

If the height fluctuations on the surface is expressed by a height-height correlation function, $h(x, y)$, then $\vec{Q} \cdot \vec{r}$ can be written as,

$$\vec{Q} \cdot \vec{r} = Q_x x + Q_y y + Q_z h(x, y) \quad (2.40)$$

So, now Eq. 2.39 becomes,

$$r_S = -r_0 \rho \frac{1}{iQ_z} \int_S e^{i(Q_x x + Q_y y)} \cdot e^{iQ_z h(x, y)} dxdy \quad (2.41)$$

Hence, The differential scattering cross-section ($\frac{d\sigma}{d\omega}$) which is defined as the absolute square of the scattering amplitude, is given by,

$$\frac{d\sigma}{d\omega} = \left(\frac{r_0\rho}{Q_z}\right)^2 \int_S e^{i[Q_x(x-x') + Q_y(y-y')]}. e^{iQ_z[h(x,y) - h(x',y')]} dx dx' dy dy' \quad (2.42)$$

If $h(x, y) - h(x', y')$ is assumed to only depend on $(x - x', y - y')$, the 4-dimensional integration in Eq. 2.42 reduces to 2-dimensional integration and $\int dx dy = \frac{A_0}{\sin \alpha_i}$, where $\frac{A_0}{\sin \alpha_i}$ is the illuminated surface area. Equation 2.42 acn be rewritten as:

$$\left(\frac{d\sigma}{d\omega}\right) = \left(\frac{r_0\rho}{Q_z}\right)^2 \left(\frac{A}{\sin \alpha_i}\right) \int_S e^{i[Q_x(x) + Q_y(y)]}. \langle e^{iQ_z[h(0,0) - h(x,y)]} \rangle dx dy \quad (2.43)$$

If the statistics of the height variations are assumed to be Gaussian, $g(x, y) = \langle e^{iQ_z[h(0,0) - h(x,y)]} \rangle^2$, the scattering cross-section can be rewritten as,

$$\left(\frac{d\sigma}{d\omega}\right) = \left(\frac{r_0\rho}{Q_z}\right)^2 \left(\frac{A}{\sin \alpha_i}\right) \int_S e^{i[Q_x(x) + Q_y(y)]}. e^{-Q^2 \frac{g(x,y)}{2}} dx dy \quad (2.44)$$

In the case of Fresnel reflectivity from a flat, sharp interface, $h(x, y)$ for all X and Y, so the Eq. 2.44 reduces to:

$$\left(\frac{d\sigma}{d\omega}\right)_{Fresnel} = \left(\frac{r_0\rho}{Q_z}\right)^2 \left(\frac{A}{\sin \alpha_i}\right) \int_S e^{i[Q_x(x) + Q_y(y)]} dx dy \quad (2.45)$$

The double integral in Eq. 2.45 can be shown to be equal to $(2\pi)^2 \delta(Q_x) \delta(Q_y)$ by Fourier transformation, Thus,

$$\left(\frac{d\sigma}{d\omega}\right)_{Fresnel} = (2\pi \frac{r_0 \rho}{Q_z})^2 \left(\frac{A}{\sin \theta_i}\right) \delta(Q_x) \delta(Q_y) \quad (2.46)$$

For a completely uncorrelated surface, $g(x, y)$ can be rewritten as,

$$g(x, y) = \langle [h(0, 0) - h(x, y)]^2 \rangle = \langle h(0, 0)^2 \rangle + \langle h(x, y)^2 \rangle + 2\langle h(0, 0) \rangle \langle h(x, y) \rangle = 2\langle h^2 \rangle = 2\sigma^2 \quad (2.47)$$

Hence, the differential scattering cross section for an uncorrelated surface,

$$\left(\frac{d\sigma}{d\omega}\right)_{uncorrelated \text{ rough surface}} = \left(\frac{r_0 \rho}{Q_z}\right)^2 \left(\frac{A}{\sin \alpha_i}\right) e^{-Q_z^2 \sigma^2} \int_S e^{i[Q_x(x) + Q_y(y)]} dx dy \quad (2.48)$$

Substituting Eq. 2.46 in Eq. 2.48 reduces to,

$$\left(\frac{d\sigma}{d\omega}\right)_{uncorrelated \text{ rough surface}} = \left(\frac{d\sigma}{d\omega}\right)_{Fresnel} e^{-Q_z^2 \sigma^2} \quad (2.49)$$

Equation 2.49 shows, uncorrelated rough surface does not contribute to off-specular scattering rather it reduces Fresnel reflectivity by a factor.

Now, the correlated surfaces are considered where $g(x, y)$ is assumed to have the following form, The second case is to consider where height differences are within limit as $r \rightarrow \infty$. In this case, $g(x, y)$ can be written as,

$$g(x, y) = \langle [h(0, 0) - h(x, y)]^2 \rangle = 2\langle h^2 \rangle - 2\langle (0, 0)h(x, y) \rangle = 2\sigma^2 - 2C(x, y) \quad (2.50)$$

Here, $C(x, y) = \langle h(0, 0)h(x, y) \rangle$ is the correlation function. Equation 2.43 now reduces to,

$$\left(\frac{d\sigma}{d\omega}\right) = \left(\frac{r_0\rho}{Q_z}\right)^2 \left(\frac{A}{\sin \alpha_i}\right) e^{-Q_z^2\sigma^2} \int e^{Q_z^2 C(x,y)} e^{i(Q_x x + Q_y y)} dx dy \quad (2.51)$$

Equation 2.51 can be rewritten as,

$$\left(\frac{d\sigma}{d\omega}\right) = \left(\frac{r_0\rho}{Q_z}\right)^2 \left(\frac{A}{\sin \alpha_i}\right) e^{-Q_z^2\sigma^2} \int [e^{Q_z^2 C(x,y)} - 1 + 1] e^{i(Q_x x + Q_y y)} dx dy \quad (2.52)$$

The last term in the square bracket in the above Eq. can be recognized as the specular reflectivity for uncorrelated surface from Eq. 2.49. Therefore, the total cross-section is rewritten as,

$$\begin{aligned} \left(\frac{d\sigma}{d\omega}\right)_{total} &= \left(\frac{r_0\rho}{Q_z}\right)^2 \left(\frac{A}{\sin \alpha_i}\right) e^{-Q_z^2\sigma^2} \int [e^{Q_z^2 C(x,y)} - 1 + 1] e^{i(Q_x x + Q_y y)} dx dy \\ &= \left(\frac{d\sigma}{d\omega}\right)_{Fresnel} e^{-Q_z^2\sigma^2} + \left(\frac{d\sigma}{d\omega}\right)_{diffuse} \end{aligned} \quad (2.53)$$

where,

$$\left(\frac{d\sigma}{d\omega}\right)_{diffuse} = \int [e^{Q_z^2 C(x,y)} - 1] e^{i(Q_x x + Q_y y)} dx dy \quad (2.54)$$

Therefore, the scattering from a correlated surface where the height differences are bounded, can be decomposed to two components. The scattering has a sharp specular component superimposed on a diffuse component.

2.5.2 Distorted wave Born approximation

Born approximation calculates the interaction between the matter and the X-rays by assuming the wave vectors inside the material are same as it is in the vacuum above it. It is valid for weak scattering, typically when α_i and $\alpha_d \geq \alpha_c$. But when $\alpha \leq \alpha_c$, the Born approximation is no longer valid. In this limit, the scattering becomes so strong that multiple scattering has to be considered. Distorted Wave Born Approximation (DWBA) theory is an extension of Born approximation, which takes into account multiple scattering.

The distorted wave Born approximation (DWBA) calculates the scattering by considering the roughness as a perturbation on the perfect interface, hence it starts with the Fresnel solution of the flat interface and then calculates the effect of the perturbing wavefront. The scattering potential is separated into two terms V_1 and V_2 where the total potential is $V = V_1 + V_2$. The ideal surface located at $z = 0$, is described as:

$$V_1 = \begin{cases} k_0^2(1 - n^2) & z < 0 \\ 0 & z > 0 \end{cases} \quad (2.55)$$

The perturbing potential due to roughness at depth z is described by

$$V_2 = \begin{cases} k_0^2(1 - n^2) & 0, z < Z(x, y) \\ -k_0^2(1 - n^2) & 0 > z > Z(x, y) \\ 0 & \text{otherwise} \end{cases} \quad (2.56)$$

where $Z(x, y)$ is the actual rough surface. Using this perturbing potential the diffuse scattering cross section within the DWBA as:

$$\begin{aligned} \left(\frac{d\sigma}{d\omega}\right)_{DWBA} = & \left(\frac{r_0\rho}{Q_z^t}\right)^2 \left(\frac{A}{\sin \alpha_i}\right) |t(k_1)|^2 |t(k_2)|^2 (1 - n^2) \exp\left\{-\frac{\sigma^2}{2}[(Q_z^t)^2 + (Q_z^{t*})^2]\right\} \\ & \times \int_{-\infty}^{\infty} (\exp\{|Q_z^t|C(R)\} - 1) \exp\{i(Q_x X + Q_y Y)\} dx dy \quad (2.57) \end{aligned}$$

Here $|t(\vec{k}_i)|$ is the Fresnel transmission coefficient from medium i . In the medium, the wavevector transfer is Q_z^t . Above the critical angle, $Q_z^t \approx Q_z$.

Equation 2.57 is an modified expression of the Born approximation in Eq. 2.54. Two modifications are obvious, in the Fresnel transmission coefficients, and the modified wavevector inside the medium, Q_z^t is used.

2.5.3 Form factor of nanoparticle within DWBA

The form factor of a nanoparticle supported on a substrate can be determined analytically with DWBA. The index of refraction for the nanoparticle is assumed to be n_p , $n_0(z) = 1$ for $z > 0$, $n_0(z) = n_s$ for $z < 0$, where n_s is the index of refraction of the substrate. Figure 7 illustrates scattering by a nanoparticle in DWBA. The scattering cross section can be derived to give,

$$\frac{d\sigma}{d\omega} = \frac{k_0^4}{16\pi^2} |n_p^2 - 1|^2 |F(Q_{xy}, k_{i,z}, k_{f,z})|^2 \quad (2.58)$$

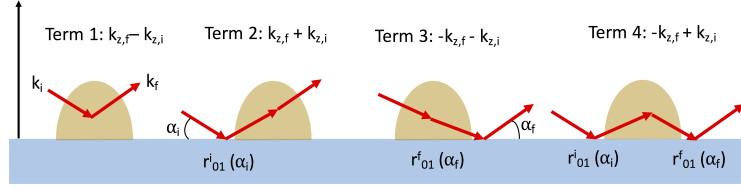


Figure 7: X-ray scattering events within DWBA

where, $F(Q_{xy}, k_{i,z}, k_{f,z})$ is the particle form factor in DWBA and can be decomposed as following,

$$\begin{aligned}
 F(Q_{xy}, k_{i,z}, k_{f,z}) &= F(Q_{xy}, k_{f,z} - k_{i,z}) + r_{0,1}^f F(Q_{xy}, -k_{f,z} - k_{i,z}) \\
 &\quad + r_{0,1}^i F(Q_{xy}, k_{f,z} + k_{i,z}) + r_{0,1}^i r_{0,1}^f F(Q_{xy}, -k_{f,z} + k_{i,z}) \quad (2.59)
 \end{aligned}$$

$F(Q_{xy}, k_{i,z}, k_{f,z})$ is also given by the Fourier transform of the particle shape,

$$F(Q) = \int e^{iQ \cdot r} dr \quad (2.60)$$

The first term in Eq. 2.59 is simply the form factor in Born approximation, *i.e* the direct scattering by the particle when it is considered to be isolated in vacuum. The other terms include reflected incident or scattered wave on the substrate, hence the corresponding form factor is weighted by corresponding reflection coefficient. At $\alpha_i = \alpha_c$, there is an enhancement in the value of $|F(Q_{xy}, k_{i,z}, k_{f,z})|^2$, because of the interplay between 1) the variation of the

phase and the amplitude of the reflection coefficients, $r_{0,1}^{i,f}$ near α_c and 2) the involved Fourier transforms $F(Q_{xy}, k_{i,z}, k_{f,z})$. This feature known as the Yoneda peak [34]. Generally, Born approximation is valid at $\alpha_i, \alpha_f \gg \alpha_c$.

2.6 Form factor and Interference function

The important feature of GISAXS technique is that it probes the morphology of nanostructures. Theoretically, the shape and size of the structures can be extracted from the form factor. But the scattered intensity is the product of two factors, form factor and structure factor, where structure factor is the Fourier transformation of nanostructures position. In a concentrated system, these two factors are strongly correlated at small Q_y . where in the case of a disordered system, the structure factor tends to one at high Q values. Hence, at high Q , form factor entirely determines the scattered intensity. Therefore, the scattered intensity must be measured far from the origin of the reciprocal space to differentiate between shapes and to measure nanostructures size and size distribution accurately. The measurements also should be carried over several orders of magnitudes for appropriate interpretation of size and shape. As the form factor decreases rapidly at high Q values, the background should be as low as possible. Many theoretical interference functions can be used to analyze the GISAXS data, such as, the Gaussian pair correlation function [26], the LennardJones pair correlation function [11], the Zhu pair correlation function [36], the Venables pair correlation function [33], the bidimensional hard core pair function [3]. The scattered intensity, I_s in a GISAXS experiment is proportional to the form factor, $F(Q)$ and the structure factor, $S(Q_{xy})$, where $S(Q_{xy})$ is the

Fourier transform of the nanostructure position. For a completely uncorrelated sample or for a dilute system, $S(Q_{xy})$ is approximated to be 1.

2.7 Effect of Polydispersity

Now, generally the nanoparticles in a suspension are polydispersed in their size and shape. For example, $|F(Q_{xy}, k_{i,z}, k_{f,z})|^2$ has zeros which are appeared as minima in the scattering intensity curve for a small polydisperse sample and for large polydisperse sample the oscillations are no more visible. The position of the minima in the case of small polydispersity can be used to determine the approximate radius of the particles. The polydispersity can be expressed by a size distribution function $D(R)$, with $\int_0^\infty D(R)dR = 1$. The scattered intensity $I(Q)$ is given by,

$$I(Q) = N \int_0^\infty D(R) |F(Q, R)|^2 dR \quad (2.61)$$

For spherical particles, the size distribution can be approximated by analytical functions, such as, Gaussian, Schulz. The polydispersity is calculated by the ratio of the RMS (root mean square) deviation of R , σ_R and the average value of R .

2.8 Limiting form of $I(Q)$

The asymptotic behavior of the form factor near the origin of reciprocal space can be well approximated by Guinier limits. The Guinier approximation in the limit, $QR_G < 1$ is,

$$I(Q) \propto e^{\frac{Q^2 R_G^2}{3}} \quad (2.62)$$

where, R_g is known as the radius of gyration. This is widely used to determine R_G from the $\log I(Q)$ vs Q^2 plot.

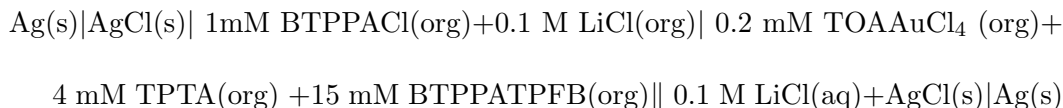
Porod approach can be applied at high Q values, typically in the range $Q_{xy}R > 3.5$ or $Q_zH > 3.5$, given R and H are the radius and the height of the particle respectively. According to Porod law, the intensity is proportional to the average of the square modulus of the form factor for a disordered system. Porod law describes, at high Q values the intensity varies with Q^{-n} where the value of n is determined by the sharpness of the shape of the nanostructure. Such as, in the parallel direction for a cylinder $n = 3$, but for a hemisphere or a pyramid the value is 4. Whereas in the perpendicular direction, $n = 2.5$ for a cylinder, 3 for a hemisphere. For a spherical particle $n = 4$ in both directions.

CHAPTER 3

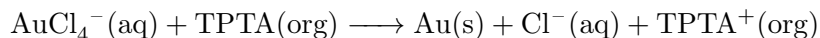
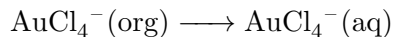
EXPERIMENTS

3.1 Gold nanoparticle synthesis

AuNPs were formed at the interface between water and 1,2-Dichloroethane (DCE) by reduction of gold ions with a weak reducing agent where both reactants were physically separated by the immiscible phases. The electrochemical cell can be represented as follows :



where || represents water-DCE interface. It is important to notice that the sample cell is prepared as gold ions and reducing agent both present in the same organic phase but they do not react to form the gold particles. This is because of the difference in reduction potential of $[\text{AuCl}_4]^-$ to Au^0 in organic and aqueous phases. The standard potential in aqueous solution for the reduction of $[\text{AuCl}_4]^-$ to Au^0 is 1.002 V , where in DCE the value is -0.9 V. So, $[\text{AuCl}_4]^-$ is stable in DCE in presence of weak reducing agent tri-(p-tolyl)amine (TPTA) but reacts upon transfer to aqueous phase. This can be presented by following simplified chemical equations:



This method of synthesizing gold nanoparticles at the interface is of great advantage to follow the growth because the distribution of $[\text{AuCl}_4]^-$ at the interface can be varied by varying

the applied potential across the interface, thus controlling the formation of particles at the interface.

3.2 Electrochemical Sample Cell

Figure 8 is a schematic diagram of the electrochemical cell. It has inner diameter of 7 cm with a cross sectional area of about 38.5 cm². The solutions are conductive because of aqueous electrolyte LiCl and organic electrolyte bis(triphenylphosphoranylidene)ammonium tetrakis(pentafluorophenyl)borate (BTPPATPFB). The four electrode glass cell can precisely measure and control the electric current and potential difference across the interface.

The counter electrodes are made of platinum wire with square platinum mesh attached to it. Platinum meshes (woven from 0.1 mm diameter wire, purchased from Alfa Aesar) have a surface area of ~ 25 cm². Large surface area distributes the applied electric field uniformly across the L/L interface. The top mesh and bottom meshes are positioned ~ 1 cm and ~ 1.5 cm from the interface respectively. AgCl coated Ag wires are used as reference electrodes. They are placed in two Luggin capillaries. The tips of these Luggin capillaries are located within a few millimeters of the interface to probe the potential drop across the interface. The top reference electrode is directly in the aqueous phase. The DCE phase reference electrode is immersed in an aqueous solution of 10 mM LiCl and 1 mM bis(triphenylphosphoranyldine)ammonium chloride (BTPPATCl), which forms a liquid junction with the organic solution for the reference electrode. The top capillary, located above with the aqueous phase, releases pressure to prevent pressure rise in the cell and the other additional capillary, entering in the DCE phase, is for adding or removing DCE to adjust the interface level.

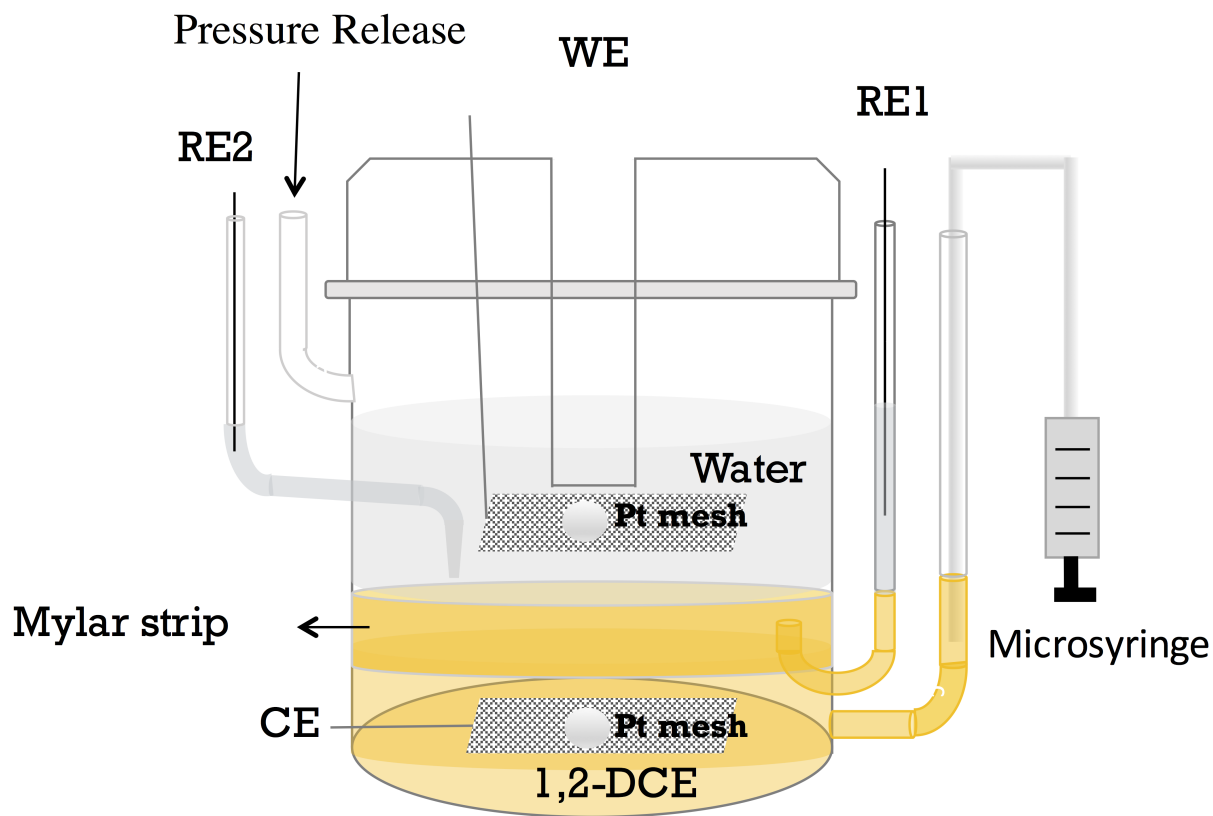


Figure 8: schematic figure of electrochemical sample cell

The extended glass tube entering the cell from the top is sealed at its bottom. It is immersed in the aqueous phase to provide a path way for laser beam in Quasi electric light scattering (QELS) measurements. The platinum meshes have ~ 2 cm diameter holes in the middle to provide passage for the laser.

Flat interface is a requirement for x-ray scattering measurements which can be achieved by pinning the interface to the glass wall and then adjusting the volume of the bottom phase. The

interface is pinned to the hydrophilic glass wall by using the top edge of a hydrophobic strip. Mylar is used for as the hydrophobic strip. Thin Mylar strip is pressed against the inner wall using a thicker Mylar to hold the thin Mylar to it's position. The top edge of the Mylar is placed approximately midway between the tips of two Luggin capillaries. The volume of the DCE phase can be adjusted by adding or removing solution using the microsyringe.

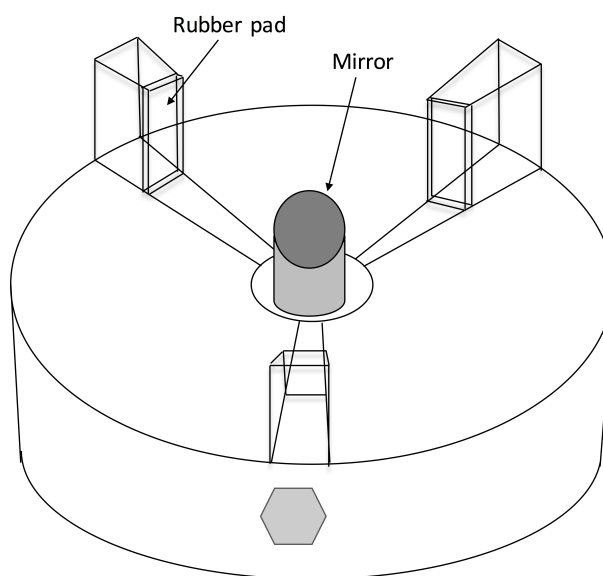


Figure 9: 3 jaw chuck

The sample cell is mounted on a 3-jaw chuck as shown in [Figure 9](#). The opening of the chuck can be adjusted with a key, which goes in the square hole at the side of the chuck. Each jaw has rubber pad attached to it to protect the glass cell.

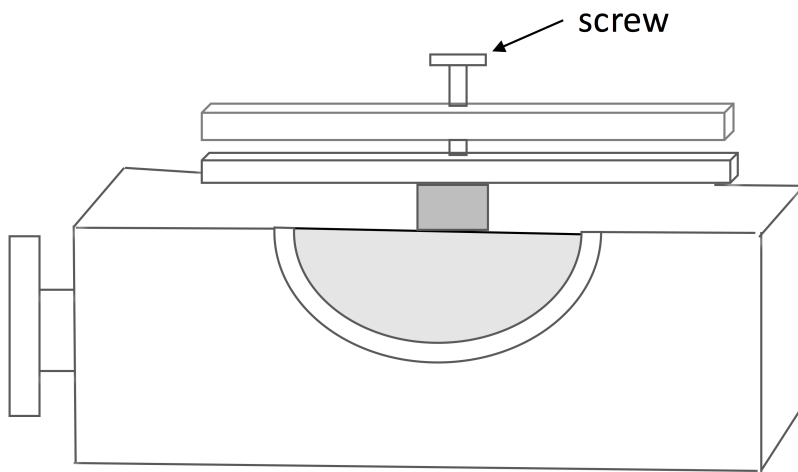


Figure 10: Tilting stage

A 45° mirror is mounted in the middle of the chuck to direct the laser beam through the solution. The chuck is again mounted on the kinematic mount and the tilting stage. Figure 10 is a drawing of the kinematic mount and tilting stage. Tilting stage levels the sample in the direction of x-ray beam while x-ray scattering measurements, where the kinematic mount levels the interface in the transverse direction of the x-ray beam in horizontal plane.

3.3 Sample Preparation

3.3.1 LiCl Purification

LiCl was roasted at high temperature to remove any organic contaminations and moisture trapped in the salt. A 40 cm long glass tube of radius 1 cm, shown in Figure 11 was used to heat up LiCl. The glass tube has 24 cm long opening on one side. Before using, the tube was cleaned in an acid bath (18 g of ammonium per sulfate in 1 liter of 98% H_2SO_4) for half an

hour. After that it was rinsed with plenty of Milli-Q water. Impure salt was put inside the tube in thin layer. The tube was wrapped with aluminum foil except one end so that moisture could escape through the open end. It was then placed in the furnace.

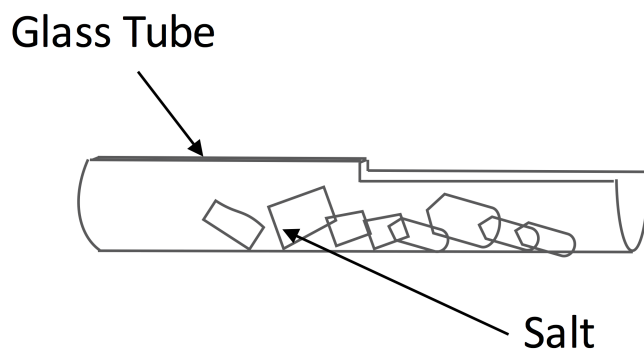


Figure 11: Glass tube to purify LiCl

The temperature of the furnace was slowly elevated to 500 °C and was maintained there. The furnace was turned off after half an hour and was allowed to cool down to room temperature. During the cooling, the open end of the tube was covered with aluminum foil to prevent the in flow of moisture and dust. Cooling down to room temperature took about 6 hours. The purified salt was stored in a clean glass bottle.

3.4 Preparation of BTPPATPFB

The preparation of the organic electrolyte, BTPPATPFB was based on metathetical reaction of the starting materials, BTPPACl and Lithium Tetrakis(Pentafluorophenyl)Borate Etharate(TPFBLi). BTPPACl was purchased from Sigma-Aldrich; and TPFBLi was purchased from Boulder Scientific Company. They were dissolved separately in a mixture of methanol and water in 2 : 1 volume ratio. The solutions were mixed together in a glass beaker. The beaker was placed on a magnetic stirrer hot plate with magnetic stir bar in it. Small volumes of the two solutions were mixed to start the reaction. First the mixture formed a gel-like material. With more addition the mixture hardened a little bit, and upon further addition the mixture precipitates into milky white material. This material was left undisturbed for an hour to allow it to form large stable crystals. It was then filtered on a circular Whatman qualitative grade 1 filter paper with diameter of 55 mm. Supernatant LiCl was discarded.

The filtered material was recrystallized from distilled acetone. To do so, 10 ml of acetone was added to impure BTPPATPFB. The mixture was heated on a hot plate and was swirled occasionally with a glass tube. Acetone was added to the solution in small amounts until BTPPATPFB was just dissolved and the solution became clear. After turning off the hot plate, the solution was allowed to cool slowly to form crystallized BTPPATPFB.

The pure crystals were separated from the mother liquor by vacuum filtration. The setup is shown in [Figure 12](#). A Buckner funnel was used to separate the crystals. A filter paper was fitted to the plate of the perforated Buckner funnel and was moistened with acetone. The solution was poured into the funnel. Vacuum was created in the flask by turning on the faucet. The

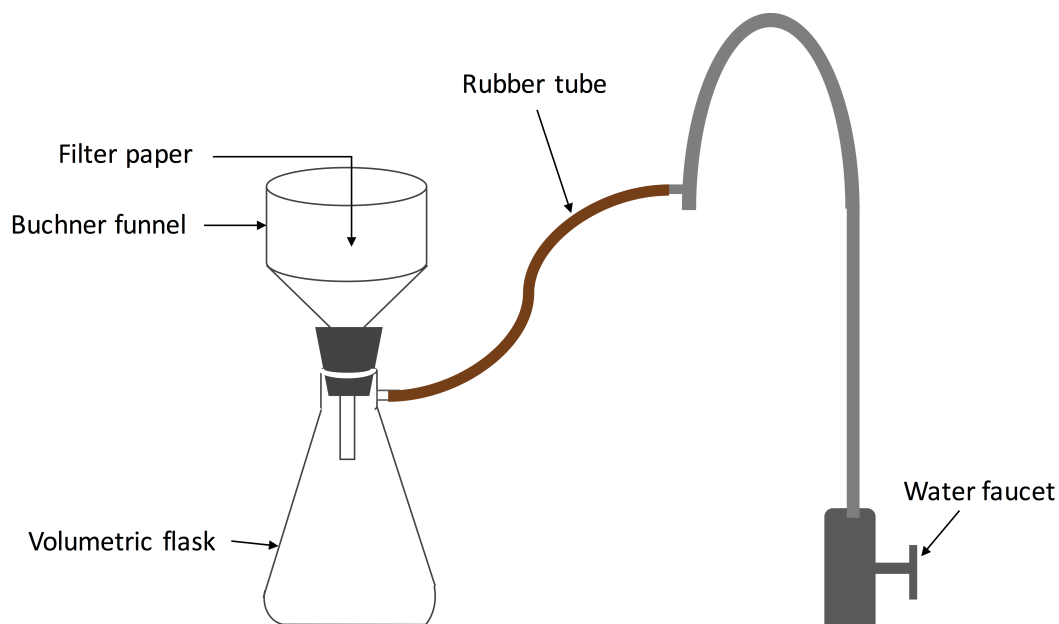


Figure 12: Recrystallization from acetone

filtered crystal was washed with cold acetone and was allowed to air-dry on the funnel. It was then transferred into a round bottom flask and was allowed to dry. The purity of the product was ensured by bright white color.

3.5 Preparation of TOAAuCl₄ solution in DCE

The metal precursor, tetraoctylammonium tetrachloroaurate (TOAAuCl₄), was prepared via phase transfer between aqueous solution of hydrogen tetrachloroaurate trihydrate (HAuCl₄·3H₂O) and organic solution of tetraoctylammonium chloride (TOACl). TOACl (0.25 g) was dissolved in 10 ml of DCE and was poured into the clean glass separatory funnel with the tap at the bottom closed. HAuCl₄·3H₂O (0.197 g) was dissolved in 15 ml of Milli-Q water and was added

into the funnel. The funnel was then closed and was shaken by inverting it several times. To release excess vapor pressure, It was periodically vented by opening the top stopper. Upon complete transfer, the light yellow upper phase became colorless. The lower DCE phase was carefully separated by opening the lower tap. The top stopper was left open during this process.

Figure 13 shows the separation of DCE phase.

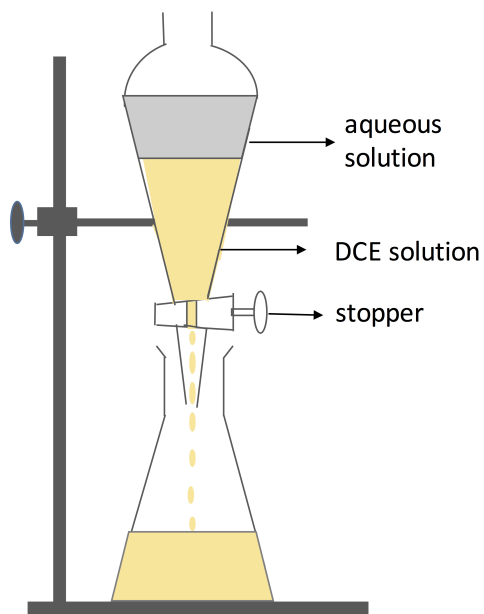


Figure 13: Setup for preparation of TOAAuCl_4

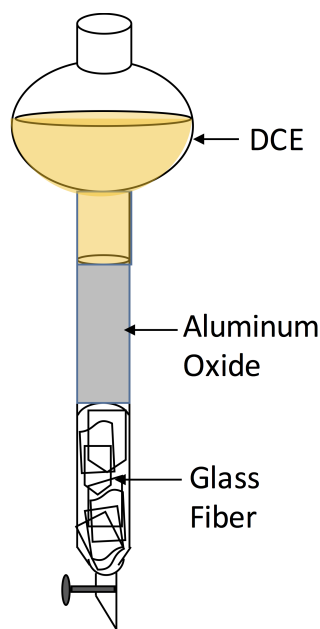


Figure 14: Setup for column chromatography

3.6 Distillation of organic solvent

Organic solvent DCE was purified by gravity column chromatography. It was passed through a 5 cm long glass column of water saturated aluminum oxide (basic alumina). Before inserting into the column, basic alumina was mixed with water in 40:1 volume ratio, and was shaken for 30 minutes with a mechanical shaker, then it was left at room temperature for 12 hours. Glass fiber was inserted in the column as a solid support so that the alumina could not flow out of the bottom of the column. From the top of the column, DCE was poured. Approximately DCE took 10 minutes to pass from top to the bottom of the column. [Figure 14](#) is a schematic drawing of the setup. First 10 ml of DCE was discarded that came out of the column because of the

possibility of the presence of unintentional alumina or glass fiber. Purified DCE was collected and stored in a clean brown bottle.

3.7 Purification of reducing agent

Tri-p-tolylamine(TTA) was recrystallized from distilled isopropanol. Measured amount of TTA was taken in an Erlenmeyer flask. It was placed on a hot plate. Isopropanol was added to the solid with a Pasteur pipette. The mixture was heated to the near boiling temperature of isopropanol. Isopropanol was added until all the solids got just dissolved. The solution was then cooled down to room temperature for recrystallization to occur. Recrystallized solid was filtered with assistance of the suction of flowing water explained elsewhere. Crystals were washed with cold isopropanol and then were left to air dry. Purified crystals were collected and stored.

3.8 Sample cell preparation

All the glassware were washed thoroughly before using. First, they were rinsed by ACS certified methanol and then acetone and then again methanol. This procedure was repeated three times and then was rinsed with plenty of ultra pure water (purity 18.2 M Ω - cm, produced by Nanopure UV Barnstead system). They were then soaked in concentrated sulfuric acid bath (18 g of ammonium persulfate in 1 liter of 98% H_2SO_4) for 6 hours. They were again rinsed with plenty of ultra pure water. The glassware were wrapped in alpha wipes and dried in an oven.

Electrochemical sample cell was rinsed following the same above mentioned procedure. It was then soaked in acid bath for half an hour. It was rinsed with plenty of water and dried

by blowing pure nitrogen gas through it. The cell was then filled with acid piranha solution (3:1 volume mixture of concentrated sulfuric acid and hydrogen peroxide, H_2O_2) to remove any organic residues that might be present. Piranha solution was prepared with great care and with all time presence of a knowledgeable user. In a clean glass beaker, H_2O_2 was added to H_2SO_4 very slowly under fume hood. All the organic material was removed from vicinity. Hot piranha solution was poured in the cell very slowly. Once the cell was filled with piranha, it was allowed to react for 45 minutes. Piranha solution was transferred back to the glass beaker and was allowed to cool down for several hours, usually overnight and then stored in a glass container for waste disposal. The sample cell was rinsed with plenty of ultra pure water. The cell was again dried with very pure nitrogen. A Pasteur pipette connected to a mechanical pump (aspirator) was used to remove water from the Luggin capillaries and the lower mesh. Any water drop present in the DCE phase might interfere with the conductance of the electrochemical cell. The clean glass cell was secured on the 3-jaw chuck which was mounted on the tilting stage and kinematic mount.

The position of the water||DCE interface was adjusted by the position of the top edge of a 300 μm Mylar strip. Mylar was pinned to the inner glass wall of the cell supported by a thick Mylar. Before putting inside, Mylar was rinsed with methanol, acetone and methanol, then with water. After that, It was soaked in DCE and wiped with alpha wipe. The Mylar was carefully placed in the sample cell. To do so, thick Mylar was placed on top of a thin Mylar. The 300 μm thick Mylar (1.5 cm in width) was wider than the thicker Mylar(1 cm). It was then

folded into a circle using a clean tweezer. The top edge of the Mylar was aligned properly with a height gauge at a height approximately midway between the tips of two Luggin capillaries.

A 0.1 M aqueous phase solution was prepared by dissolving 2.12 g of purified LiCl in 500 ml ultra pure water. LiCl is the aqueous phase electrolyte. Two to three drops of DCE were added to the aqueous solution and the solution was shaken vigorously. It was then left for several hours. DCE was added to the solution to make the aqueous phase in equilibrium with the organic phase to avoid any transfer once they came in contact in the sample cell. The solution was filtered through 0.2 μm filter membrane in a glass millipore filter.

Organic phase solution was prepared with tetraoctylammonium tetrachloroaurate (TOAAuCl_4) as the metal precursor, recrystallized tri-(p-tolyl)amine as the reducing agent, (BTPPATPFB) as organic phase electrolyte and 1,2-dichloroethane as organic solvent. The amount of each were measured to make the concentration 0.2 mM TOAAuCl_4 , 4 mM TTA and 15 mM BTPPATPFB in DCE. Few water drops were added to the solution to equilibrate the DCE solution with the aqueous solution. This solution was filtered with the glass millipore filter using 0.2 μm membrane. Water was carefully removed from the top of the surface with an aspirator.

A 25 ml clean glass pipette was used to pour organic solution into the cell. The liquid was added against the inner wall of the cell slowly and carefully to avoid any bubble formation and splashing. As the organic solution reaches the height of the tip of lower Luggin capillary, few drops of the organic solution was added through the outer tube of the capillary to remove any undesired water in the capillary. Residual water was pushed out of the capillary by placing

a rubber bulb on the opening of the outer tube of the capillary. The surface of the organic solution was aspirated during each filling to remove dust and water.

Aqueous solution was added to the cell by another clean 25 ml pipette. It was added very slowly against the inner wall of the cell. Due to hydrophilic glass, the water solution filled up from periphery towards the center. The weight of the added water might push down the level of organic solution. The level was constantly monitored so that water could not flow into the lower Luggin capillary. In case that might occur, rubber bulb, placed on the tip of outer tube, was used to blow out the water solution. The microsyringe connected to the cell through the lower capillary was filled with DCE solution and was used to add DCE solution. During the process of adding aqueous solution, little amount of DCE could come to the water vapor interface and evaporates, leaving BTPPATPFB as precipitate at the interface. Top surface of water was aspirated after addition of each 25 ml to keep it clean. If it was not clean, the precipitate might fall through the aqueous phase and land on the L/L interface. This would interfere with x-ray scattering measurements. The water solution was added until the top platinum mesh was fully immersed and the solution entered the top Luggin capillary used for aqueous reference electrode.

After adding both solutions, sample cell was covered with the glass top. Homemade Ag/AgCl electrode was directly immersed in the aqueous solution through the top reference electrode capillary. For the DCE phase reference electrode, an aqueous solution of 0.1 mM LiCl and 1 mM BTPPCl was added to the lower reference electrode capillary. The solution created a liquid junction for the organic phase reference electrode. Ag/AgCl electrode was immersed in

this solution. The reference electrodes and counter electrodes were connected to the Solartron potentiostat through four insulated wires. The outlets of the Luggin capillaries were covered with Teflon tape except for the capillary used for releasing pressure.

3.9 Ag/AgCl electrode preparation

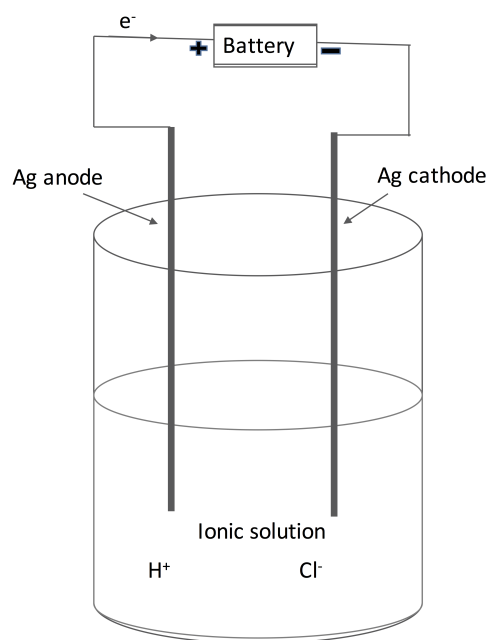


Figure 15: Reference electrode preparation

Ag wire was abraded with very fine sandpaper. It was rinsed with ultrapure water. The desired portion to be coated was immersed in a 0.1 M HCl solution as shown in [Figure 15](#). Using this electrode as anode, and another Ag wire as cathode, 10 mA/cm^2 current was allowed to

pass through the circuit for 30 seconds. Dark gray deposition formed on the Ag anode. it was rinsed with ultra pure water and was ready to use.

3.10 Electrochemical measurements

All the electrochemical measurements were performed using Solartron 1287 potentiostat (Solartron Instruments, England).

The potential difference of the electrochemical cell, measured by the potentiostat is $\Delta\phi_{cell}$. The absolute potential difference between the bulk aqueous phase and bulk organic phase is $\Delta\phi = \phi^{aqueous} - \phi^{organic}$. According to the definition of IUPAC, $\Delta\phi = \Delta\phi_{cell} - \Delta\phi_{pzc}$, where $\Delta\phi_{pzc}$ is the zero charge potential. Zero charge potential was determined from the electrocapillary curve of supporting electrolytes.

Cyclic Voltammetry (CV) is a technique where the applied electric potential across the interface is varied linearly between two limits, the initial electrode potential E_i and the final E_f . The current between the working electrode and counter electrode is measured while the applied potential is ramped at a constant rate. This rate is known as CV scan rate. For the CV measurements, the applied potential was varied between 100 mV and 600 mV at a scan rate of 5 mV/s, 10 mV/s and 15 mV/s. [Figure 16](#) shows detailed parameter settings for the CV measurements.

3.11 TEM measurements

JEOL JEM-3010 TEM was used at Research Resources Center (RRC) facility of University of Illinois at Chicago (UIC). It is a 300 kV TEM with a LaB6 electron source. It can achieve

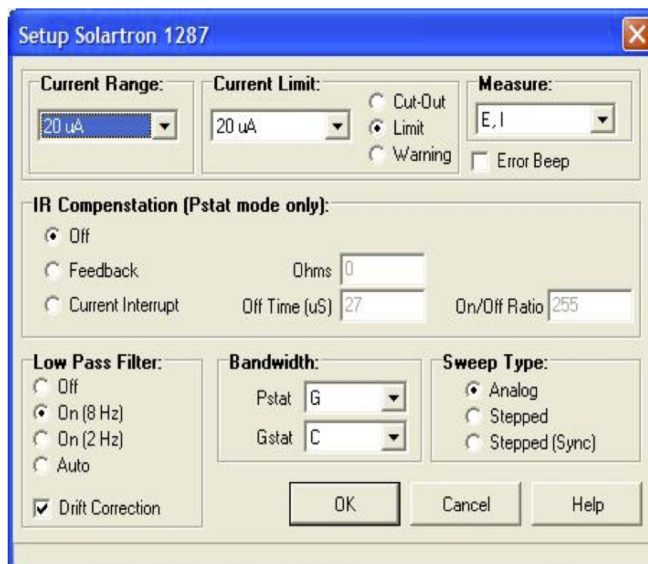


Figure 16: Parameters for CV measurements

0.14 nm resolution and 1500000x magnification. The microscope is equipped with an XEDS system.

Gold nanoparticles were formed at the water-DCE interface by applying potential across the interface. The dimensions of the formed particles were measured by TEM. For sample preparation, 2 μL solution was very carefully withdrawn from the water-DCE interface with a 10 μL syringe and was deposited on a 300 mesh holey copper-carbon grid (purchased from Tedpillars). The grid was dried under a UV lamp for 15 minutes. It was mounted on the TEM specimen holder. The holder was then carefully loaded in the ultra high vacuum TEM chamber. The holder was manipulated to bring the region of interest in the path of electron beam. The aperture of condenser lenses, objective lenses and projector lenses were adjusted to get a clear

image of the region of interest. The magnified images were collected by a Gatan Orius SC200 CCD 2000×2000 pixels.

3.12 X-ray scattering measurements

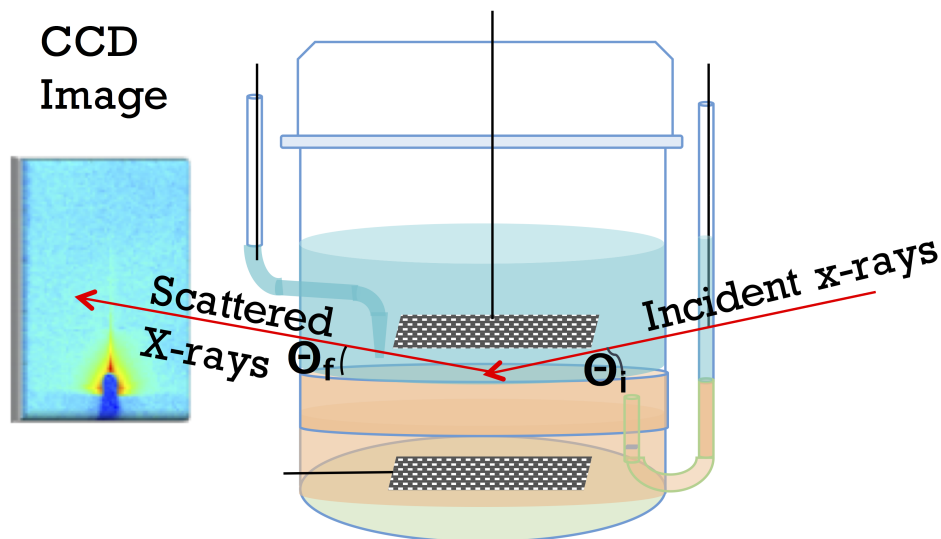


Figure 17: X-ray scattering measurements

The liquid spectrometer at the ChemMatCars Beamline 15-ID at Advanced Photon Synchrotron at Argonne National Laboratory, USA was used to perform the X-ray measurements. [Figure 18](#) is a schematic figure of the liquid surface spectrometer. Monochromatic X-rays of 30 keV energy were deflected by a steering crystal made of Ge(111) to the sample surface at a desired incidence angle. An ionization chamber measured the intensity of the incident beam.

A set of slits (S_1) determined the height and width of the incident beam. A 2 mm wide and 0.015 mm high X-ray beam was used for our GISAXS experiments. The intensity of the incidence beam was optimized by a set of absorbers placed between the sample and the ionization chamber to avoid CCD detector saturation and sample damage.

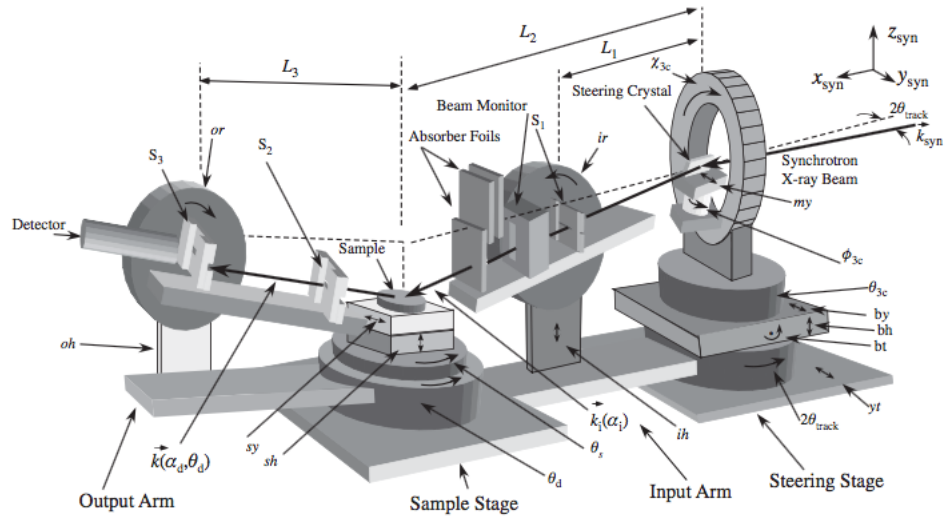


Figure 18: Schematic figure of liquid-surface spectrometer installed on the ChemMatCARS at Advanced Photon source, ANL. Copied from Liquid Surfaces and Interfaces: Synchrotron X-ray Methods (p. 31) by P. S. Pershan, M. Schlossman, 2012, Cambridge University Press.

Scattered x-rays were recorded with a Bruker Apex II CCD area detector with 1024×1024 pixels. The detector resolution was achieved by grouping a 4×4 set of pixels into one virtual pixel. Each virtual square pixel is 60 mm on a side. The important parameters of the

spectrometers are, the distance between the steering crystal and the first sets of slits, S1 (563 mm), the distance from the steering crystal to the center of sample (1242 mm), the distance from the center of the sample cell to the CCD camera (3275 mm). The flatness of the interface was measured with a sample height scan with the X-rays. An acceptable flatness of the interface for our experiment usually had a full width at half maximum (FWHM) of $\sim 100 \mu\text{m}$ from the sample height scan at $Q_z = 0.06 \text{ \AA}^{-1}$.

For GISAXS measurements, the x-rays struck the surface at an incident angle (less than the critical angle of water-DCE interface) for total external reflection. A beam stop was placed before the detector to block the direct and totally reflected beams for GISAXS measurements. The slits before the CCD detector were wide open (width 58 mm, height 61mm) to record the diffused scattering. Bulk scattering from aqueous phase was measured by lowering the sample by 1 mm. Interface flatness was checked every half an hour.

For x-ray reflectivity measurements, the incidence angle was varied and the specularly reflected beam was recorded with the CCD detector. The reflectivity was calculated by summing over a region of 30×60 (v \times h) virtual pixels.

3.13 Interfacial tension measurement

The interfacial tension of water-DCE interface was measured by using Quasi Elastic Light Scattering (QELS) technique. A monochromatic coherent laser light was allowed to scatter from the interface in transmission mode. The scattered light was further scattered from a grating of known grating constant, which gives a diffraction pattern. The Fourier transform of the intensity of different order diffraction peaks was recorded using a Fourier Transform Analyzer.

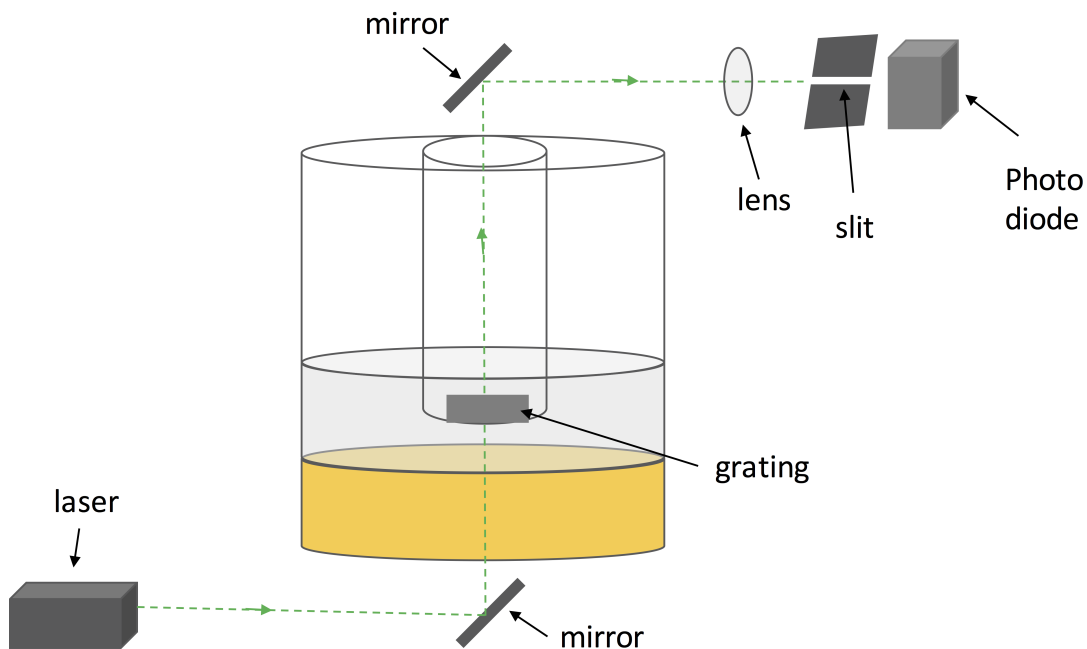


Figure 19: Interfacial tension measurements

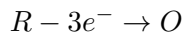
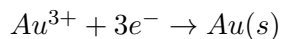
For the experiment, a 20 mW green Nd:YAG laser (purchased from Crystal Laser Corp.) with a wavelength of 532 nm was used. A 45° mirror was placed on the mounting stage of the sample cell to make the incidence angle of 90° on water-DCE interface. The transmitted beam through the liquid was scattered from a grating with grating constant $250\ \mu\text{m}$. The beam was then reflected by another 45° mirror and focused on to a S1133 Hamamatsu photodiode by a convex lens. The setup is shown in [Figure 19](#). The signal was amplified by a wide band amplifier (model 13AMP005 Melles-Griot). Fast Fourier Transformation (FFT) of the amplified signal was performed by Stanford Research model SRS760.

CHAPTER 4

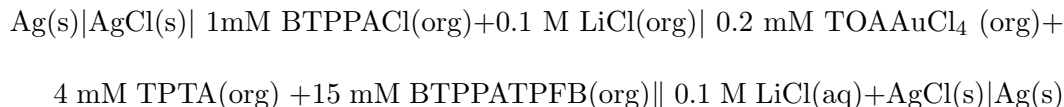
GISAXS AT WATER/DCE INTERFACE

4.1 Gold Nanoparticle Synthesis

In situ GISAXS technique was used to probe the formation of AuNPs at the electrified water-DCE interface. AuNPs were formed by a simple redox reaction,



where, R is the reducing agent and O is the oxidized products. The electrochemical L/L cell investigated by GISAXS was,



One important thing to notice, even though the anionic complex $AuCl_4^{-}$ and the reducing agent, TPTA both were dissolved in the same organic solvent 1,2-DCE, the reduction process did not occur. But upon transferring the $AuCl_4^{-}$ to the aqueous phase, it was reduced spontaneously by TPTA and formed Au particles at the interface. This is because the standard reduction potential of $AuCl_4^{-}$ to Au(0) in aqueous phase is 1.002 V, where in organic phase the value is $-0.9 V$ [9, 10].

The distribution of $AuCl_4^{-}$ at the interface was controlled by applying potential across the interface. The Cyclic Voltammogram (CV) measurements on the sample cell were performed

to investigate $AuCl_4^-$ transfer from organic to aqueous phase. Figure 20 shows the CV of the electrochemical cell.

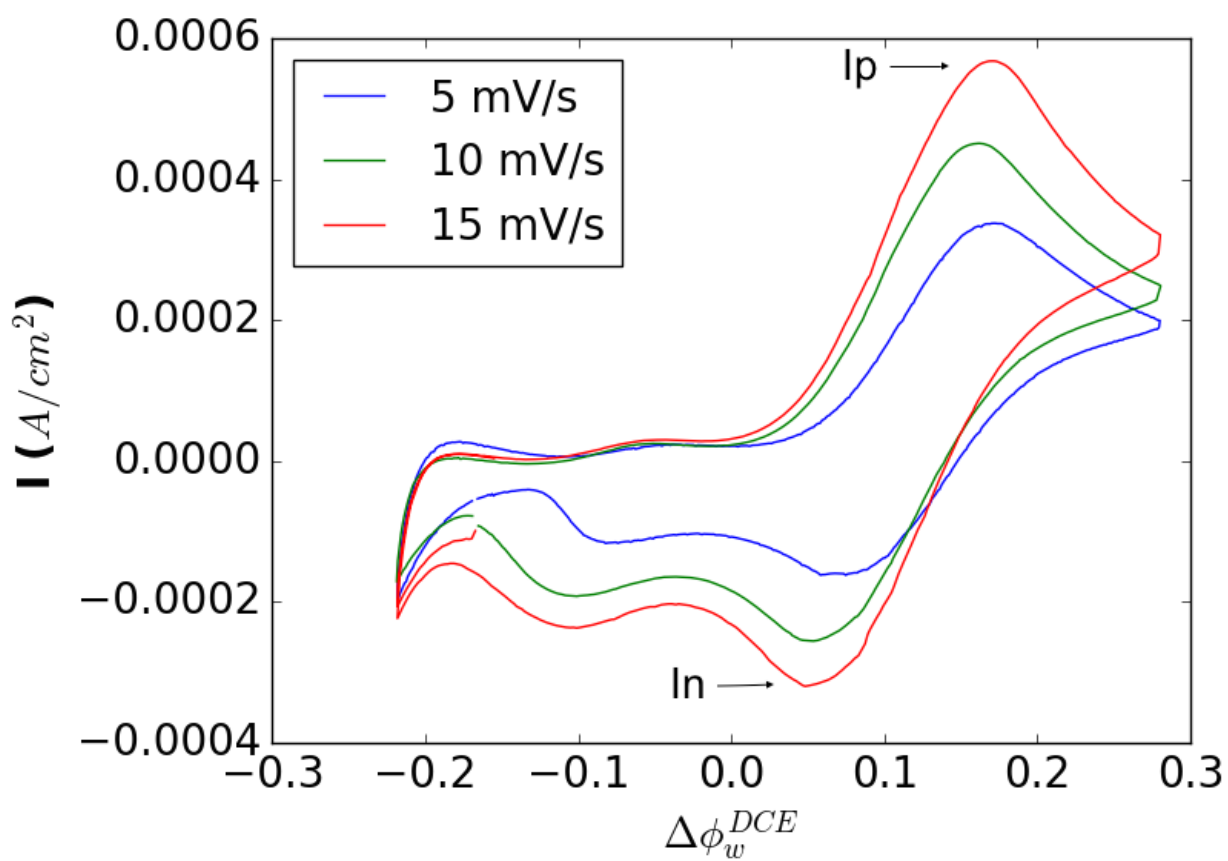


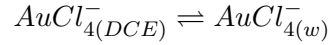
Figure 20: Voltammograms for the $AuCl_4^-$ ion transfer across the water-DCE interface as a function of scan rate

The CVs were performed at scan rates 5 mV/s, 10 mV/s and 15 mV/s. The measured potential, E is converted to the Galvani cell potential, ϕ^{DCE} as,

$$\phi_w^{DCE} = E - E_{PZC} \quad (4.1)$$

where, the potential of zero charge, $E_{PZC} = 320$ mV. The evaluation of E_{PZC} is described in ??

The positive and negative peak current, I_p and I_n as shown in [Figure 20](#), are due to the transfer of $AuCl_4^-$ between Water and DCE.



The CV also shows that the peak in the current varies linearly with the square root of the scan rate indicating the ion transfer process is diffusion controlled.

AuNPs were formed at the interface by transferring $AuCl_4^-$ at a positive potential E_{trans} for t_{app} minutes. The electrochemical cell was then held at a slightly negative potential E_{hold} , so that the transferred $AuCl_4^-$ did not diffuse into the bulk.

During the GISAXS experiments at Advanced Photon Source, the electrodeposition conditions were varied to probe the growth of AuNPs in situ at the water/DCE interface. Experimental conditions are summarized in [Table I](#).

Batch No.	E_{trans} (mV)	t_{app} (seconds)	E_{hold} (mV)
1	130	15	-220
2	130	15	-120
3	130	15	-260
4	130	15	-20
5	130	3	-20

TABLE I: Electrochemical deposition by changing applied potential and duration time.

Time resolved GISAXS patterns were obtained for Batch 5 and are analyzed in this chapter. Ex situ transmission electron microscopy (TEM) confirmed the formation of AuNPs at the interface which is discussed later in this chapter.

4.2 Determination of Potential of Zero Charge

The potential of zero charge, E_{ZPC} at a surface is defined as the potential when the electrical charge density on the surface is zero. The excess charge per unit area of an interface, σ according to Lippman's equation [22, 13] is:

$$\sigma = -\frac{\delta\gamma}{\delta E} \quad (4.2)$$

where, γ is the interfacial tension and E is the potential.

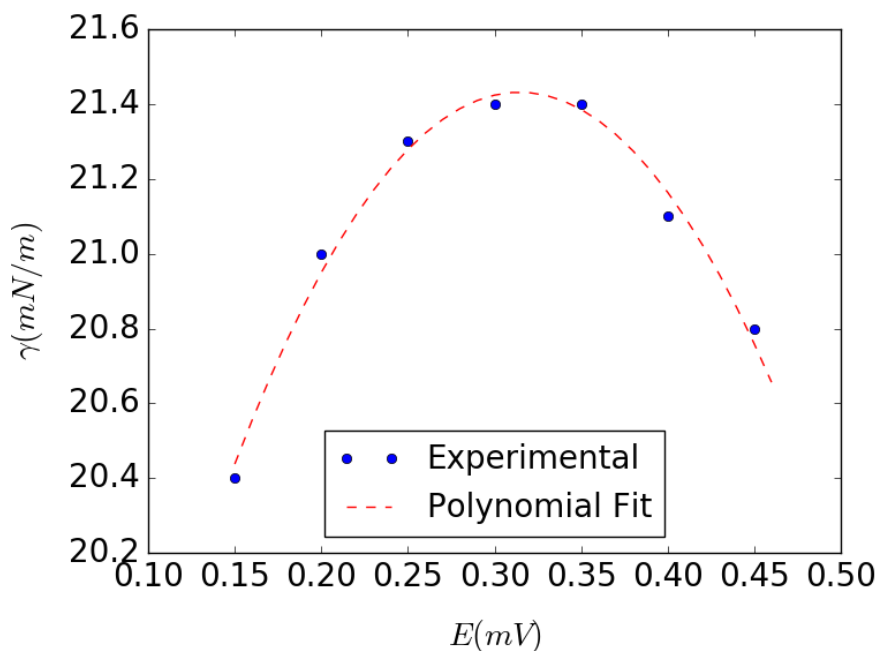


Figure 21: Interfacial tension measurements at the interface between 0.1 M LiCl in water and 15 mM BTPPATPFB in DCE.

The E_{ZPC} can be obtained from the Interfacial tension, γ vs. applied potential, E curve as shown in Figure 21. The interfacial tension was measured at the interface between 0.1 M LiCl in water and 15 mM BTPPATPFB in DCE using QELS. The curve was fitted by a polynomial function. The $E_{ZPC} = 320 \text{ mV}$ was determined from the apex of the fitted curve.

4.3 GISAXS Measurement

As mentioned above, The growth of AuNPs were followed in situ by synchrotron GISAXS technique. Figure 22 illustrates the scattering geometry of GISAXS. The incident X-rays strike

the surface at an incident angle α_i at a very small angle, typically less than the critical angle, α_c of the surface and exits at an angle α_d with the scattering plane. The angle θ_d is the in plane angle of the scattered wave vector. The incident and scattered wave vectors are denoted by \mathbf{k}_i and \mathbf{k}_s respectively. Therefore, the wave vector transfer \mathbf{Q} is,

$$\mathbf{Q} = \mathbf{k}_s - \mathbf{k}_i \quad (4.3)$$

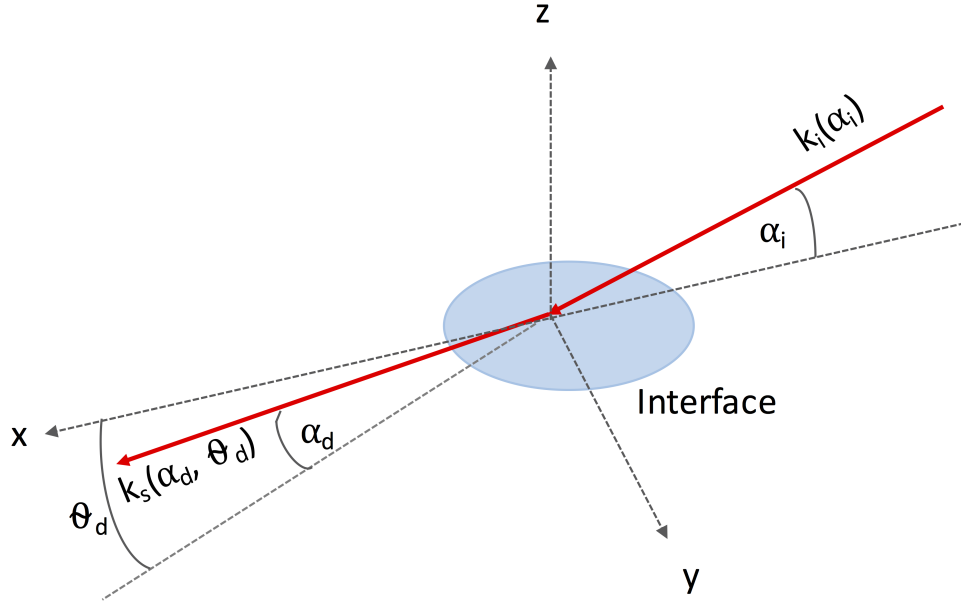


Figure 22: Scattering geometry of grazing incidence small angle X-ray scattering.

The parallel (\mathbf{Q}_{xy}) and the perpendicular (\mathbf{Q}_z) components of \mathbf{Q} can be expressed as functions of α_i , α_d and θ_d ,

$$Q_{xy} = \sqrt{Q_x^2 + Q_y^2} = k_0 \sqrt{\cos^2 \alpha_d + \cos^2 \alpha_i - 2 \cos \alpha_i \cos \alpha_d \cos \theta_d} \quad (4.4)$$

$$Q_z = k_0 (\sin \alpha_i + \sin \alpha_d) \quad (4.5)$$

Specularly reflected wave vector transfer \mathbf{Q}_z is,

$$\mathbf{Q}_z = 2k_0 \sin \alpha_i \hat{\mathbf{z}} \quad (4.6)$$

X-ray scattering measurements require a very flat interface. A sample height scan of the interface is used to test the flatness of the interface. An experimental sample height scan at $Q_z = 0.06 \text{ \AA}^{-1}$ is shown in [Figure 23](#). The full width at half maximum (FWHM) of the scan was $95.6 \text{ } \mu\text{m}$. At this angle this FWHM was due to $\frac{95.6}{\tan(0.0019)} \approx 50 \text{ mm}$ of interface flatness. Our sample cell diameter was $\approx 70 \text{ mm}$. This level of flatness was acceptable for GISAXS measurements.

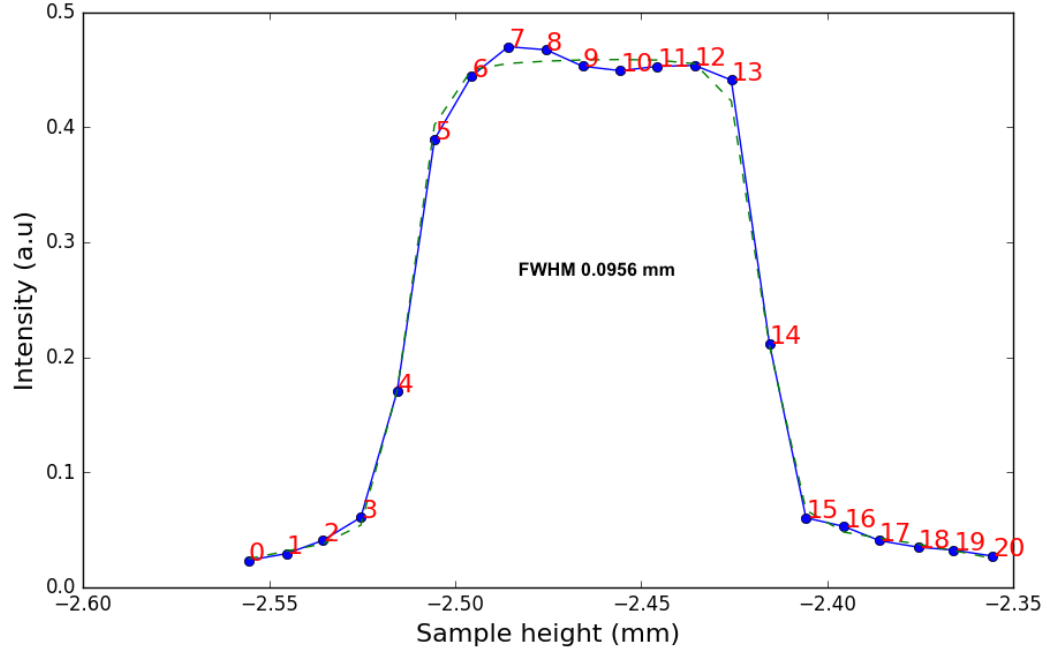


Figure 23: Sample Height Scan

4.3.1 Two Dimensional GISAXS Patterns

The distribution of the scattered X-rays was recorded in the plane of detection by a Bruker APEXII CCD detector with 1024×1024 pixels. This results in a two-dimensional scattering pattern, $I_{exp}(y, z)$, where y and z are the horizontal and vertical pixel numbers. Figure 24 is a typical 2D GISAXS pattern.

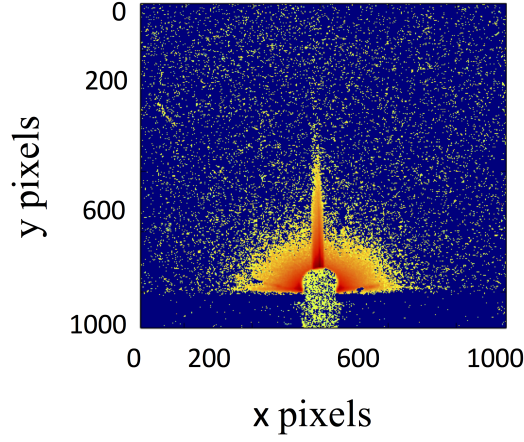


Figure 24: 2D GISAXS image

4.3.2 1D Linecuts

Most of the time, recorded 2D GISAXS patterns have more data than are actually necessary. Particle size, shape, orientation, inter-particle distances can be described by 1 dimensional (1D) scattering curves. I vs Q linecuts can be obtained by integrating intensity over a selected region either in Q_{xy} or Q_z direction which is then fitted with appropriate model to get quantitative informations about the particles. For the data analysis purpose, the narrow region to integrate over was carefully chosen. 1D linecuts were obtained by integrating over a narrow zone Q_{xy} , 0.016 to 0.018 \AA^{-1} (bounded region by two white lines in Figure 25 (a)).

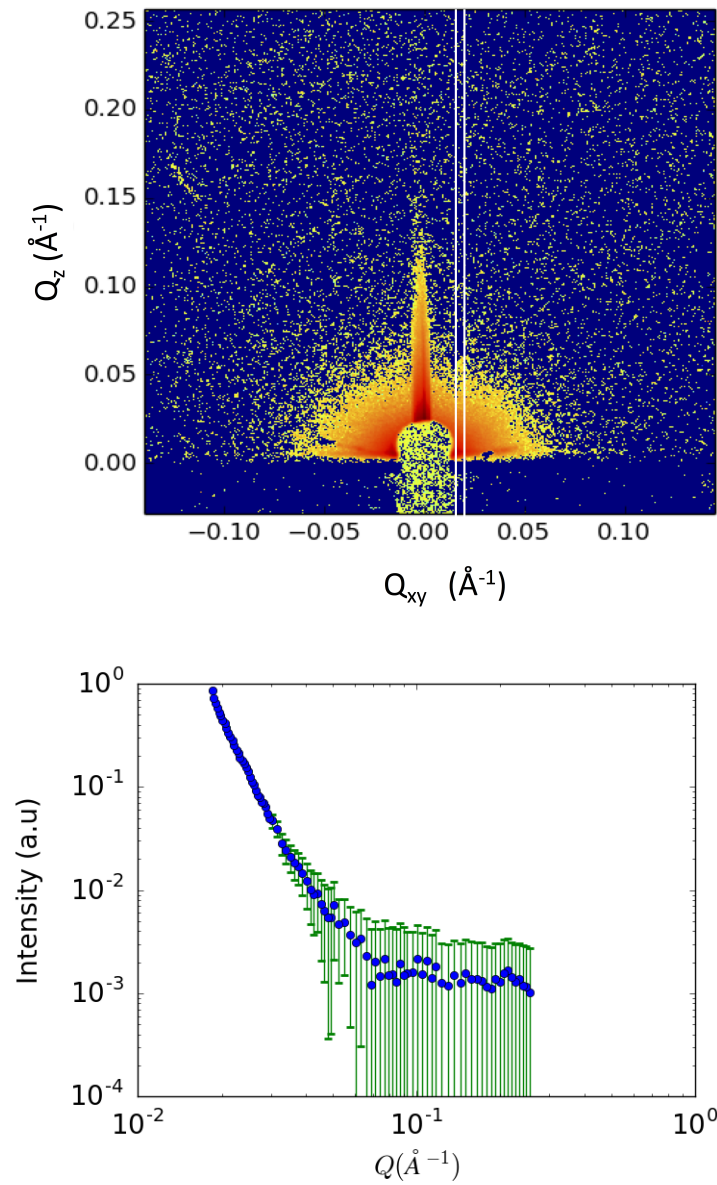


Figure 25: (a) 2D GISAXS image converted to Q space. (b) I vs Q curve integrated over the narrow white bounded region

Figure 25 (b) shows the I vs. Q curve after integration over the narrow zone.

4.3.3 Exposure time

As we are probing time resolved particle growth, shorter exposure time provides better experimental resolution but the statistical quality of the scattering pattern improves with increasing intensity, hence longer exposure time provides good quality data. For our experiments, each frame was recorded for 60 seconds exposure. Typically 10 frames were averaged to improve data quality. Repeated short exposure was preferred over long exposure to avoid saturation value of the CCD detector.

4.3.4 Primary Data Processing

Before the 1D linecuts are extracted for data analysis, each CCD image is processed to take into account dark count of the detector and any changes in the incident X-rays. The error propagation is also calculated with each mathematical operation. Dark count is the intensity that the detector records even though no X-ray beam is switched on. The dark count for our detector was $32 \frac{\text{counts}}{\text{pixel}}$ and it was subtracted from each pixel of the

The error in the CCD data is calculated by the following equation which is provided by the Beamline 15ID at APS, ANL.

$$\text{error} = \sqrt{a \times CCD\text{imagedata} \left(1 + b + \frac{\text{data}}{ab}\right)}$$

where, a=0.1, b=200.0

After dark count subtraction the scattered intensity is normalized by the intensity of the incident beam I_0 .

The error after normalization is calculated as,

$$normalized\ imagedata = \frac{imagedata \times absorberfactor^{absorbernumber}}{I_0}$$

$$error\ after\ normalization = \sqrt{\left(\frac{imagedata^2}{I_0^2} + \frac{imagedata^2}{I_0^3}\right) \times absorberfactor^{2 \times absorbernumber}}$$

Then, the scattering image, $I_{exp}(x\ \text{pixels}, y\ \text{pixels})$ is converted from real to reciprocal space $I_{exp}(Q_{xy}, Q_z)$. Mapping of the pixels to Q space was performed with the known values of wavelength of incident X-rays, sample to detector distance, position of the direct beam and the size of a pixel of the CCD detector.

4.3.5 Evolution of GISAXS Patterns with Time

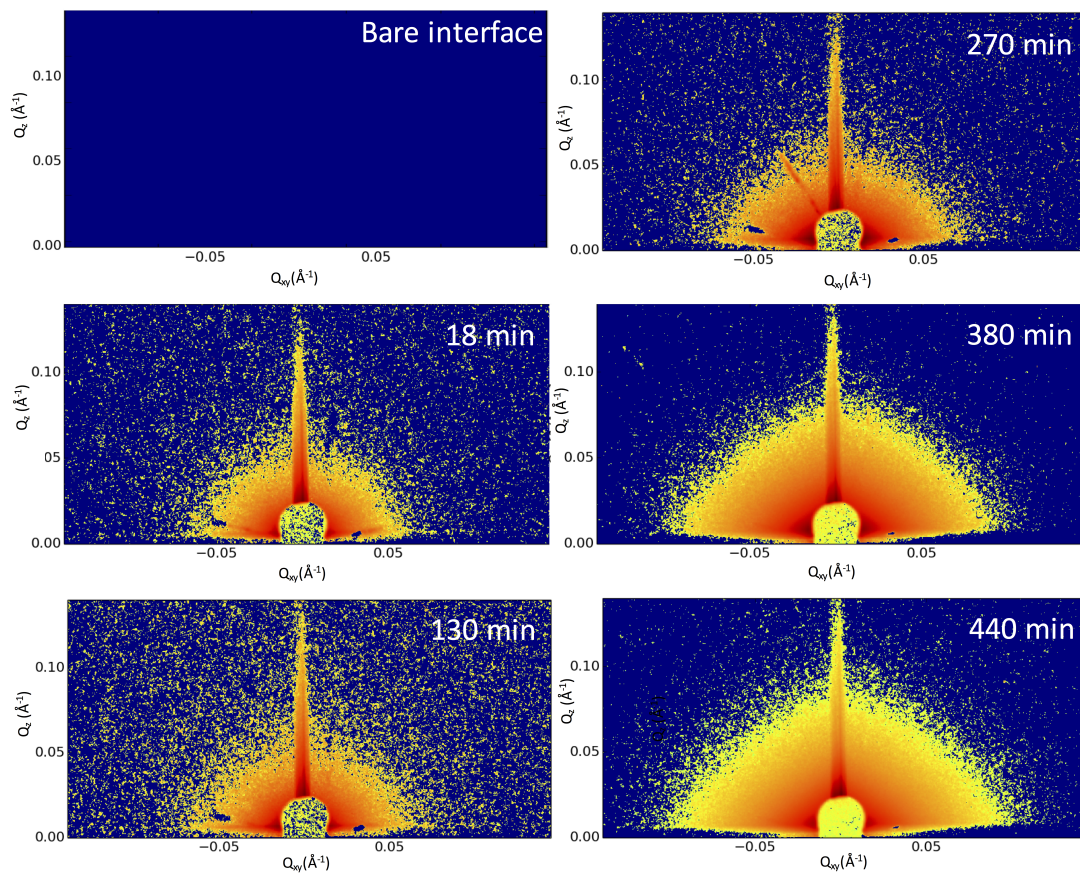


Figure 26: background subtracted GISAXS patterns with time

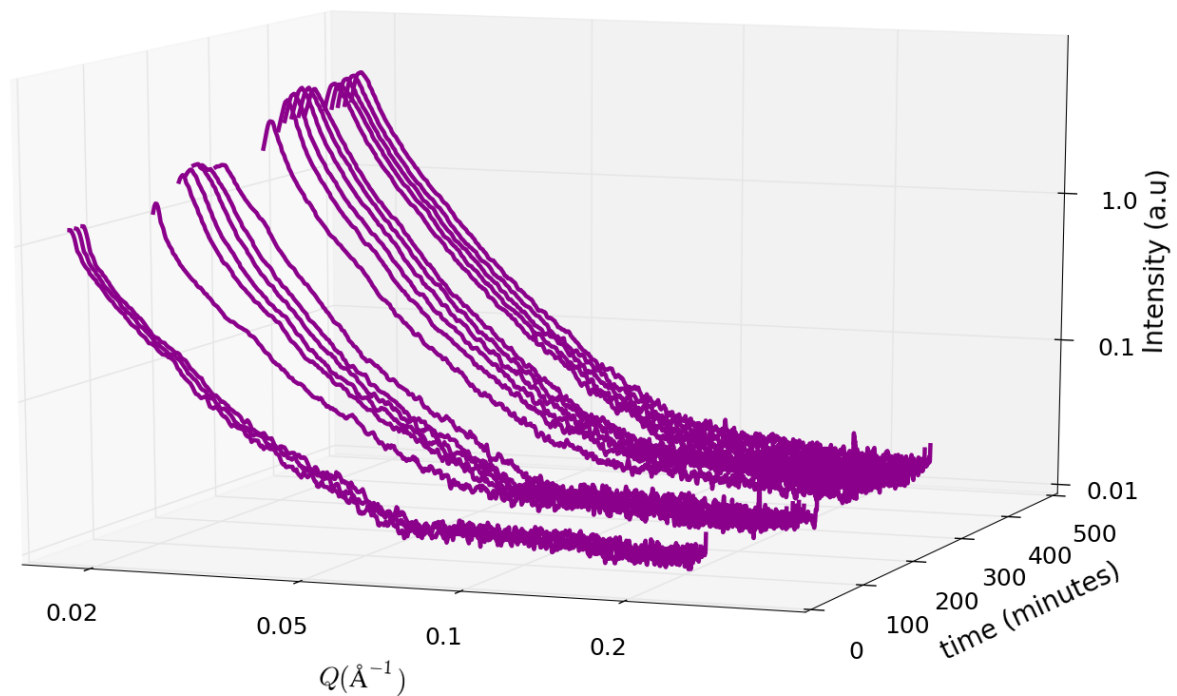


Figure 27: I vs Q curves with time

[Figure 26](#) compares the GISAXS images with time. All the images are background subtracted. From the figure, it is clearly evident that 2D GISAXS images are changing with time which indicates that the structure at the interface is changing. To have better understanding of the temporal growth of the particles, the linecuts are compared in [Figure 27](#). The I vs Q curves in the figure show how the scattering pattern from the interface are changing with time.

The change in the slope of the curves can be associated with the change in size and number of the particles at the interface.

4.4 Background Subtraction

It is critical to measure proper background for background subtraction. During the experiment, Background was measured by two different methods. One was, GISAXS from bare interface and the other one was recording transmission X-rays through the aqueous (top) phase. Both were performed with the same GISAXS geometry. Linecuts from these two backgrounds are compared in [Figure 28](#). It shows I vs Q_{xy} (integrated over Q_z range of 0.016 to 0.018 \AA^{-1}) and I vs Q_z line cuts (integrated over Q_{xy} range of 0.016 to 0.018 \AA^{-1}) for both backgrounds where green curve represents scattering from bare interface and the blue curve is for transmission X-rays. It indicates the backgrounds are similar except for the appearance of a sharp Yoneda peak in out of plane direction in case of scattering from interface. Yoneda peak is a characteristic feature of a GISAXS pattern. The Yoneda peak occurs when the exit angle is equal to the critical angle of the interface. Theoretically, the Yoneda peak for water, DCE interface with 30 keV X-rays is at Q_z value 0.008 \AA^{-1} , and experimentally the peak is observed around 0.007 \AA^{-1} . As the two backgrounds are similar and the region around Yoneda peak was carefully avoided during data modeling and fitting, either background could be used for subtraction. In this thesis, the scattering from bare interface was subtracted for analyzing the structure of nanoparticles forming at the interface with time.

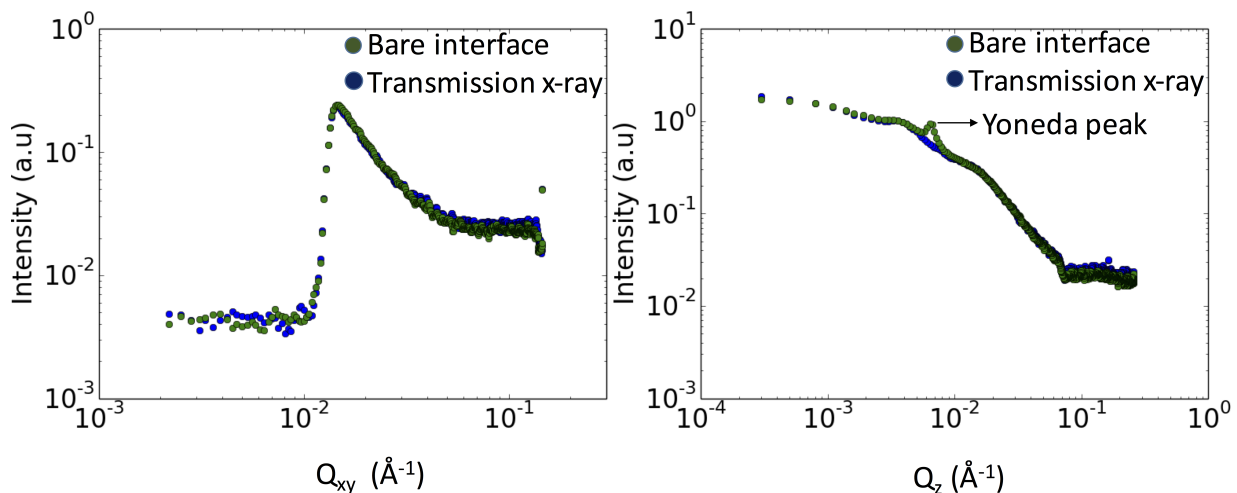


Figure 28: X-ray transmission through the sample and scattering from bare interface linecuts are compared in both direction. The I vs Q_{xy} curve is integrated over Q_z from 0.016 to 0.018 \AA^{-1} and same Q_{xy} is integrated for I vs Q_z curve.

Figure 29 shows the background subtracted GISAXS images. Left image is the GISAXS pattern before the reaction started ($t = 0$) and right image is the average GISAXS pattern from $t = 0$ to $t = 10$ minutes. As seen, they are significantly different, which indicates formation of particles at the interface. The most pronounced feature in the right image is the presence of almost spherical half ring, the center of which is hidden by the beam stop. The half spherical ring generally indicates the present of spherical particles.

Figure 29.

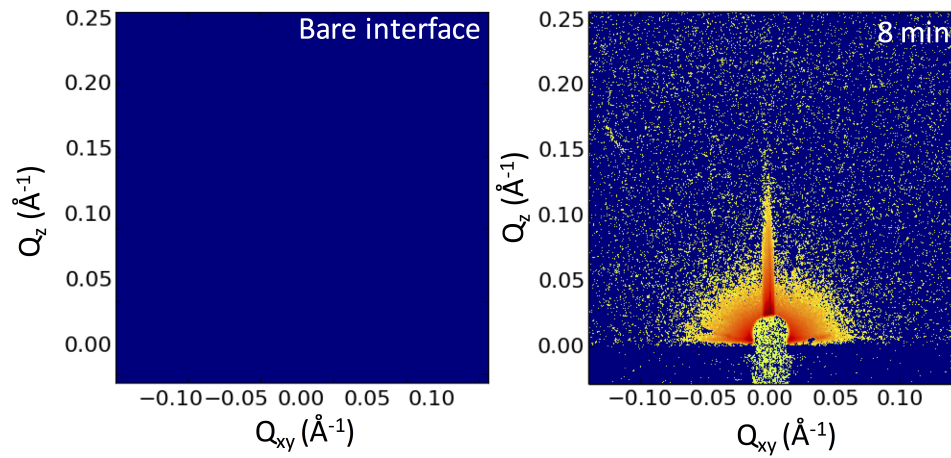


Figure 29: background subtracted GISAXS pattern at (a)bare interface (b)at $t = 0$ to 10 minutes

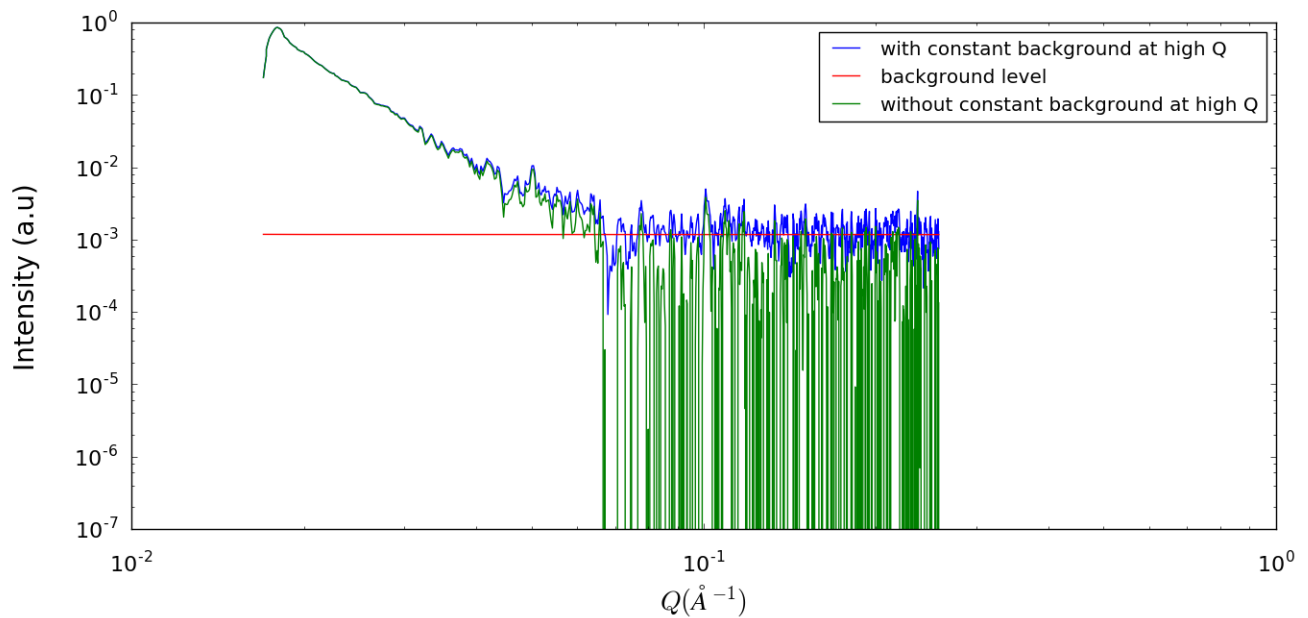


Figure 30: The constant background at high Q (blue curve) is fitted (red curve) and subtracted (green curve).

Figure 30 shows the background subtracted I vs Q curve integrated over Q_{xy} region 0.016 to 0.018 \AA^{-1} averaged over $t = 0$ to 10 minutes. One thing to notice, the curve levels off at high Q values which is possibly for due to incoherent scattering (compton scattering or fluorescence)

I_{inc} , that adds a constant to the scattering curve. Once this constant is fitted and subtracted, then the scattering curve falls down to the noise level at high Q.

4.5 Data Interpretation

4.5.0.1 Shape of the Particle

The shape of the AuNPs were investigated by transmission electron microscopy (TEM). [Figure 31](#) is a TEM image of the particles obtained by applying 130 mV for 1 minute. Though any in-situ information on the growing particles was not obtained from the TEM image but the image suggested the average shape of the particles was spherical.

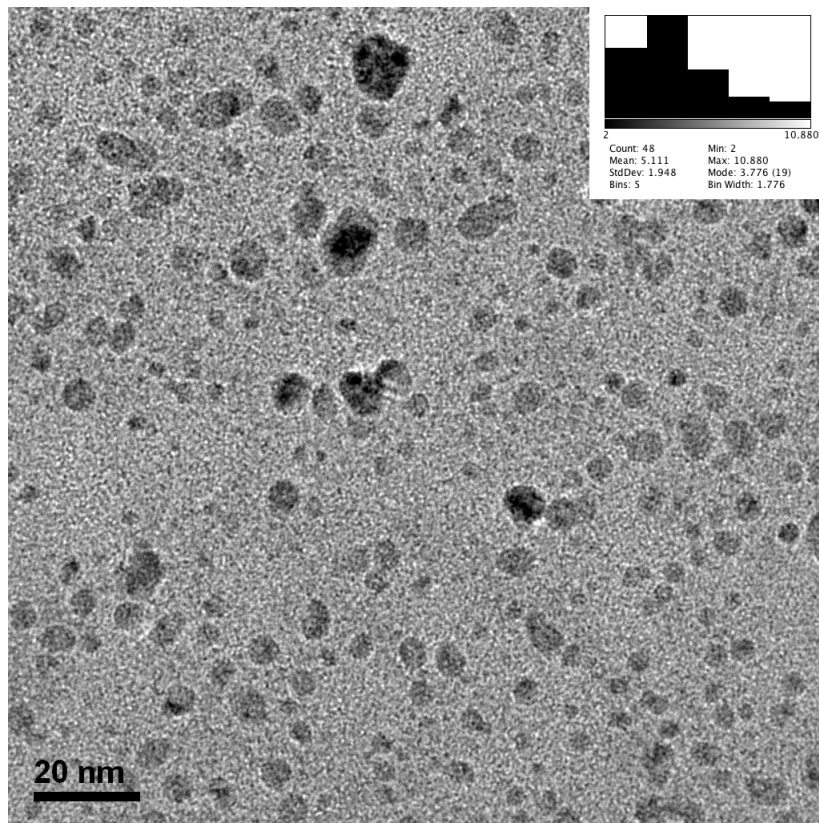


Figure 31: TEM image of gold nanoparticles forming at liquid/liquid interface at 300k magnification. Particles were formed by applying 450 mV at the interface for 1 minute and then collected immediately

The shape of the particles can be also deduced from the asymptotic behavior of the form factor. This is known as the Porod approach. At large Q values where $Q_{xy}R > 3.5$ or $Q_zR > 3.5$ condition is valid, the intensity ($I(Q_{xy})$ or $I(Q_z)$) of the 1-D linecuts varies with Q_{xy} or Q_z with an exponent n which depends on the shape of the formed particles. For instance, $n = 4$

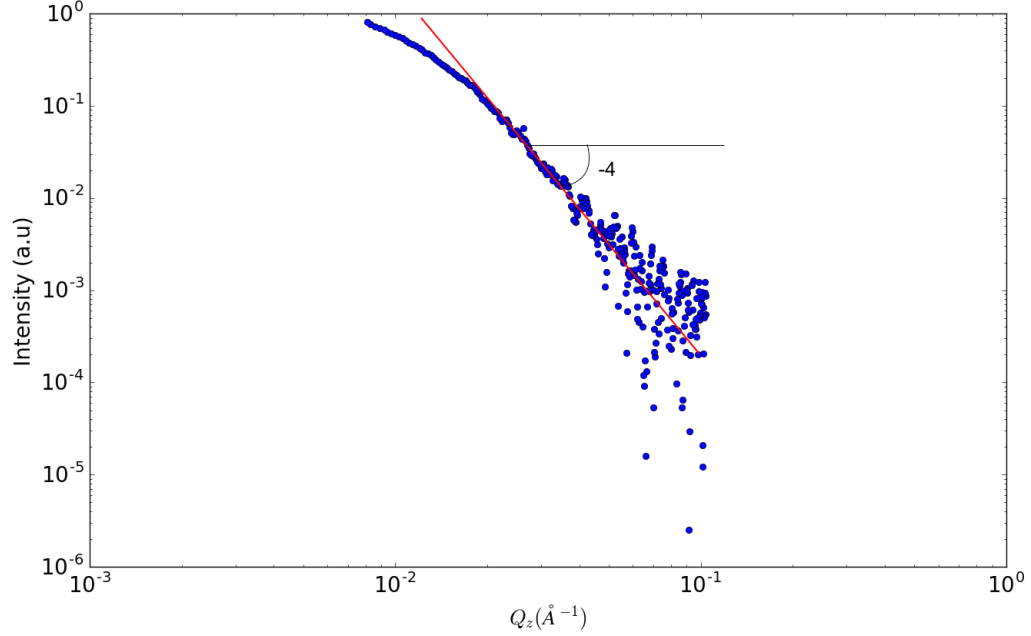


Figure 32: log-log plot of the I vs Q_z with a power law fitting at high Q_{xy} range

in both direction for spherical particles, for cylindrical particle $n = 3$ in parallel direction and $n = 2.5$ in perpendicular direction, For pyramid shaped particles, $n = 4$ in parallel and $n = 2.5$ in perpendicular direction [25].

Figure 32 and Figure 33 are the Porod plots of GISAXS pattern at 0-10 minutes. $I(Q_{xy}) \propto Q_{xy}^{-4}$ and $I(Q_z) \propto Q_z^{-4}$ at high Q ($Q_{xy}R$ and $Q_zR > 3.5$) range in the plots illustrate presence of spherical particles at the interface. One limitation of Porod plots is the plots are fitted at high Q which can coincide with the noise level of the experiment. In our experiment, the Porod plots support fitting the experimental data with spherical particles.

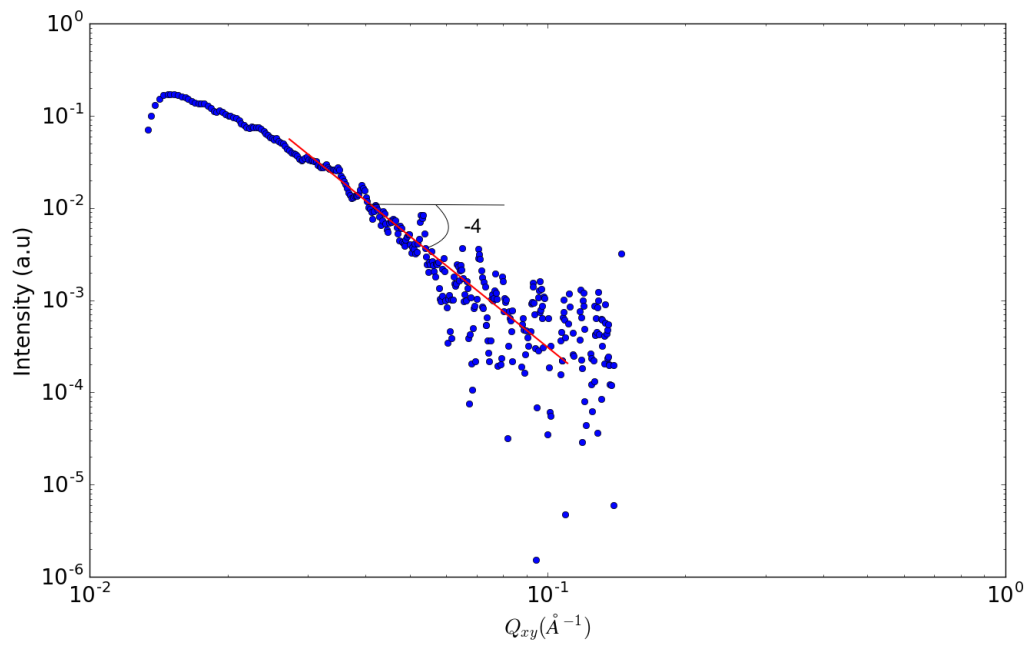


Figure 33: log-log plot of the I vs Q_{xy} with a power law fitting at high Q_{xy} range

4.5.1 Data Modeling

The 1-D I vs Q curves were obtained from the 2-D GISAXS patterns by integrating intensity from Q_{xy} 0.016 to 0.018 \AA^{-1} .

The intensity can be written as,

$$I(Q) = A. |F(Q)|^2. S_{||}(Q) \quad (4.7)$$

where A is a constant scale factor. All the constants are lumped into A which consists of the particle contrast, volume, concentration etc. $F(Q)$ is the average nanostructure form factor. Form factor is the Fourier transform (FT) of the shape of the nanostructure. $S_{||}(Q)$ is the structure factor which is defined as the FT of the pair correlation function of the nanostructure position.

Typically, the distorted-wave Born approximation (DWBA) is used to analyze diffuse scattering to take into consideration the dynamic effects at shallow angle near the critical angle. Form factor under DWBA is

$$\begin{aligned} F_{DWBA}(Q_{xy}k_{iz,w}, k_{iz,DCE}) = & F(Q_{xy}(k_{fz,w} - k_{iz,DCE}) + r_{w,DCE}^f F(Q_{xy}(-k_{fz,w} - k_{iz,w}) \\ & + r_{w,DCE}^i F(Q_{xy}(k_{fz,w} + k_{iz,DCE}) + r_{w,DCE}^f r_{w,DCE}^i F(Q_{xy}(-k_{fz,w} + k_{iz,w}) \quad (4.8) \end{aligned}$$

At high Q , the DWBA form factor simply reduces to the Born approximation as in the high Q range the Fresnel reflection coefficients $r_{w,DCE}^i, r_{w,DCE}^f$ go to zero. For the simplicity of the modeling of the 1-D linecuts the region near Yoneda peak was carefully avoided, that is the intensity at low Q values were not fitted. In general, $Q_z > 4Q_c$ rule [25] was followed to fit 1D linecuts. Below this range, it is difficult to fit with a simple model function.

Now, the relative positions of particles can be described by a reduced partial pair correlation function $g(r_{||})$. The structure factor $S(r_{||})$ is,

$$S(r_{||}) = 1 + n_s \int_A (g(r_{||}^{\vec{r}}) - 1) e^{Q_{||} \cdot r_{||}^{\vec{r}}} dr_{||}^{\vec{r}} \quad (4.9)$$

For a disorder system with lack of long range order, $g(r_{||}^{\vec{r}}) \rightarrow \infty \approx 1$. Hence, the $S(r_{||})$ can be approximated as 1. The GISAXS patterns in our experiment there is no visible Bragg peak which indicates lack of long range order. It can be concluded that $S(Q) = 1$ for our system. The GISAXS intensity is then entirely determined by the form factor.

So, the model function becomes,

$$f(Q) = A \cdot |F(Q)|^2 \quad (4.10)$$

The form factor in the equation 4.10 is the average of all illuminated particles in the sample. $F(Q)$ therefore is the sum of the contributions from identical particles in monodisperse samples, particles of the same general shape but different size, or particles of totally different shapes and sizes. For our sample, the average shape of the particle is reasonably predicted to be spherical. It

is known I vs. Q linecuts oscillate at certain Q values depending on the size for a monodispersed system. The presence of distribution in size smoothes the oscillations in the scattering curve. So, from the 1D linecuts for our sample, it is obvious the particles are polydispersed.

For a polydispersed system, the average form factor $F(Q)$ can be calculated from,

$$F_{average}(Q) = \int_0^\infty |F(Q, R)|^2 P(R) dr$$

Here, $P(R)$ is the intensity weighted size distribution.

The shape of the particles was identified to be spherical based on the TEM and Porod plots. Therefore, the experimental scattering data was fitted with theoretical model for spherical particles to determine the size of the particles. The Rayleigh function is the spherical form factor function which describes small-angle scattering from random dilute suspension of spheres. The bare function is,

$$F(Q, R) = \frac{3(\sin(QR) - QR\cos(QR))}{(QR)^3} \quad (4.11)$$

The exact size distribution law is very difficult to predict. The size distribution is usually described by a log-normal probability distribution. The distribution function is asymmetric and is expressed by the following equation:

$$P(R) = \frac{\exp\left\{\frac{-(\ln QR - \mu)^2}{2\sigma^2}\right\}}{QR\sigma\sqrt{2\pi}}$$

where μ and σ for the log normal distribution are defined as

$$\mu = \ln \left(\frac{R_{avg}}{\sqrt{1 + \frac{\nu_R}{R_{avg}^2}}} \right)$$

$$\sigma^2 = \ln \left(1 + \frac{\nu_R}{R_{avg}^2} \right)$$

where R_{avg} is the average radius of the the particles and ν is the variance of the sample.

As shown earlier, after primary data processing and the background subtraction 1D linecuts still have a constant background at high Q. So, with the model function above a constant was also added as background.

$$f(Q) = AF_{average}(Q) + background \quad (4.12)$$

Now, the model function has 3 parameters, A, R_{mean} , σ_R . Background for each dataset was obtained by fitting the flat region separately as described in Section 4.4.

The fitting program reads the experimental data, calculates the model function with the starting values of the parameters provided by the user. Then it compares the calculated and experimental data. The best values of the parameters are found which provide the best agreement between the model and the data. There are different algorithms for accomplishing the best fit. Least-squares method was applied for our fitting program.

In the least-squares method, the agreement between experimental curve and the model function is described by χ^2 , which is defined as,

$$\chi^2 = \sum \left(\frac{f(Q_i) - I_{i,exp}}{e_i} \right)^2$$

so, the reduced χ^2_ν is defined as:

$$\chi^2_\nu = \frac{\chi^2}{N - M}$$

Here, N is the number of data points(I_i, Q_i) each with uncertainty e_i in I_i . At each point the model function $f(Q_i)$ is calculated which depends on the values of 4 parameters. The goal is therefore to find the set of parameters which minimizes χ^2 .

While fitting, the starting parameters were chosen carefully. In the least-squares method, the fitting function just finds the minima that is the closest to the starting parameters. So, the fitting function can find a local minima, which might not be the global minima. Thus the fitting program can provide data set which is not a good fit. To avoid false minima, it was ensured the data visually fitted. Also, different ranges of starting parameters were tried to verify if they find the same minima.

Our data was fitted with a commercial X-ray data analysis software Datasqueeze (<http://www.datasqueezesoftware.com/>)[12]. Datasqueeze software reads the 1D scattering curves and plots it. The plotted data can be least-squares fit to a wide variety of models suitable for powder diffraction analysis (Lorentzian, Gaussian, Voigt), scattering from spheres, rods, or disks, or polymers. The 1D scattering curves were also fitted with our own fitting function written in python programming language which is provided in [A](#).

[Figure 34](#) shows the fitted curve (red curve) for spherical particles plotted with the experimental data (blue dots). The best fitted values found by the fitting program are, $R = 204 \text{ \AA}$, standard deviation in R, $\sigma_R = 49 \text{ \AA}$ and the constant, $A = 3.44$.

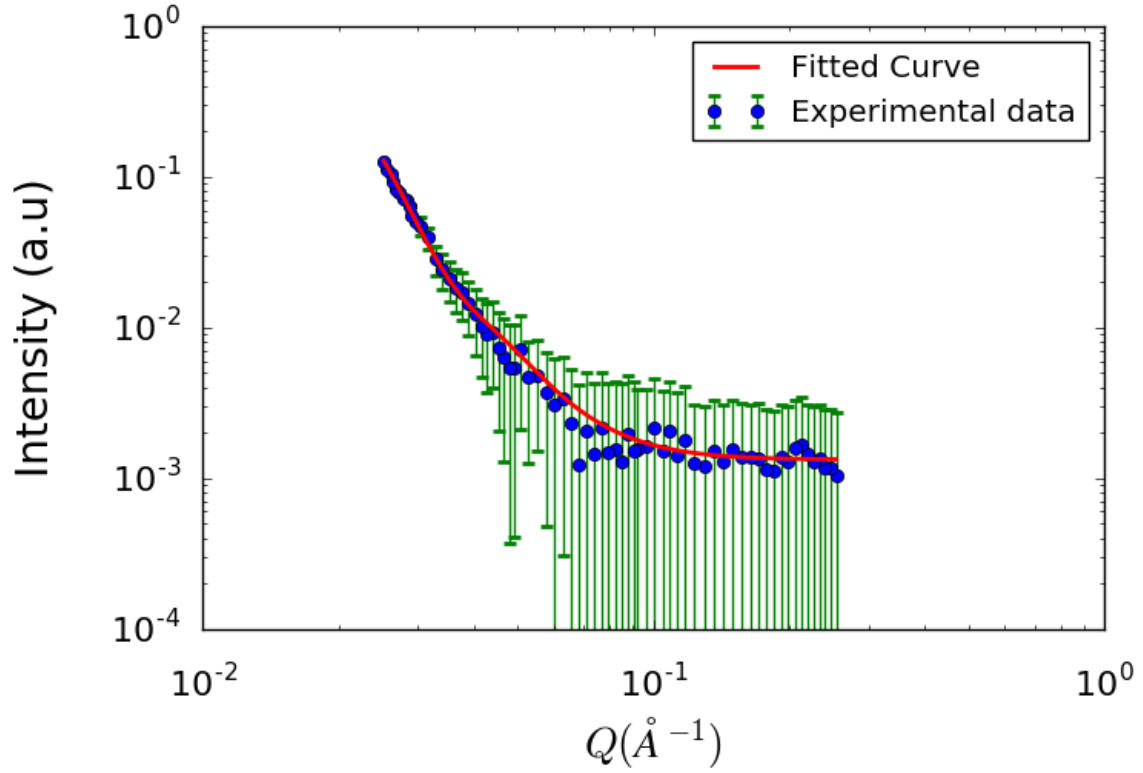


Figure 34: I vs. Q (blue curve) for $t=0$ to 10 minutes is fitted (red curve).

The error bar was also calculated for each parameter. The value of the reduced χ^2_{ν} corresponding to 30% probability of exceeding the minimum χ^2 with the degree of freedom of our fitting. The value is 1.025 for our fitting which was obtained from the table of chi-squared distributions [4]. Figure 35 shows the estimation of the error bar in parameter R for the growth

of the particles from 0 to 10 minutes. The radii corresponding to 1.08 were determined to calculate the error bars in R.

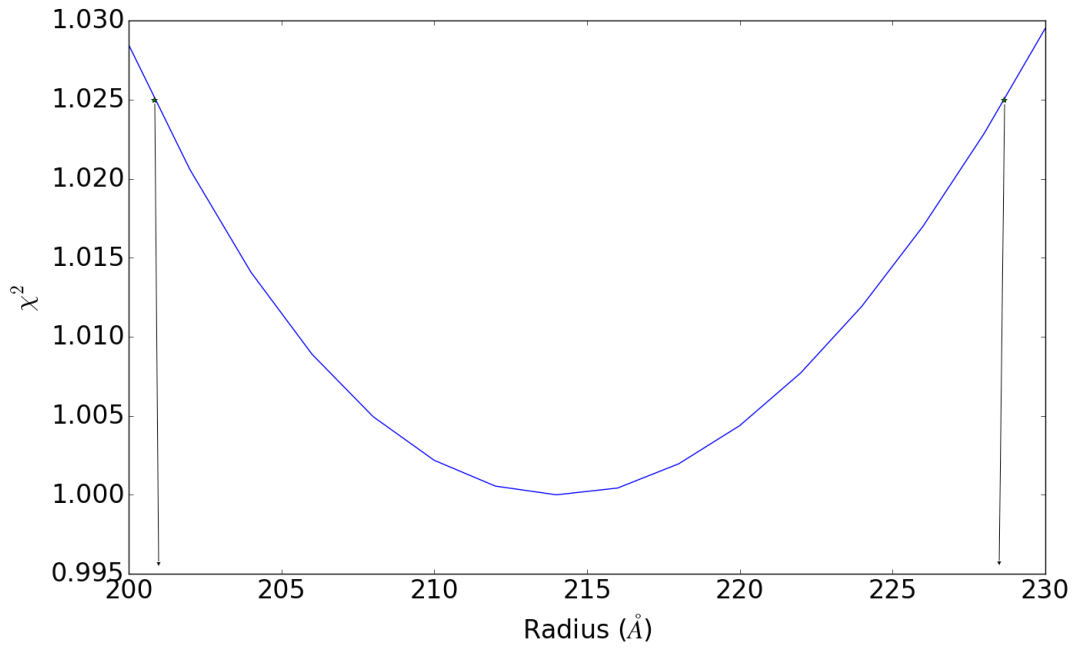


Figure 35: Distribution of χ^2 with R.

Figure 36 to Figure 47 shows 1D linecuts (blue dots) at different stages of the growth with the best fitted curves (red line). The best fitted parameter are tabulated in Table II.

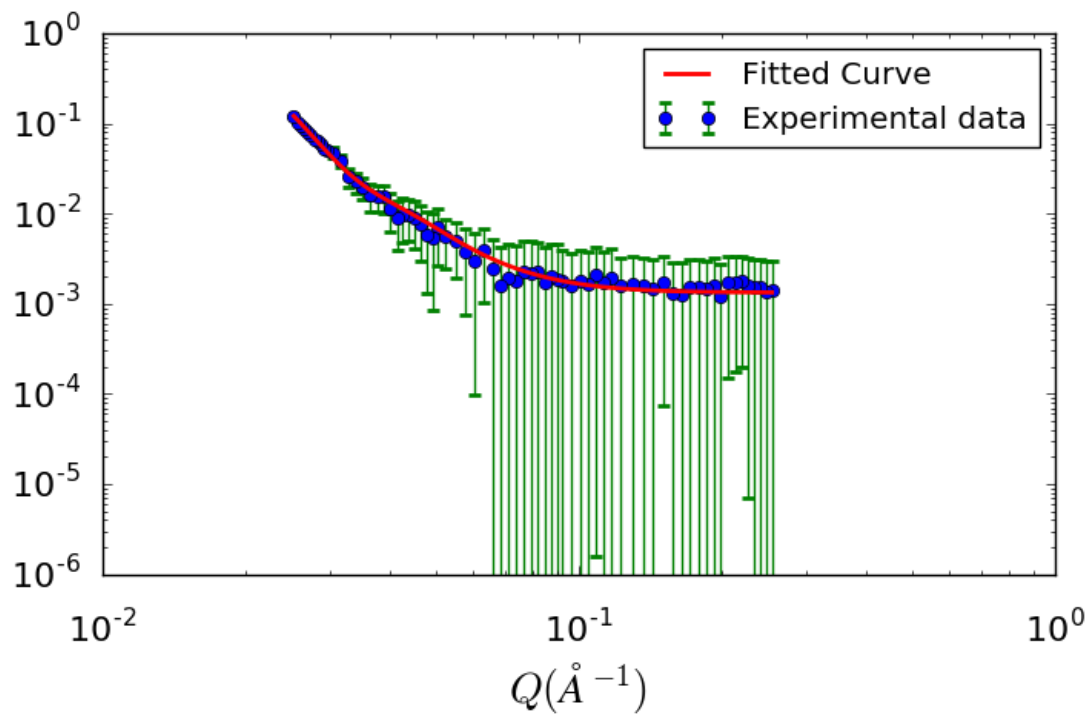


Figure 36: I vs. Q (blue curve) for $t=11$ to 20 minutes is fitted (red curve). Bottom part of the figure shows residuals.

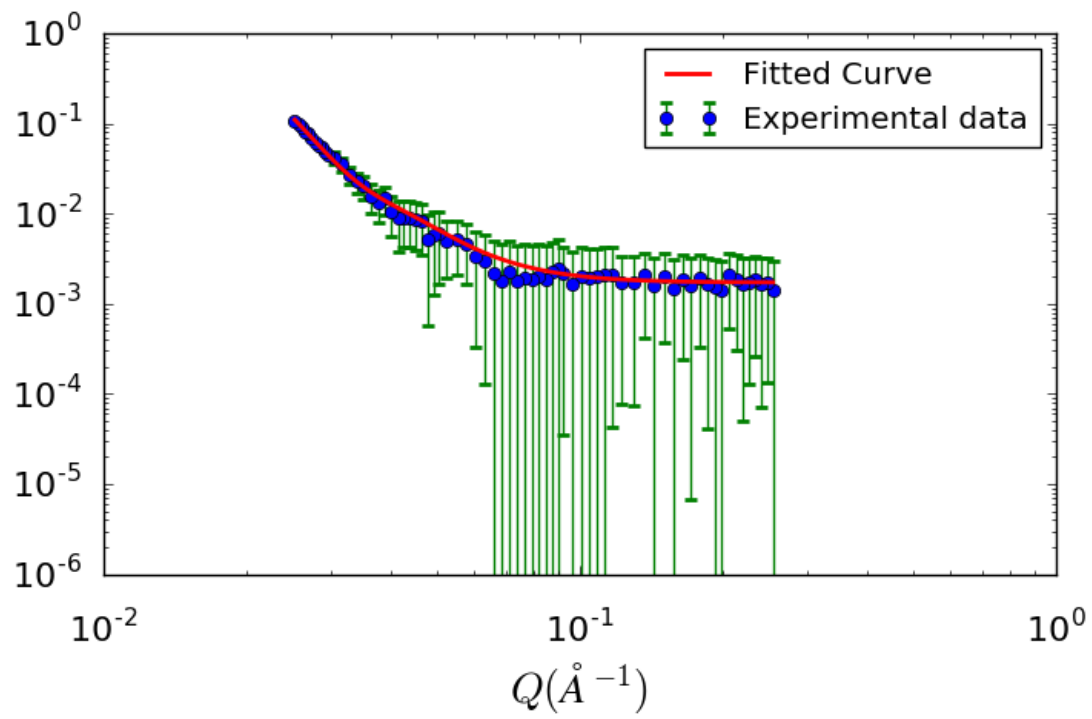


Figure 37: I vs. Q (blue curve) for $t=21$ to 30 minutes is fitted (red curve). Bottom part of the figure shows residuals.

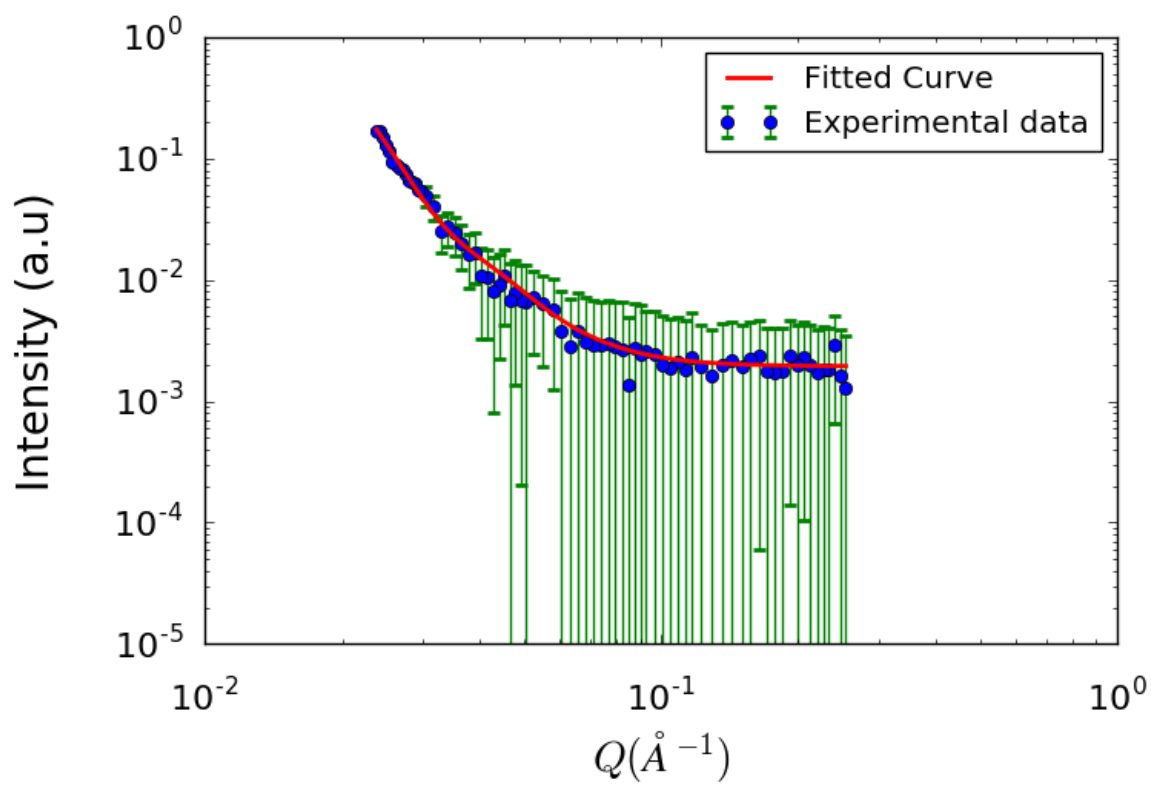


Figure 38: I vs. Q (blue curve) for $t=141$ to 150 minutes is fitted (red curve). Bottom part of the figure shows residuals.

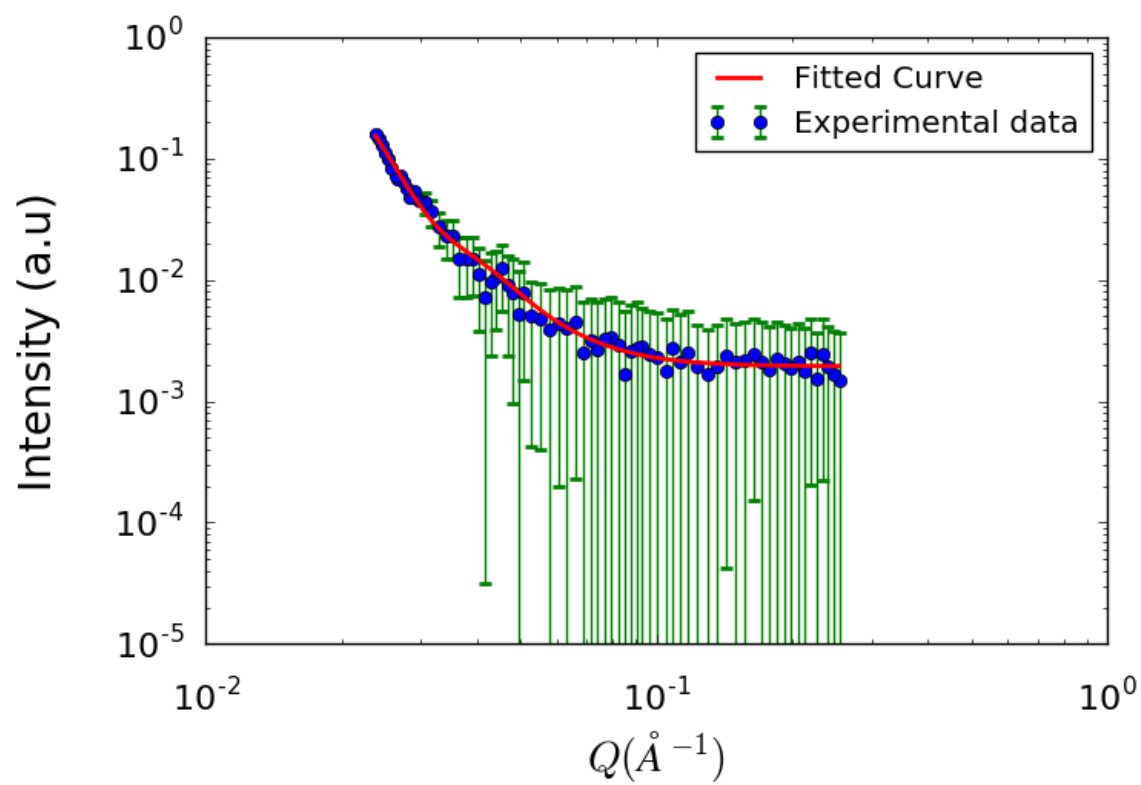


Figure 39: I vs. Q (blue curve) for $t=151$ to 160 minutes is fitted (red curve). Bottom part of the figure shows residuals.

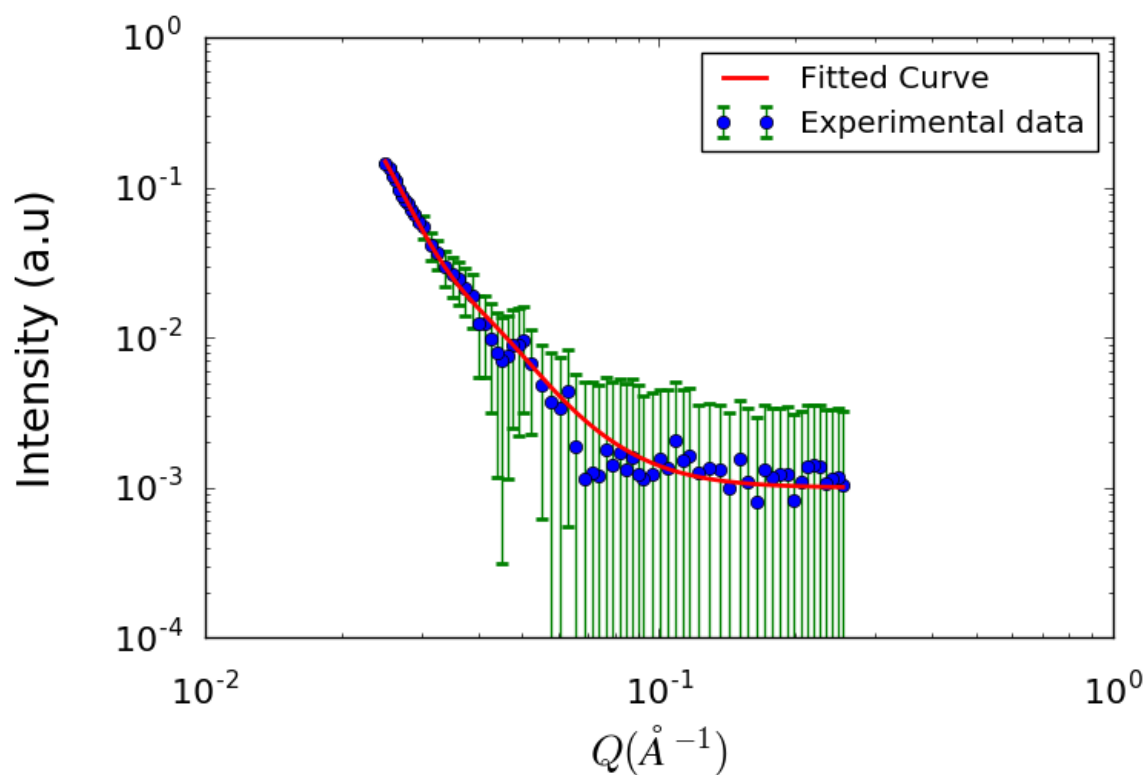


Figure 40: I vs. Q (blue curve) for $t=185$ to 194 minutes is fitted (red curve). Bottom part of the figure shows residuals.

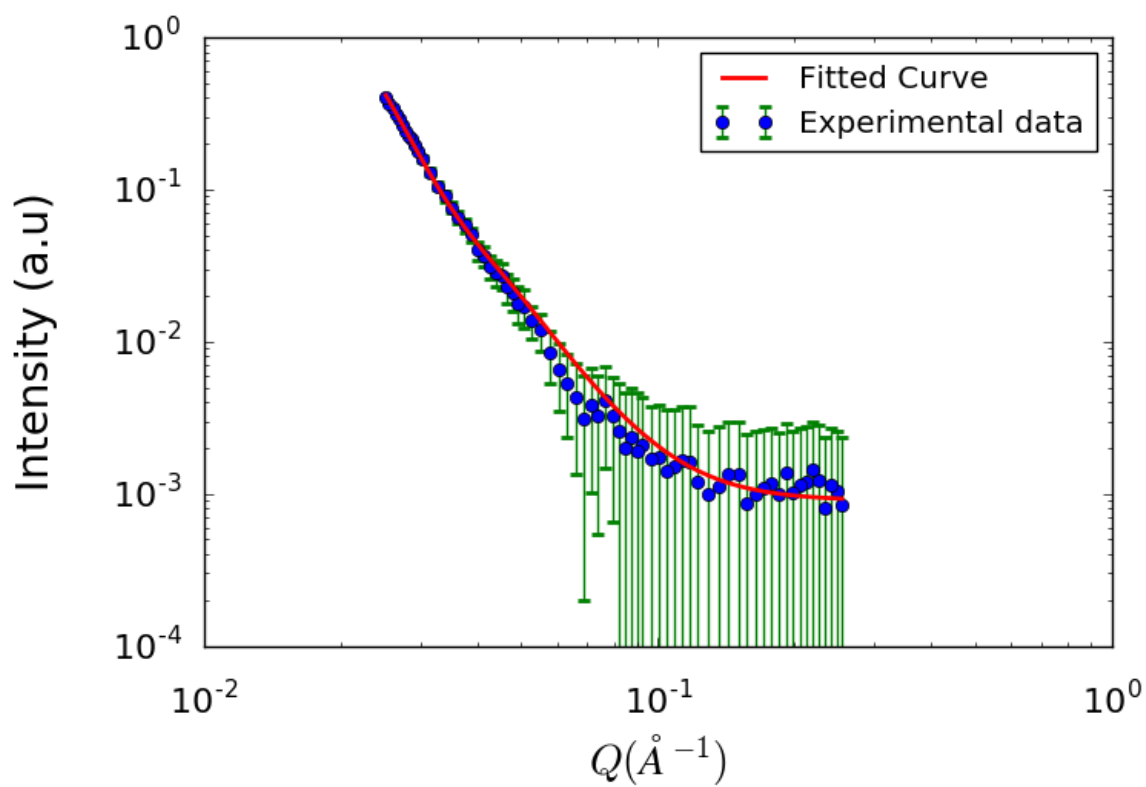


Figure 41: I vs. Q (blue curve) for $t=323$ to 332 minutes is fitted (red curve). Bottom part of the figure shows residuals.

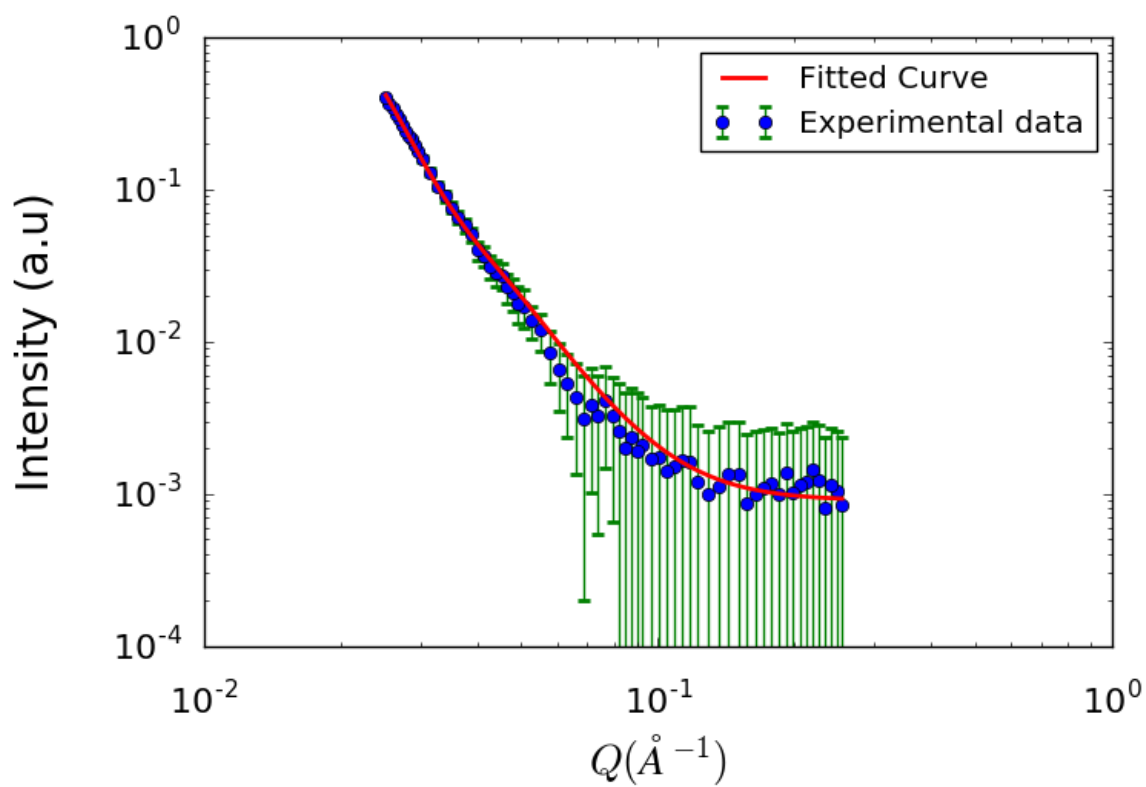


Figure 42: I vs. Q (blue curve) for $t=337$ to 346 minutes is fitted (red curve). Bottom part of the figure shows residuals.

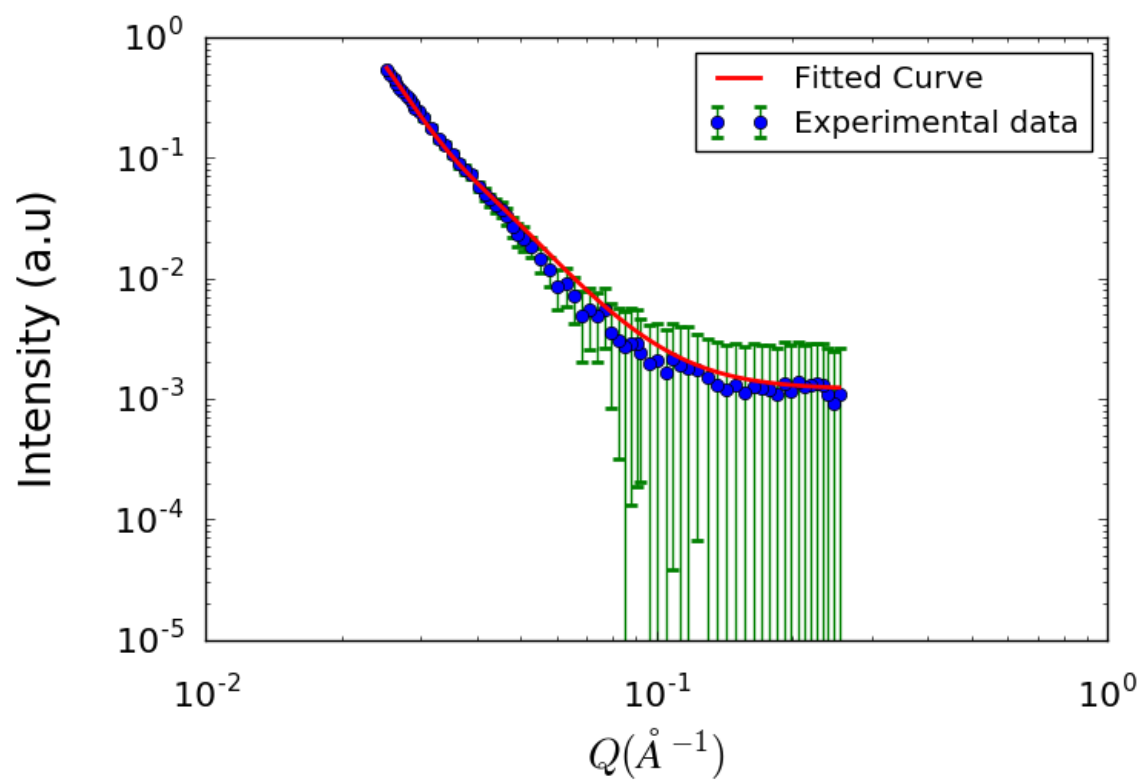


Figure 43: I vs. Q (blue curve) for $t=348$ to 357 minutes is fitted (red curve). Bottom part of the figure shows residuals.

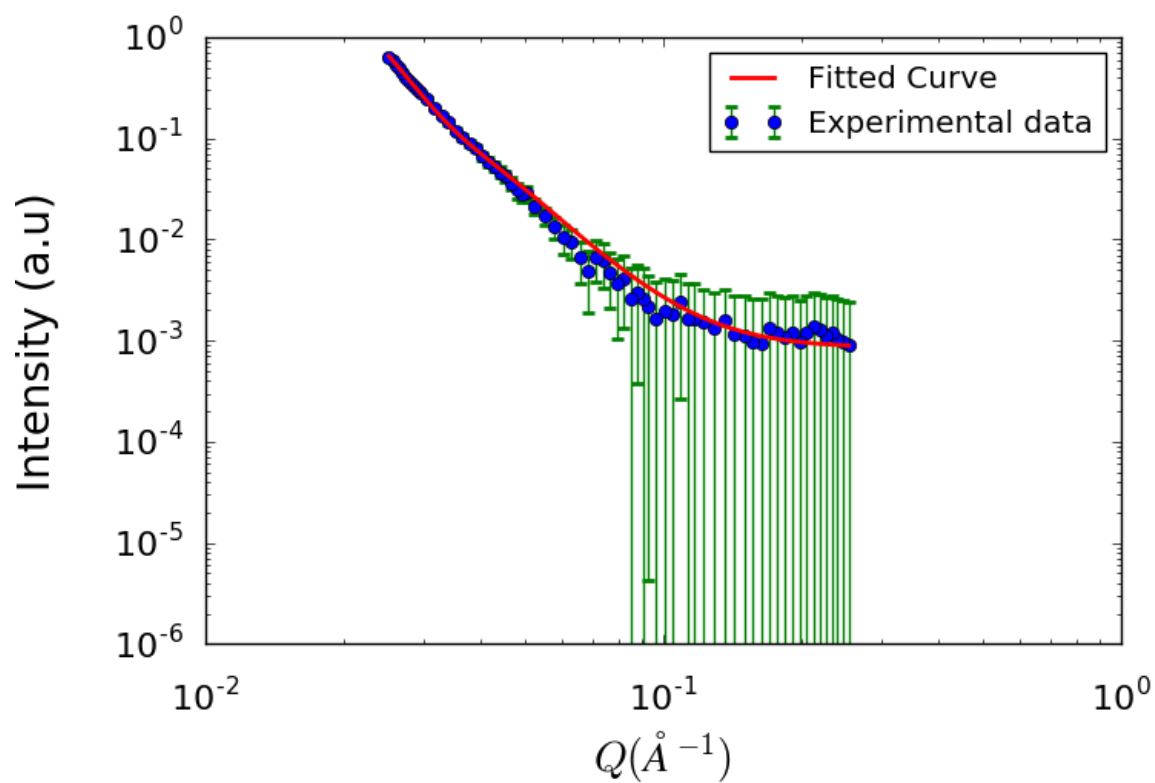


Figure 44: I vs. Q (blue curve) for $t=358$ to 369 minutes is fitted (red curve). Bottom part of the figure shows residuals.

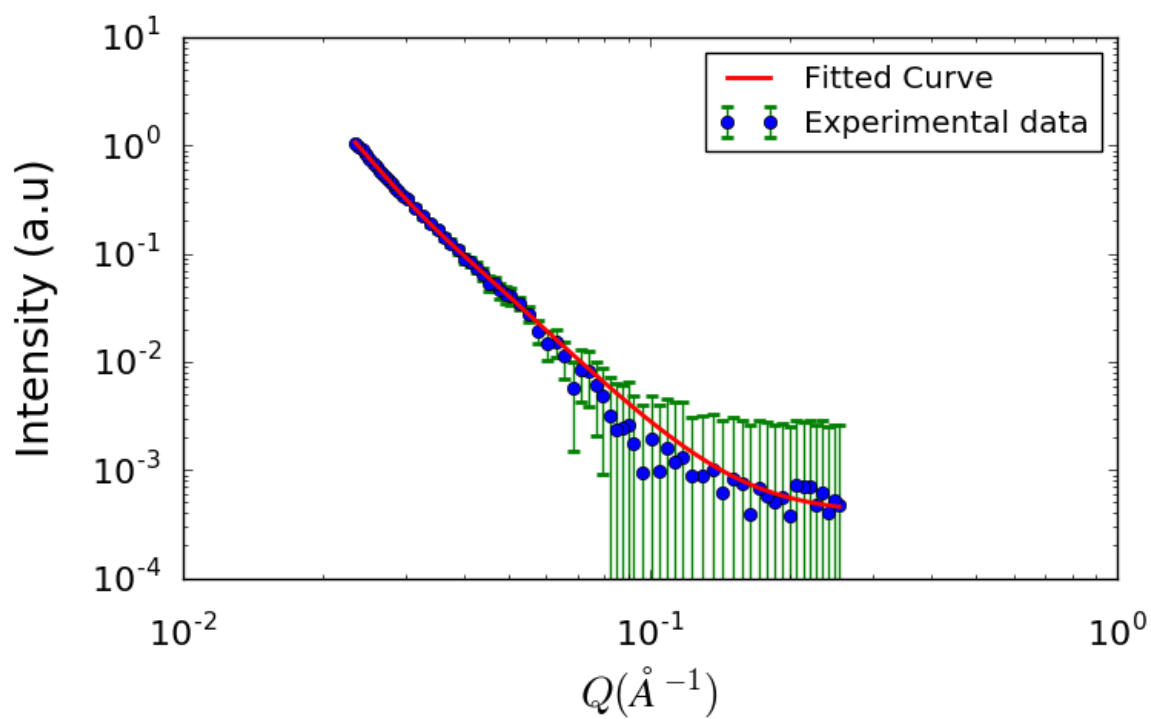


Figure 45: I vs. Q (blue curve) for $t=423$ to 432 minutes is fitted (red curve). Bottom part of the figure shows residuals.

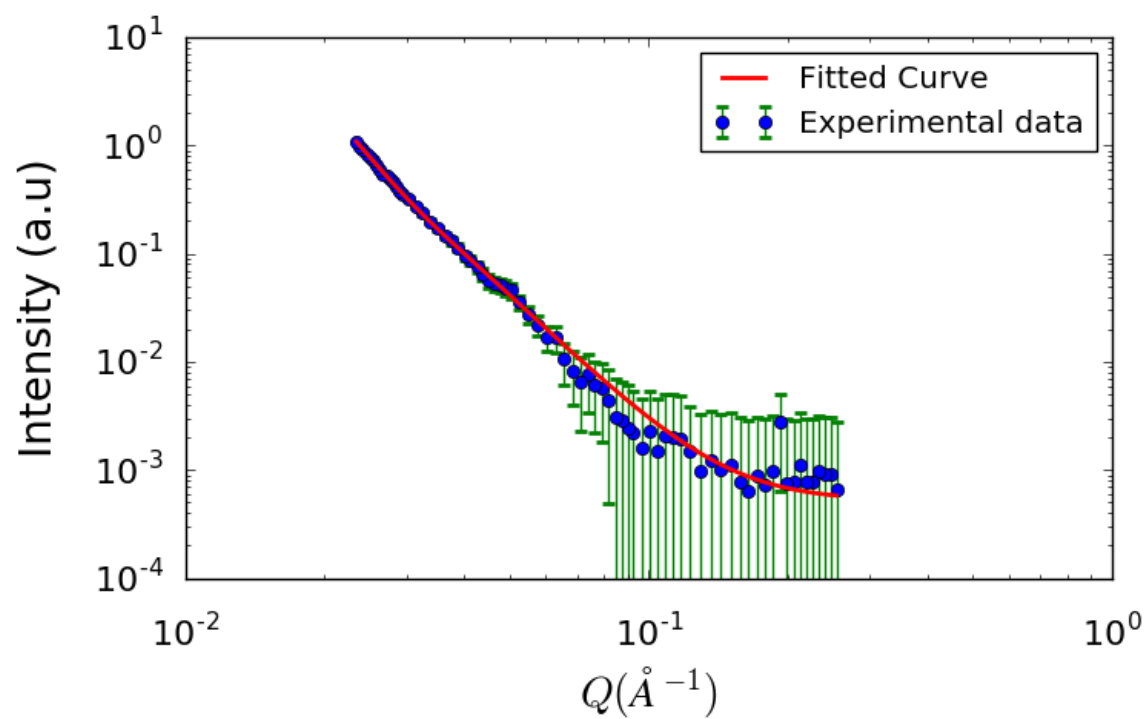


Figure 46: I vs. Q (blue curve) for $t=435$ to 444 minutes is fitted (red curve). Bottom part of the figure shows residuals.

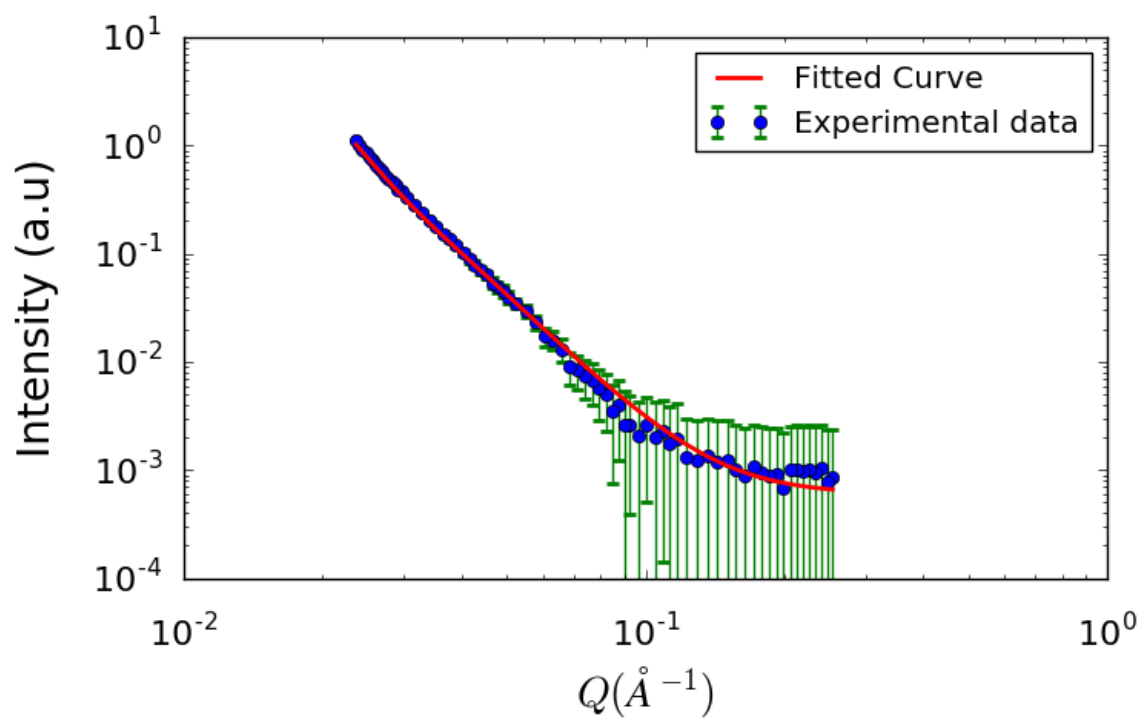


Figure 47: I vs. Q (blue curve) for $t=447$ to 456 minutes is fitted (red curve). Bottom part of the figure shows residuals.

time (minutes)	R (\AA)	$\sigma_R(\text{\AA})$	A
0-10	196^{+8}_{-7}	47^{+3}_{-3}	$2.69^{+0.37}_{-0.31}$
11-20	197^{+8}_{-8}	46^{+4}_{-3}	$2.72^{+.4}_{-0.37}$
21-30	207^{+8}_{-7}	46^{+4}_{-3}	$3.05^{+0.4}_{-0.36}$
141-150	210^{+12}_{-11}	50^{+6}_{-4}	$3.88^{+0.82}_{-0.73}$
151-160	211^{+9}_{-9}	48^{+4}_{-6}	$4.05^{+0.65}_{-0.62}$
185-194	215^{+9}_{-9}	54^{+4}_{-4}	$4.28^{+0.66}_{-0.59}$
323-332	228^{+8}_{-7}	64^{+7}_{-3}	$12.69^{+1.41}_{-01.19}$
337-346	235^{+6}_{-7}	66^{+4}_{-2}	$16.6^{+1.03}_{-2.1}$
348-357	239^{+7}_{-8}	69^{+2}_{-3}	$20.147^{+2.35}_{-2.247}$
358-369	231^{+6}_{-6}	64^{+2}_{-2}	$21.8^{+2.2}_{-2.0}$
423-432	319^{+12}_{-13}	108^{+7}_{-8}	$62.626^{+2.74}_{-5.71}$
435-444	325^{+16}_{-12}	109^{+11}_{-7}	$71.682^{+5.39}_{-4.12}$
447-456	339^{+13}_{-13}	116^{+8}_{-8}	$81.25^{+4.54}_{-4.04}$

TABLE II: Best fitted parameters of Raleigh form factor fitting with log normal distribution in R.

Scattering from the particles can be written as,

$$\Delta I(Q) = I_0 \cdot (\Delta\rho)^2 \cdot N \cdot V^2 \cdot |F(Q)|^2 \quad (4.13)$$

so, the constant A is proportional to the squared particle volume V. When A is normalized with the square of the volume of the particle, then the resultant is proportional to the number of particles. The volume of a spherical particle is $\frac{4\pi R^3}{3}$. A is then divided by the the square of the volume of corresponding average size particle.

Figure 48 shows the average radius, R, width of the distribution in radius, R and $\frac{A}{V^2}$ with time obtained from the analysis of the GISAXS patterns.

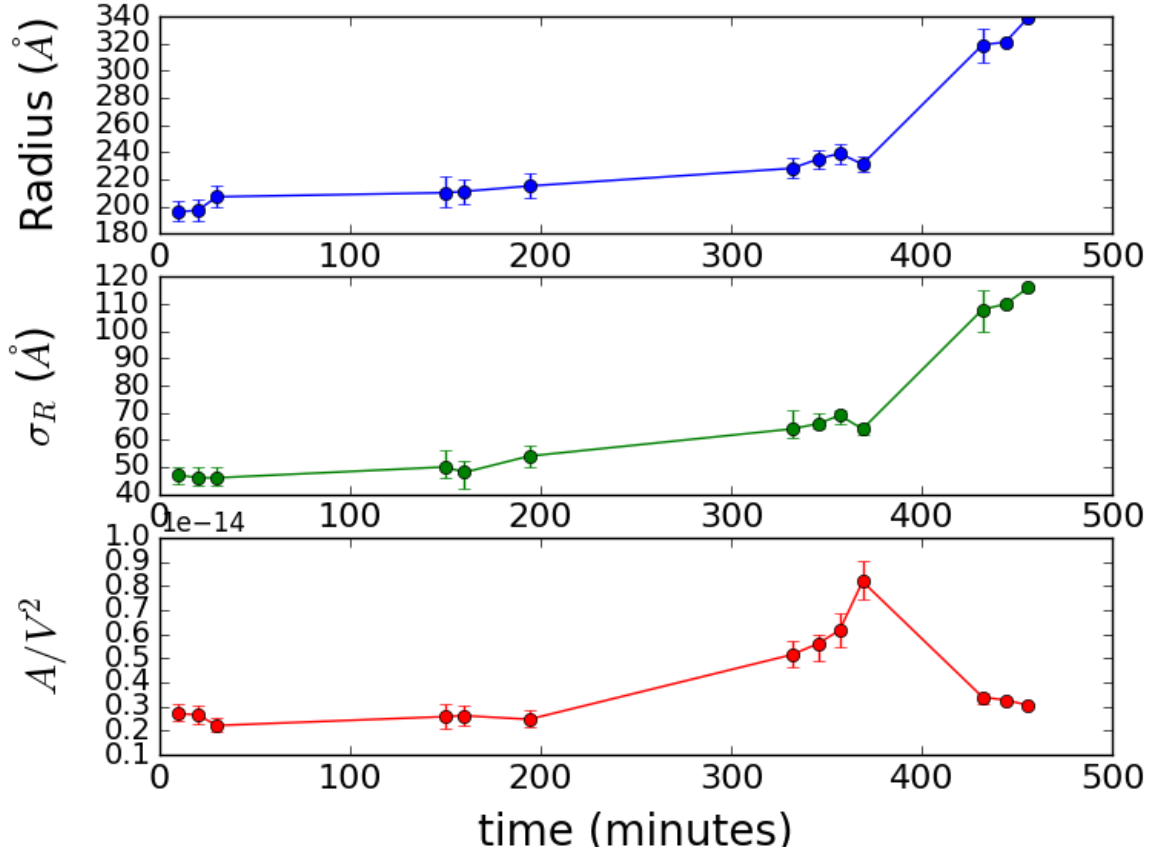


Figure 48: Best fitted values of R , σ and $\frac{A}{V^2}$

As Figure 48 suggests, AuNPs of size 196^{+8}_{-7} Å in radius with about 25% polydispersity were formed at the interface in first 10 minutes of the reduction reaction. The particles slowly increase in radius upto around 240 Å with increasing polydispersity in first 400 minutes. In this time interval the factor $\frac{A}{V^2}$ which is proportional to the number of particles at the interface increased significantly. After 400 minutes the particles grew in radius very fast and at 456

minutes the probed size of the particles was measured to be 339_{-13}^{+13} in radius with width of the distribution in radius 116_{-8}^{+8} . But the number of particles did not increase in this period of fast growth, rather it significantly decreased.

Although the AuNPs at the liquid-liquid interface were probed in situ with time by GISAXS, an obvious growth mechanism of the AuNPs cannot be proposed from our experiments. Because of the large background from scattering of the bulk aqueous phase, the high \mathbf{Q} region *i.e.* the very small particles could not be probed. Hence, no information on the nucleation of the particles was obtained. Since the quality of the data was increased by averaging GISAXS patterns over 10 minutes, the time resolution of our experiment was ten minutes. Although in our experiments no growth kinetics for the formation of AuNPs has been identified, our data places limits on the type of the mechanism that can be operating. it can be suggested from the GISAXS experiments that spherical AuNPs are formed through a sequence of reaction steps comprising very fast nucleation and growth ($t=0-10$ minutes), slow growth of the particles which is sustained by continuous reduction of gold precursor with the complete consumption of the precursor species ($t=10-400$ minutes) and finally the coalescence of particles to form bigger particles ($t> 400$ minutes).

CHAPTER 5

CONCLUSION

In this thesis, a new approach to study the formation of gold nanoparticle at the liquid-liquid interface is presented. The reduction between $AuCl_4^{-1}$ and the organic electron donor TPTA at the water-DCE interface is investigated in situ by grazing incidence small angle X-ray scattering technique. The reduction reaction is controlled electrochemically by using the potential-induced transfer of the $AuCl_4^{-1}$ in a homebuilt four electrode electrochemical cell. The system exploits the difference in the potential of reduction of $AuCl_4^{-1}$ between the water and DCE. The GISAXS measurements provide time-resolved in situ information on the formation of gold nanoparticles. The analysis of the GISAXS patterns shows formation of spherical particles at the interface where the particles increases in size with increasing polydispersity. Although a conclusive growth mechanism is not proposed in this thesis, from the analysis of the GISAXS patterns, it has been suggested the particles are formed in three steps, fast nucleation and growth, slow growth and coalescence. In conclusion, grazing incidence small angle X-ray scattering technique can be used to measure the structure and the average size of nanostructures formed at an liquid-liquid interface in situ. Because of the confinement of the X-ray beam at grazing incidence angle a large area of the surface can be measured, leading to very good statistics. Challenges for future studies are an improved resolution in time of the experimental method, minimization of background, hence probe smaller particles. Future study plan includes varying the conditions of synthesis to derive a comprehensive mechanism

of particles formation and invesgation of other metal nanoparticles for a comparative study in the formation mechanism.

APPENDIX

FITTING FUNCTION FOR GISAXS DATA ANALYSIS

The programs here are used to fit the GISAXS iD linecuts. The form factor was calculated for spherical particles which is then convoluted by a log normal distribution function with dispersion in radius as width. The convoluted form factor is scaled with a proportional factor to calculate the intensity. There are 3 parameters used to describe the scattering curve:

A: the scale factor

R: Average radius of the particles

ΔR Dispersity in average radius, R

The programs are written in programming language python. The following program calculates average form factor for spherical particles.

```
import numpy as np

import scipy.integrate as integ

class Form_Factors:

    def __init__(self):

        """ Class defining form factors for different shapes
```

APPENDIX (Continued)

```

""" self.re=2.814e-5

def sphere(self,q,R,Rsig=0.0,rho=1,rhos=0):

""" Form factor of a sphere:

q=Change in wave-vector transfer in Inverse Angstroms

R=Average Radius of the sphere in Angstroms

Rsig=standard deviation in R. Default=0 for single size.

rho=Electron density of the sphere Inverse Angstrom Cube. Default=1

rhos=Electron density of the medium Inverse Angstrom Cube. Default=0

""" if Rsig>0.1:

return (rho-rhos)**2*(np.sin(q*R)-q*R*np.cos(q*R))**2/(q*R)**6

else:

x=np.arange(R/10,4*R,R/10)

sf=[]

for qr in q:

sf.append(integ.trapz((rho-rhos)**2*(np.sin(qr*x)-qr*x*np.cos(qr*x))**2*self.logNormal(x,R,Rsig)/(qr*x)**6

return np.array(sf)

def logNormal(self,x,R,Rsig):

""" Log Normal Distribution:

x=size or radius of the nanoparticles.

```

APPENDIX (Continued)

R=Average radius of the nanoparticles.

Rsig=Standard deviation in R.

```
""" mu=np.log(R)-np.log(1+Rsig**2/R**2)/2.0
```

```
sig=np.sqrt(np.log(1+Rsig**2/R**2))
```

```
return np.exp(-(np.log(x)-mu)**2/2/sig**2)/np.sqrt(2*np.pi)/x/sig
```

The following program calculates the best fitting parameters

```
import pylab

import matplotlib.pyplot as pl

import numpy as np

import sys

from form_factors import Form_Factors

from lmfit import minimize, Parameters, conf_interval

import matplotlib.gridspec as gridspec

from matplotlib import ticker

# read the file def readfile():

global datalist,filename

filename=raw_input("enter the file number:")

filename="/Users/urmee/Desktop/mucuts.017/"+fnumber+"S# "+fnumber+"_sum.cut"
```

APPENDIX (Continued)

```
datalist = pylab.loadtxt(filename)
```

```
# In which region data will be fitted def limit():
```

```
global endlimit
```

```
endlimit=input('endlimit?')
```

```
def errorbar():
```

```
global err_bar
```

```
err_bar=input('err_bar? if yes, press 1, else 0: ')
```

```
scan=['linecut at Qxy 0.016']
```

```
readfile()
```

```
limit()
```

```
errorbar()
```

```
q=datalist[0:endlimit,0]
```

```
I=datalist[0:endlimit,1]
```

```
E=datalist[0:endlimit,2]
```


APPENDIX (Continued)

```

gs = gridspec.GridSpec(2,1)

def func(par,x):

ff=Form_Factors()

Rc=par['Rc'].value

Rcsig=par['Rcsig'].value

fac=par['fac'].value

bac=par['bac'].value

sum=ff.sphere(q,Rc,Rcsig)


return sum1*fac+bac


def residue(par, x, y,error,log): if log==1: if len(error)==0: return (np.log10(y)-np.log10(func(par,x)))
else: return (np.log10(y)-np.log10(func(par,x)))*y*np.log(10)/error else: if len(error)==0: re-
turn (y-func(par,x)) else: return (y-func(par,x))/error

par=Parameters()

par.add('Rc', value=195, vary=True, min=10.0, max=500.0)

par.add('Rcsig', value=47.258, vary=False, min=0.0, max=500.0)

par.add('fac', value=2.64, vary=False, min=1e-4, max=1000)

```

APPENDIX (Continued)

```

par.add('bac', value=9.93074*10**(-4), vary=False, min=0.0, max=1e-2)

print "_____ " print "Fitting for #", fnum," :
Please wait..." print " minobj=minimize(residue,par,args=(q,I,E,log)) minobj.leastsq() p_names=[name
for name in ['Rc','Rcsig','fac','bac'] if par[name].vary] print "Fitting Parameters"

for name in p_names: print name,'=',par[name].value print "Min ChiSquare=", minobj.chisqr

Rc=par['Rc'].value
Rcsig=par['Rcsig'].value
fac=par['fac'].value
bac=par['bac'].value

fit=func(par,q)

gs = gridspec.GridSpec(2,1,height_ratios=[10,3],hspace=0.1)

fig = pl.figure()

ax.legend()

pl.errorbar(q, I,E,fmt='o', ecolor='g', capthick=2, label='Experimental Data')

ax.plot(q,fit,'r',linewidth=1,label='Fitted Curve')

```

APPENDIX (Continued)

```
ax.set_xscale("log")

ax.set_yscale("log")

ax.set_xlabel('Q( $\text{\AA}^{-1}$ )',linespacing=8,fontsize=20)

ax.set_ylabel('Intensity (a.u)',fontsize=20)


ax.tick_params(axis='x', pad=15,labelsz=16)

ax.tick_params(axis='y', pad=10,labelsz=16, which= 'major')


pl.show()
```

CITED LITERATURE

1. Benjamin Abécassis, Fabienne Testard, Olivier Spalla, and Philippe Barboux. Probing in situ the nucleation and growth of gold nanoparticles by small-angle x-ray scattering. *Nano letters*, 7(6):1723–1727, 2007.
2. Jens Als-Nielsen and Des McMorrow. *Elements of modern X-ray physics*. John Wiley & Sons, 2011.
3. Marc Baus and Jean-Louis Colot. Thermodynamics and structure of a fluid of hard rods, disks, spheres, or hyperspheres from rescaled virial expansions. *Physical Review A*, 36(8):3912, 1987.
4. Philip R Bevington, D Keith Robinson, J Morris Blair, A John Mallinckrodt, Susan McKay, et al. Data reduction and error analysis for the physical sciences. *Computers in Physics*, 7(4):415–416, 1993.
5. Sarah D Brown, Paola Nativio, Jo-Ann Smith, David Stirling, Paul R Edwards, Balaji Venugopal, David J Flint, Jane A Plumb, Duncan Graham, and Nial J Wheate. Gold nanoparticles for the improved anticancer drug delivery of the active component of oxaliplatin. *Journal of the American Chemical Society*, 132(13):4678–4684, 2010.
6. Mathias Brust, Merryl Walker, Donald Bethell, David J Schiffrin, and Robin Whyman. Synthesis of thiol-derivatised gold nanoparticles in a two-phase liquid–liquid system. *J. Chem. Soc., Chem. Commun.*, (7):801–802, 1994.
7. David J Des Marais, Louis J Allamandola, Steven A Benner, Alan P Boss, David Deamer, Paul G Falkowski, Jack D Farmer, S Blair Hedges, Bruce M Jakosky, Andrew H Knoll, et al. The nasa astrobiology roadmap. *Astrobiology*, 3(2):219–235, 2003.
8. Tiberio A Ezquerra, Mari Cruz Garcia-Gutierrez, Aurora Nogales, and Marian Gomez. *Applications of synchrotron light to scattering and diffraction in materials and life sciences*, volume 776. Springer, 2009.
9. Yvonne Gründer, Huong LT Ho, J Fred W Mosselmans, Sven LM Schroeder, and Robert AW Dryfe. Inhibited and enhanced nucleation of gold nanoparticles at the water—1, 2-dichloroethane interface. *Physical Chemistry Chemical Physics*, 13(34):15681–15689, 2011.

10. Yvonne Grunder, J Frederick W Mosselmans, Sven LM Schroeder, and Robert AW Dryfe. In situ spectroelectrochemistry at free-standing liquid–liquid interfaces: Uv–vis spectroscopy, microfocus x-ray absorption spectroscopy, and fluorescence imaging. *The Journal of Physical Chemistry C*, 117(11):5765–5773, 2013.
11. A Guiner, Gérard Fournet, and CB Walker. Small angle scattering of x-rays. *J. Wiley & Sons, New York*, 1955.
12. PA Heiney. Datasqueeze. department of physics and astronomy, 2006.
13. Binyang Hou. *Ion distributions at electrified liquid-liquid interfaces: Microscopic and macroscopic measurements*. PhD thesis, University of Illinois at Chicago, 2011.
14. Daniel Huang, Frank Liao, Steven Molesa, David Redinger, and Vivek Subramanian. Plastic-compatible low resistance printable gold nanoparticle conductors for flexible electronics. *Journal of the electrochemical society*, 150(7):G412–G417, 2003.
15. Xiaohui Ji, Xiangning Song, Jun Li, Yubai Bai, Wensheng Yang, and Xiaogang Peng. Size control of gold nanocrystals in citrate reduction: the third role of citrate. *Journal of the American Chemical Society*, 129(45):13939–13948, 2007.
16. K Lance Kelly, Eduardo Coronado, Lin Lin Zhao, and George C Schatz. The optical properties of metal nanoparticles: the influence of size, shape, and dielectric environment, 2003.
17. J Kimling, M Maier, B Okenve, Vassilios Kotaidis, H Ballot, and Anton Plech. Turkevich method for gold nanoparticle synthesis revisited. *The Journal of Physical Chemistry B*, 110(32):15700–15707, 2006.
18. Stephan Kubowicz, Markus A Hartmann, Jean Daillant, Milan K Sanyal, Ved V Agrawal, Christian Blot, Oleg Kononov, and Helmuth Mohwald. Gold nanoparticles at the liquid- liquid interface: X-ray study and monte carlo simulation. *Langmuir*, 25(2):952–958, 2008.
19. Catherine J Murphy, Tapan K Sau, Anand M Gole, Christopher J Orendorff, Jinxin Gao, Linfeng Gou, Simona E Hunyadi, and Tan Li. Anisotropic metal nanoparticles: synthesis, assembly, and optical applications, 2005.
20. Lyman G Parratt. Surface studies of solids by total reflection of x-rays. *Physical review*, 95(2):359, 1954.

21. Siva Rama Krishna Perala and Sanjeev Kumar. On the mechanism of metal nanoparticle synthesis in the brust–schiffrin method. *Langmuir*, 29(31):9863–9873, 2013.
22. Peter S Pershan and Mark Schlossman. *Liquid Surfaces and Interfaces: Synchrotron X-ray Methods*. Cambridge University Press, 2012.
23. Francesca Pietra, Freddy T Rabouw, Wiel H Evers, Dima V Byelov, Andrei V Petukhov, Celso de Mello Donega, and Daniel Vanmaekelbergh. Semiconductor nanorod self-assembly at the liquid/air interface studied by in situ gisaxs and ex situ tem. *Nano letters*, 12(11):5515–5523, 2012.
24. Boon-Kin Pong, Hendry I Elim, Jian-Xiong Chong, Wei Ji, Bernhardt L Trout, and Jim-Yang Lee. New insights on the nanoparticle growth mechanism in the citrate reduction of gold (iii) salt: formation of the au nanowire intermediate and its nonlinear optical properties. *The Journal of Physical Chemistry C*, 111(17):6281–6287, 2007.
25. Gilles Renaud, Rémi Lazzari, and Frédéric Leroy. Probing surface and interface morphology with grazing incidence small angle x-ray scattering. *Surface Science Reports*, 64(8):255–380, 2009.
26. Denise Bertulucci Rocha Rodrigues, Sanivia Aparecida Lima Pereira, Marlene Antônia dos Reis, Sheila Jorge Adad, João Eduardo Caixeta, Angélica Maeda Chiba, Richard Átila Sousa, and Virmondes Rodrigues, Jr. In situ detection of inflammatory cytokines and apoptosis in pemphigus foliaceus patients. *Archives of pathology & laboratory medicine*, 133(1):97–100, 2009.
27. Milan K Sanyal, Ved V Agrawal, Mrinal K Bera, KP Kalyanikutty, Jean Daillant, Christian Blot, S Kubowicz, Oleg Konovalov, and CNR Rao. Formation and ordering of gold nanoparticles at the toluene- water interface. *The Journal of Physical Chemistry C*, 112(6):1739–1743, 2008.
28. Mark L Schlossman. Liquid–liquid interfaces: studied by x-ray and neutron scattering. *Current opinion in colloid & interface science*, 7(3):235–243, 2002.
29. Tanya Stuchinskaya, Miguel Moreno, Michael J Cook, Dylan R Edwards, and David A Russell. Targeted photodynamic therapy of breast cancer cells using antibody–phthalocyanine–gold nanoparticle conjugates. *Photochemical & Photobiological Sciences*, 10(5):822–831, 2011.

30. Allen C Templeton, W Peter Wuelfing, and Royce W Murray. Monolayer-protected cluster molecules. *Accounts of Chemical Research*, 33(1):27–36, 2000.
31. David T Thompson. Using gold nanoparticles for catalysis. *Nano Today*, 2(4):40–43, 2007.
32. John Turkevich, Peter Cooper Stevenson, and James Hillier. A study of the nucleation and growth processes in the synthesis of colloidal gold. *Discussions of the Faraday Society*, 11:55–75, 1951.
33. JA Venables. Rate equation approaches to thin film nucleation kinetics. *Philosophical Magazine*, 27(3):697–738, 1973.
34. Y Yoneda. Anomalous surface reflection of x rays. *Physical review*, 131(5):2010, 1963.
35. Shenghu Zhou, Bindhu Varughese, Bryan Eichhorn, Greg Jackson, and Kevin McIlwrath. Pt–cu core–shell and alloy nanoparticles for heterogeneous nox reduction: anomalous stability and reactivity of a core–shell nanostructure. *Angewandte Chemie*, 117(29):4615–4619, 2005.
36. Y Zhu and RA Antonia. The spatial resolution of hot-wire arrays for the measurement of small-scale turbulence. *Measurement Science and Technology*, 7(10):1349, 1996.